MODELING AND FABRICATION OF IONIC POLYMER-METAL COMPOSITE (IPMC) SENSORS

By

Hong Lei

A DISSERTATION

Submitted to
Michigan State University
in partial fulfillment of the requirements
for the degree of

Electrical Engineering - Doctor of Philosophy

2015

ABSTRACT

MODELING AND FABRICATION OF IONIC POLYMER-METAL COMPOSITE (IPMC) SENSORS

By

Hong Lei

Ionic polymer-metal composites (IPMCs) are an important class of electroactive polymers (EAPs) with built-in actuation and sensing capabilities. They have received tremendous interest for their potential in various sensor applications. In this dissertation, a physics-based dynamic model is proposed for cantilevered IPMC sensors that are excited at the base, and the humidity-dependence of IPMC sensing dynamics is discussed based on this model. To ensure the sensing consistency, thick parylene encapsulation is proposed for IPMC sensors, and the performance of encapsulated IPMC sensors is evaluated. Fabrication and modeling of two novel IPMC sensors and micro-fabrication of IPMC-based artificial lateral line system are also presented. These contributions are further elaborated below.

The proposed dynamic model is physics-based, and it combines the vibration dynamics of a flexible beam under base excitation and the ion transport dynamics within an IPMC. In addition, it incorporates the effect of a tip mass. The model is further reduced to finite dimensional one, based on which an inverse compensation scheme is proposed to reconstruct the base excitation signal given the sensor output. Both simulation and experiments are conducted to validate the model and the inverse compensation scheme. The humidity-dependence of IPMC sensing dynamics is also studied based on the latter model, where the humidity-dependence of five physical parameters is captured with polynomial functions, which are then plugged into the model to predict the IPMC sensing output.

Encapsulated IPMC sensors based on thick parylene coating are presented to ensure sensing

consistency. The proposed fabrication process comprises major steps of parylene deposition and water drive-in. The physical properties of coated IPMCs are tested and their sensing performances are evaluated under different media along with the comparison with the typical naked IPMC sensors. Experimental results show that the proposed thick parylene coating can effectively maintain the sensing consistency, which allows IPMC sensors to be used in practical applications.

Two novel IPMC sensors capable of omnidirectional sensing are proposed. One is fabricated by plating two pairs of electrodes on orthogonal surfaces of a Nafion square column, and the other uses Nafion tubing as the raw materials to fabricate a tubular IPMC. The sensing responses of both fabricated IPMC sensors are characterized to evaluate their omnidirectional sensing capabilities and the coupling issue is discussed for both cases. An empirical model and a physical model are further developed for the proposed square column IPMC sensor and tubular IPMC sensor, respectively.

Inspired by the lateral line system, a micro-fabrication process is presented to realize flow sensor arrays based on IPMCs. Several challenges are addressed in the proposed recipe including the non-planar process, soft material, and selective formation of electrodes. A new approach of double-subtraction is developed and the first prototype is presented.

Dedicated to my family with all my love and gratitude.

ACKNOWLEDGMENTS

I would like to express my sincere gratitude to my advisor, Prof. Xiaobo Tan, for providing me with this research assistant opportunity in Smart Microsystems Lab during my doctoral study. His valuable guidance and generous encouragement benefited me a lot in my research and will always do it on my future career.

I want to thank all my Ph.D. committee members: Prof. Hassan Khalil, Prof. Guoming Zhu, and Prof. Wen Li at Michigan State University, for kindly joining my advisory committee and offering me insightful comments. In particular, I thank Prof. Wen Li for aiding me in the area of fabrication and materials. I also thank our research collaborators, Prof. Derek A. Paley at University of Maryland and Prof. Kalyanmoy Deb at Michigan State University, for their constant support and kind help in my research projects.

I would like to thank the ECE technical staff, ECE cleanroom committee, and ECE cleanroom colleagues for their advice and assistance on my fabrication work in ECE cleanroom at Michigan State University, in particular, Brian Wright, Karl Dersch, Prof. Timothy P. Hogan, and Dr. Yue Huang. I would also like to thank Dr. Sandrine Martin in the Lurie Nanofabrication Facility (LNF) for her help on my fabrication work in LNF at University of Michigan.

I am grateful to all my colleagues and friends who have offered help in various ways, especially to John Thon, Dr. Feitian Zhang, Dr. Jianxun Wang, Cody Thon, Chaiyong Lim, Bin Tian, Francis D. Lagor, Prof. Levi DeVries, Dr. Alex Esbrook, Dr. Ahmad T. Abdulsadda, Jun Zhang, Bo Song, Dr. Xianbo Yang, Ali Ahrari, and Montassar Aidi Sharif. Their comments and collaboration have helped my research a lot. Thanks also to all of the administrators and staff members in the ECE department for their assistance over the years.

I would also like to acknowledge the financial support from National Science Foundation

(ECCS 0547131, DBI 0939454) and Office of Naval Research (N000140810640, N000141210149) for their support of my research.

Most of all, I am foremost thankful for my family. I would like to thank my mother, Jishu Sun, my father, Minghua Lei, and my sister, Yan Lei, for their all-enduring love and everlasting support in this life journey. I lost my dear father two years ago, but my life was brightened again by my fiancee, Hang Guo, to whom I am deeply grateful for her selfless love, support and encouragement. This dissertation would not have been possible without their years of encouragement and continuous support in both good times and bad times.

TABLE OF CONTENTS

LIST OF TABLES

LIST OF FIGURES

Chapter 1

Introduction

Ionic polymer-metal composites (IPMCs) have inherent sensing properties. They hold strong promise for versatile applications as sensors for their direct mechanosensory property and inherent polarity. A physics-based dynamic model and novel fabrication methods of IPMC sensors are proposed in this report.

In this introduction, a brief background is first presented for this smart material of IPMCs. It is followed by the discussion on the modeling of IPMC sensors: a literature review is conducted and my accomplished work on the modeling is discussed. Afterwards, new fabrications of IPMC sensors are presented, including encapsulated IPMCs, square column and tubular IPMCs, and artificial lateral line system based on IPMCs. At last, an overview of the contributions is presented.

1.1 Ionic Polymer-Metal Composites

Electroactive polymers (EAPs) have received tremendous interest for their potential applications in a large variety of engineering areas [1]. Ionic polymer-metal composites (IPMCs) are an important class of EAPs with built-in actuation and sensing capabilities. They hold strong promise for versatile applications because they require low-actuation voltages (several volts) for producing large bending deformation, work in air and in aqueous environments without stringent packaging requirements, and have minimal structural complexity in implementation as actuators and sensors [2, 3]. They are also bio-compatible and amenable to microfabrication [4, 5].

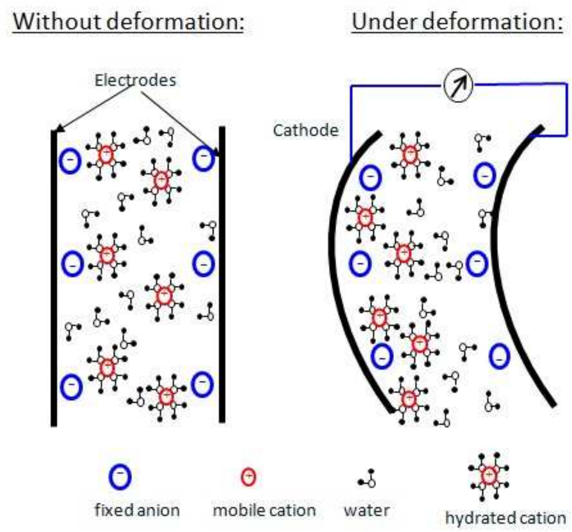

Figure 1.1: Illustration of IPMC sensing principle.

An IPMC sample typically consists of a thin ion-exchange membrane (e.g., Nafion), chemically plated with a noble metal as electrodes on both surfaces. The traditional method for the fabrication of IPMCs is based on the impregnation-reduction-ion-exchange process [6]. Inside the polymer, anions covalently fixed to polymer chains are balanced by mobile cations. An applied voltage across the IPMC leads to the redistribution of cations and accompanying solvent molecules, resulting in both differential swelling and electrostatic forces, which cause the material to bend and hence the actuation effect [2, 7, 8]. IPMC actuators have been proposed for various applications in biomedical devices [9], grippers and manipulation systems [10], and biomimetic robotics [11, 12]. On the other hand, IPMCs have inherent sensing properties – an applied force or deformation on an IPMC beam yields a detectable electrical signal (typically open-circuit voltage or short-circuit current) across the electrodes, as illustrated in Fig. 1.1 . Recent applications of IPMC sensing capability span measurement of force, pressure, displacement and shear loading, structural health monitoring, and energy harvesting [13–21].

1.2 Modeling of IPMC Sensors

1.2.1 Dynamic Modeling of Base-excited IPMC Sensors

There has been extensive effort in modeling and understanding IPMC sensors in recent years. Newbury and Leo proposed a grey-box model for IPMC actuators and sensors by drawing analogy to piezoelectric transducers [22, 23]. The latter model was further elaborated and verified by Bonomo *et al.* [24]. Takagi *et al.* [25] examined the modeling of IPMC sensors using the current and voltage as the output respectively, based on Onsager's equation. Buechler and Leo [26] presented a variational formulation to model IPMCs and evaluated the model computationally with the Galerkin method. Various physics-based models have also been studied for IPMCs. For example, de Gennes *et al.* [27] used linear irreversible thermodynamics to study IPMC transduction, where a static model was proposed to capture both actuation and sensing mechanisms. Through a micromechanics approach, Nemat-Nasser and Li [7] presented a partial differential equation (PDE) governing the charge dynamics in IPMC materials. This model was used by Farinholt and Leo [28] to derive the charge sensing response for a cantilevered IPMC beam subject to tip displacement. With the same governing PDE from [7], Chen *et al.* [29] developed a geometrically scalable, infinite-dimensional transfer function model for cantilevered IPMC sensors subjected to tip stimulus, where the effect of distributed surface resistance of IPMC electrodes is captured. In [30], Porfiri developed a comprehensive framework for modeling IPMC actuation and sensing based on mixture theory [31], which was specialized to the analysis of linear static deformation of a thin and flat IPMC. Aureli and Porfiri further extended the modeling framework for IPMC sensing to account for convection and large deformations in [32].

Various configurations of IPMC sensors have been considered in the literature. The most common configuration is an IPMC cantilever beam, where the stimulus is applied at the free end of the beam. Integrating multiple IPMC sensors in an array results in an artificial lateral line system for flow sensing, as reported in [33]. An IPMC undergoing longitudinal vibrations has been proposed for energy harvesting [20]. A dynamic curvature sensor has been created by bonding an IPMC to the surface of a structure [16]. Another important configuration for IPMC sensors is a cantilevered IPMC subjected to base excitation, which finds potential applications in energy harvesting and structural monitoring [14, 18, 19].

In this dissertation, a dynamic, physics-based model for a base-excited IPMC sensor loaded with a tip mass, is proposed. It has a closed-form expression and combines the vibration dynamics of a flexible beam with a tip mass under base excitation and the ion transport dynamics within the IPMC. The mechanical vibration of the IPMC is modeled with Euler-Bernoulli cantilever beam theory, incorporating damping and accommodating suitable boundary conditions. The ion transport dynamics is based on the governing PDE in [7] that accounts for electrostatic interactions, ionic diffusion and ionic migration along the thickness direction. For the purpose of real-time signal processing, the original infinite-dimensional model is reduced to finite-dimension by combining techniques of Padé approximation and Taylor series expansion. An inverse compensation scheme for the reduced model is then presented to reconstruct the base excitation signals given the sensor output. Both the simulation and experiments are conducted to validate the proposed model and inverse compensation scheme.

1.2.2 Modeling of Humidity-dependence of IPMC Sensing Dynamics

A critical issue for the sensing behavior of IPMCs is that they need ionic hydration to operate in air. The content of water, the most commonly used solvent in the IPMCs, varies with the humidity level of the ambient environment, significantly affecting the sensing properties of an IPMC in air. This humidity-dependence is primarily rooted in the internal physics of the sensing mechanism of

IPMCs and results in the difficulty of maintaining accurate sensing properties of IPMC sensors. Therefore, it is of great interest to study the humidity-dependence of IPMC sensors. Some work on characterizing the influence of humidity on IPMCs has been reported. Bauer *et al.* [34] studied the influence of humidity on a Nafion 117 film from the aspect of mechanical properties. Shoji and Hirayama [35] experimentally characterized the humidity effect on the performance of IPMC actuators. Brunetto *et al.* [36,37] characterized the humidity influence on IPMC sensors by statistically investigating sensing signals in typical working conditions based on a linear model. Park [38] conducted the characterization of the solvent evaporation effect on IPMC sensors by using a circuit model and found the optimum level of hydration for a surface-mounted sensor.

In current work we characterize and model the influence of environmental humidity on IPMC sensors from a physical perspective. The proposed dynamic, physics-based model is used to understand the underlying physics of the humidity-dependence for a cantilevered IPMC beam that is subjected to base-excitation inside a custom-built humidity chamber with controlled humidity level. The Young's modulus Y, strain-rate damping coefficient C_s, and viscous air damping coefficient C_a for the mechanical properties, and ionic diffusivity d and dielectric constant κ_e for the mechanoelectrical dynamics are modeled in terms of their humidity-dependence in this dissertation.

1.3 Fabrication of IPMC sensors

1.3.1 Fabrication and Evaluation of Parylene-encapsulated IPMC Sensor

As mentioned above, one critical issue in the practical use of IPMC sensors is that the humidity level of the ambient environment affects the sensing behavior of an IPMC in air [39,40] and thus results in the difficulty of maintaining consistent sensing properties of the IPMC sensor. For some applications not in air, the working environment (such as sea water, acid solution, gasoline *et al.*) could also affect the uniformity of IPMC sensing properties, even cause the IPMC sensor fail to work. For example, the contact resistance between the platinum electrodes and the attached or soldered conductive wire would increase dramatically due to the galvanic corrosion effect in the water. Besides, IPMCs with different cation inside (like Na^+, Li^+, H^+ *et al.*) will display different properties [6,41,42]. If the sensor is exposed to the outside media, the cations inside IPMC will exchange with others gradually, given the fact that the IPMC is made of Nafion (a polymer typically made for ion-exchange purpose). The exposure of the IPMC sensor to some organic solvent will also affect the sensor behavior significantly. Therefore, in order to use the IPMC sensor in practical applications, it is necessary to adopt some measures to ensure its consistent response over time and under different environment. One possible solution to address this challenge is to coat the IPMC with some waterproof materials to suppress the water permeation, and isolate the IPMC from outside media.

A few encapsulation processes have been reported for IPMC actuators. For example, Shahinpoor *et al.* [43] and Akle and Leo [44] proposed the encapsulation of IPMCs using Saran plastic membrane. Franklin [45] reported using Kapton$^{\text{TM}}$ film to cover a multilayer IPMC actuator. Malone and Lipson [46] proposed the use of a PDMS membrane material for IPMC encapsulation. However, encapsulation with these high stiffness materials has increased the IPMC Young's modulus and reduced the IPMC free deflection amplitude, considerably affecting the IPMC performance as actuator and sensor. Recently, IPMC encapsulations with much less stiff materials have been reported. Barramba *et al.* [47] proposed the use of dielectric gel materials as an IPMC encapsulant, which showed a very low stiffness and a high dielectric constant. Kim *et al.* [48] explored coating isotactic polypropylene, silicone rubber and parylene on the IPMC and found that parylene was the most effective coating material to suppress water leakage from IPMC. However, their approaches were primarily focused on IPMC actuators. Experiments have not yet been conducted to verify how these encapsulants maintain the IPMC sensing performance in air, or in other media rather than air.

Besides, Bennett and Leo proposed the use of ionic liquids as solvents for IPMCs in [49]. These liquids are ionic compounds that exist in the form of liquids at low temperatures, and will not be lost to evaporation. IPMCs with ionic liquid as solvent inside can operate in air for a long time. However, IPMCs are not limited in air-operable applications only. We consider applying IPMCs in other media, rather than air exclusively, and find that the encapsulation is still a more general solution to those aforementioned problems.

In this dissertation we propose the use of thick parylene C (up to 25 μm) as an encapsulant for IPMC sensors, which is shown to effectively suppress the water permeation and isolate the sensor from outside media. The proposed fabrication process enables us to control and maintain the hydration level of an encapsulated IPMC sensor to achieve large sensing signal. The water impermeability, mechanical property and corrosion effect of the parylene-encapsulated IPMC sensor are tested by experiments.

1.3.2 Fabrication and Modeling of Novel IPMC Sensors

Reported IPMC sensors are typically in the shape of beams since they are often fabricated using thin Nafion films. Such IPMC sensors only respond to mechanical stimuli in the beam-bending direction (i.e., the direction perpendicular to the beam plane). Recently, several groups have demonstrated IPMC actuators of tubular [50] and cylindrical [51] shapes that can bend in all directions under an appropriate voltage stimulus, but the sensing property of these IPMCs has not been studied. IPMC pipes and their buckling effect have also been reported [52].

In this dissertation, we first present a new fabrication process for the IPMC sensor based on casting and solidification of Nafion solution. This novel sensor has a unique shape of square column, with two pairs of electrodes chemically plated on orthogonal surfaces, and is capable of responding to deflections in any directions on the cross-sections. We first characterize its sensing behavior in air and find that there is strong correlation between the two sensing outputs. We also conduct the modeling for its sensing capability underwater of two-dimensional flow with a two-input-two-output empirical model, which is identified by the empirical frequency responses. The identified model is further verified by the experiment results.

The proposed IPMC sensor with a shape of square column shows strong coupling effect between two routes of sensing outputs, which make it difficult to develop a promising physical model for such a square-column IPMC sensor. Therefore, we further develop a novel, omnidirectional, tubular IPMC sensor that responds to all stimuli perpendicular to the tube axis. With one common inner electrode and four outer electrodes, the tubular IPMC sensor provides four routes of common-ground current outputs. With a custom-made setup, the response of each sensor route is characterized under tip deflection in different orientations at frequencies 1-20 Hz, which verifies the sensor's omnidirectional sensing capability and shows little mechanoelectrical coupling between neighboring sensor routes. An analytical dynamic model, in the form of an infinite-dimensional transfer function, is developed for the sensor, which captures the internal ion-transport physics and the effect of contact resistance. Experimental results show that the proposed model is able to capture the tubular sensor dynamics. Finally, the original model is reduced to a finite-dimensional one, based on which an inversion algorithm is used to reconstruct the mechanical stimulus given the sensor output. The effectiveness of the reconstruction approach is demonstrated experimentally.

1.3.3 Micro-fabrication of Artificial Lateral System Based on IPMC

The biological lateral line system is an important sensory organ for fishes and aquatic amphibians [53, 54], that enables them to perform various animal behaviors, including prey/predator detection [55], rheotaxis [56], schooling [57], courtship and communication [54]. A lateral line system consists of arrays of so called neuromasts, functioning as flow sensors. Each neuromast contains bundles of sensory hairs, encapsulated in a gelatinous structure called cupula. Under an impinging flow, the hairs are deflected, which excites the hair cell neurons and thus enables the animal to identify near-field objects of interest and perform hydrodynamic imaging of the environment. It is of interest to develop artificial lateral line systems for applications in underwater environment. This would provide a new complementary sensing module for the existing sensing mechanisms such as sonar and imaging, and facilitate the control and coordination of underwater robots and vehicles. Lateral line sensors have inspired a lot of work in engineering in the past few years. On the hardware aspect, arrays of flow sensors, explicitly motivated by the biological lateral line, have been fabricated by exploiting various transduction principles, such as hot wire anemometry [58], piezoresistivity [59], and capacitive sensing [60]. Abdulsdda and Tan reported an artificial lateral line based on the sensing capability of ionic polymer-metal composite (IPMC) materials [33]. Also there have been a number of signal processing algorithms proposed for artificial lateral line systems [33, 59, 60].

In this dissertation we propose the use of ionic polymer-metal composite to fabricate an artificial lateral line flow sensor for the direct mechanosensory property and inherent polarity of IPMCs. Three-dimensional IPMC cilia in micro scale will be fabricated, sticking out of a substrate to effectively interact with flows, and thus traditional planar MEMS process is inapplicable. We choose Nafion solution instead of Nafion membrane to create the vertical structure by solidifying the solution within a mold formed by SU-8. Gold-based IPMC fabrication approach, parylene deposition and selective plasma etching are combined to selectively form the electrodes. The microfabrication process is further refined by the double-subtraction approach, and the first prototype is presented with testing results.

1.4 Overview of Contributions

The contributions of this research mainly rely on the dynamic, physics-based model for a base-excited IPMC sensor and the improvement of fabrication of IPMC sensors. The details are as follows.

First, the proposed dynamic model is physics-based with a closed-form expression, combines the vibration dynamics of a flexible beam under base excitation and the ion transport dynamics within an IPMC, and incorporates the effect of a tip mass. An inverse compensation scheme is presented for reconstruction of the base excitation signal given the sensor output. Based on the proposed model, the humidity-dependence of IPMC sensors is characterized and modeled from a physical perspective.

Second, the practical applications of IPMC sensors face with several challenges. To address those challenges, an encapsulated IPMC based on thick parylene coating is fabricated. Various evaluation on the physical properties and sensing properties of this coated sensor is conducted, showing that the parylene encapsulant effectively reduces the water permeation and isolate the sensor from outside media.

Third, two novel types of IPMC sensors capable of omnidirectional sensing are presented. One has a shape of square column, and the fabrication process is based on casting and solidification of Nafion solution; the other is a tubular IPMC fabricated by Nafion tubing. Different from typical

IPMC sensors which respond to deflections in the beam-bending directions only, both sensors are capable of responding to omnidirectional stimulus within the cross-section plane. Their omnidirectional sensing properties are studied. An empirical model and a physical model are proposed for the square column IPMC sensor and the tubular IPMC sensor, respectively.

Last, the proposed micro-fabrication process for IPMC-based artificial lateral line flow sensor is novel. IPMC is the ideal material for developing artificial lateral line flow sensor for the reasons of its direct mechanosensory property and inherent polarity. Several challenges have been addressed in the non-planar solution-based process, and the first prototype is presented.

Chapter 2

Dynamic Modeling of Base-excited IPMC Sensors

We have developed a dynamic model for a base-excited IPMC sensor in air, which comprises a cascade of a mechanical module accounting for the vibration dynamics and an electrical module accounting for the charge dynamics within the IPMC. The model has a closed form and is geometrically scalable. Schemes have been developed to approximate the original infinite-dimensional model with one that is finite-dimensional, to facilitate practical use in sensing and feedback control applications. Experimental results have validated the mechanical vibration model and the overall sensing model. In addition, an inverse compensation scheme has been described and illustrated with simulation results and structural monitoring experiments.

2.1 Model Derivation

2.1.1 Mechanical Dynamics of a Base-excited Cantilever Beam

Consider Fig. 2.1, where the beam is clamped at one end ($z = 0$) and is subjected to a base excitation $u(t)$, producing the bending displacement $w(z,t)$ and a short-circuit sensing current $i(t)$. The neutral axis of the beam is denoted by $x = 0$, and the upper and lower surfaces are denoted by $x = h$ and $x = -h$, respectively. The $y - z$ plane is parallel to the beam plane when the beam is

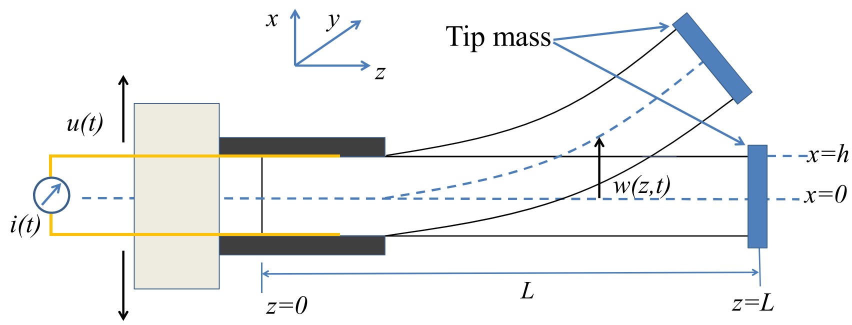

Figure 2.1: Geometric definition of an IPMC beam subjected to base excitation.

not deformed. We consider that a mass of M_L is located at the beam tip $z = L$. We assume that the beam mass and the tip mass are considerably small and their gravity effects are ignored, which implies the skew symmetry of the axial stress. We further assume that the IPMC undergoes small deformation when vibrating, the deformation is restricted to the $x-z$ plane, and the IPMC beam has a considerably smaller thickness $2h$ than its length L and width b. Therefore, the displacement $w(z,t)$ of the beam can be described by the following Euler-Bernoulli beam equation with viscous air damping and strain-rate (or Kelvin-Voigt) damping [61, 62]:

$$YI\frac{\partial^4 w(z,t)}{\partial z^4} + C_s I\frac{\partial^5 w(z,t)}{\partial z^4 \partial t} + C_a\frac{\partial w(z,t)}{\partial t} + m\frac{\partial^2 w(z,t)}{\partial t^2} = 0, \tag{2.1}$$

where Y is the Young's modulus, $I = \frac{2}{3}bh^3$ is the moment of inertia of the beam cross-section , C_a is the viscous air damping coefficient, C_s is the strain-rate damping coefficient, and m is the mass per unit length of the beam. It is a simple approach to use viscous air damping to model the force of air particles that acts on the beam during the vibration. The composite structure of the IPMC is assumed to demonstrate linear-viscoelastic material behavior, hence the strain-rate damping is included in (2.1), accounting for the structural damping due to the internal energy dissipation of the beam. These two mechanisms of damping meet the proportional damping criterion, and for the later model analysis they are also mathematically convenient [62].

Performing the Laplace transform on the time variable t, we convert (2.1) into the Laplace domain:

$$(YI + C_s Is)\frac{\partial^4 W(z,s)}{\partial z^4} + (C_a s + ms^2)W(z,s) = 0, \tag{2.2}$$

where s is the Laplace variable. Eq. (2.2) can be rewritten as

$$\frac{\partial^4 W(z,s)}{\partial z^4} + 4k(s)^4 s^2 W(z,s) = 0, \tag{2.3}$$

where $k(s)^4 = \frac{C_a + ms}{4Is(Y + C_s s)}$. The general solution for (2.3) is

$$\begin{aligned} W(z,s) &= A_1(z,s)\cos(pz)\cosh(pz) + A_2(z,s)\cos(pz)\sinh(pz) \\ &\quad + A_3(z,s)\sin(pz)\cosh(pz) + A_4(z,s)\sin(pz)\sinh(pz), \end{aligned} \tag{2.4}$$

where $p = k\sqrt{s}$. We consider the following boundary conditions (BCs):

$$w(0,t) = u(t), \tag{2.5}$$

$$\frac{\partial w(0,t)}{\partial z} = 0, \tag{2.6}$$

$$I_L \frac{\partial^3 w(L,t)}{\partial t^2 \partial z} + \frac{\partial^2 w(L,t)}{\partial z^2} = 0, \tag{2.7}$$

$$YI \frac{\partial^3 w(L,t)}{\partial z^3} - M_L \frac{\partial^3 w(L,t)}{\partial t^3} = 0, \tag{2.8}$$

or equivalently,

$$\begin{aligned}
W(0,s) &= U(s), &(2.9)\\
\frac{\partial W(0,s)}{\partial z} &= 0, &(2.10)\\
s^2 I_L \frac{\partial W(L,s)}{\partial z} + \frac{\partial^2 W(L,s)}{\partial z^2} &= 0, &(2.11)\\
\frac{\partial^3 W(L,s)}{\partial z^3} - \gamma(s) W(L,s) &= 0, &(2.12)
\end{aligned}$$

where $\gamma(s) = \frac{s^3 M_L}{YI}$, I_L is the moment of inertia of the tip mass about $z = L$. For the geometric boundary conditions at the $z = 0$ (clamped base), the first BC (2.5) means that the base displacement is prescribed by the excitation $u(t)$ ($U(s)$) and (2.6) indicates the fixed slope of zero. For the natural boundary conditions at $z = L$ (free end), the third BC (2.7) indicates the zero bending moment and (2.8) means that the internal shear force is in equilibrium with the force applied by the mass at the tip [62]. The moment of inertia of the tip mass attachment I_L is ignored in (2.7) based on the assumption that the attachment is a point mass right on the tip.

By substituting the boundary conditions into (2.4), we get the following equation for the transformed displacement:

$$W(z,s) = U(s)\frac{N_1(z,s)}{D_1(s)}, \tag{2.13}$$

where

$$
\begin{aligned}
N_1(z,s) = D_1(s)[\cos(pz)\cosh(pz) - \sin(pz)\sinh(pz)G_1(s)] \\
+ [C_1(s) + C_2(s)G_1(s)][\cosh(pz)\sin(pz) - \cos(pz)\sinh(pz)],
\end{aligned} \tag{2.14}
$$

$$C_1(s) = \sin(pL)\sinh(pL), \tag{2.15}$$

$$C_2(s) = \cos(pL)\cosh(pL), \tag{2.16}$$

$$G_1(s) = \frac{\gamma(s)(\sin(2pL) + \sinh(2pL)) + 2p^3(\cosh(2pL) - \cos(2pL))}{\gamma(s)(\sinh(2pL) - \sin(2pL)) + 2p^3(\cos(2pL) + \cosh(2pL) + 2)}, \tag{2.17}$$

$$D_1(s) = \cos(pL)\sinh(pL) + \cosh(pL)\sin(pL). \tag{2.18}$$

Following [61], we can decompose $W(z,s)$ as

$$W(z,s) = W^s(z,s) + W^d(z,s), \tag{2.19}$$

where $W^s(z,s)$ is the quasi-static displacement due to the base motion, $W^s(z,s) = U(s)$, and $W^d(z,s)$ is the dynamic displacement due to dynamic inertial and viscous force effects. The axial strain in the IPMC beam is only produced by $W^d(z,s)$,

$$W^d(z,s) = U(s)\frac{N_1(z,s)}{D_1(s)} - U(s). \tag{2.20}$$

2.1.2 Charge Dynamics in the IPMC

The governing PDE for charge distribution within IPMC was first proposed in [7]. Since the thickness of the IPMC beam is much smaller than its length or width, it can be assumed that the electric field E inside the polymer is restricted to the thickness direction (x-direction) [29].

Following the derivation in [29], we obtain the linearized PDE for the charge density distribution $\rho(x,z,t)$:

$$\frac{\rho(x,z,t)}{\partial t} - d\frac{\partial^2 \rho(x,z,t)}{\partial x^2} + \frac{F^2 dC^-}{\kappa_e RT}(1 - C^- \triangle V)\rho(x,z,t) = 0, \tag{2.21}$$

where d is the ionic diffusivity, F is Faraday's constant, C^- is the anion concentration (mol/m^3), κ_e is the effective dielectric constant of the polymer, R is the gas constant, T is the absolute temperature, and $\triangle V$ is the volumetric change, which represents how much the polymer volume swells after taking water. Since the anions are permanently attached to the backbone structure, C^- is assumed to be spatially homogeneous. Furthermore, in the absence of large changes in the hydration level (as in the context considered in our work), it is reasonable to assume that C^- is a constant. Eq. (2.21) can be converted into the Laplace domain:

$$\frac{\partial^2 \rho(x,z,s)}{\partial x^2} - \beta(s)^2 \rho(x,z,s) = 0, \tag{2.22}$$

where $\beta(s)^2 = \frac{s+K}{d}$ and $K \triangleq \frac{F^2 dC^-}{\kappa_e RT}(1 - C^- \triangle V)$. The general solution of (2.22) takes the form

$$\rho(x,z,s) = a_1(z,s)e^{-\beta(s)x} + a_2(z,s)e^{\beta(s)x}, \tag{2.23}$$

where $a_1(z,s)$ and $a_2(z,s)$ depend on the boundary conditions.

2.1.3 The Sensing Model

Following [28] and [29], we assume that the charge density $\rho(x,z,s)$ is proportional to the mechanically induced stress $\sigma(x,z,s)$ at the boundary $x = \pm h$:

$$\sigma(\pm h, z, s) = \alpha_o \rho(\pm h, z, s), \tag{2.24}$$

where α_o is the charge-stress coupling constant. From the fact $\sigma(h,z,s)+\sigma(-h,z,s)=0$, one gets $\rho(h,z,s)+\rho(-h,z,s)=0$, which implies $a_1(z,s)=-a_2(z,s)$. Consequently, Eq. (2.23) becomes

$$\rho(x,z,s)=2a_2(z,s)\sinh(\beta(s)x). \tag{2.25}$$

We can further relate the stress σ to the external stimulus $U(s)$

$$\sigma(x,z,s)=\frac{M(z,s)x}{I}, \tag{2.26}$$

where $M(z,s)$ denotes the bending moment at z, which can be written as

$$\begin{aligned} M(z,s) &= YI\frac{\partial^2 W^d(z,s)}{\partial z^2} \\ &= YI\frac{U(s)}{D_1(s)}\frac{\partial^2 N_1(z,s)}{\partial z^2}. \end{aligned} \tag{2.27}$$

Define

$$N_2(z,s)\triangleq\frac{\partial^2 N_1(z,s)}{\partial z^2}. \tag{2.28}$$

We can then write

$$\sigma(x,z,s)=\frac{YxU(s)N_2(z,s)}{D_1(s)}. \tag{2.29}$$

Using (2.25) and (2.29) at $x=h$, we can solve for $a_2(z,s)$:

$$a_2(z,s)=\frac{YhU(s)N_2(z,s)}{2\alpha_o D_1(s)\sinh(\beta(s)h)}. \tag{2.30}$$

Finally, let E and ϕ denote the electric field and electric potential, respectively. The following equations hold:

$$E(x,z,s) = -\frac{\partial \phi(x,z,s)}{\partial x},$$
$$\kappa_e \frac{\partial E(x,z,s)}{\partial x} = \rho(x,z,s).$$

With these equations and (2.25), we can solve for $E(x,z,s)$ using the short-circuit boundary condition $\phi(h,z,s) - \phi(-h,z,s) = 0$. Note that here we assume perfectly conducting electrodes for the IPMC. In later experiments, the latter assumption is satisfied by further depositing gold on the electrodes to greatly reduce the surface resistance. The resulting electric field is evaluated as

$$E(x,z,s) = \frac{2a_2(z,s)\cosh(\beta(s)x)}{\kappa_e \beta(s)} - 2a_2(z,s)\frac{\sinh(\beta(s)h)}{\kappa_e h \beta^2(s)}. \tag{2.31}$$

The total induced charge can be obtained by integrating the electric displacement $D = \kappa_e E$ over the beam area at the boundary $x = h$:

$$Q(s) = \frac{bY(\beta(s)h\coth(\beta(s)h) - 1)U(s)}{\alpha_o D_1(s)\beta^2(s)} N_3(s), \tag{2.32}$$

where

$$\begin{aligned} N_3(s) &= \int_0^L N_2(z,s)dz \\ &= 2p(s)[C_1(s) + C_2(s)G_1(s)]\sin(p(s)L)\sinh(p(s)L) \\ &- D_1(s)p(s)[\cosh(p(s)L)\sin(p(s)L)(G_1(s)+1) + \cos(p(s)L)\sinh(p(s)L)(G_1(s)-1)]. \end{aligned}$$

Finally, the transfer function for the sensor, taking the base stimulus $U(s)$ as input and the short-circuit current $I(s)$ as output, is

$$\begin{aligned} H(s) &= \frac{I(s)}{U(s)} = \frac{sQ(s)}{U(s)} \\ &= \frac{bYs(\beta(s)h\coth(\beta(s)h)-1)}{\alpha_o\beta^2(s)}\frac{N_3(s)}{D_1(s)}. \end{aligned} \tag{2.33}$$

For the special case of zero tip mass, $M_L = 0$, $\gamma(s) = 0$, $G_1(s)$ becomes

$$G_1(s) = \frac{\cosh(2p(s)L) - \cos(2p(s)L)}{\cos(2p(s)L) + \cosh(2p(s)L) + 2},$$

and $H(s)$ is evaluated as

$$H(s) = \frac{bYs(\beta(s)h\coth(\beta(s)h)-1)}{\alpha_o\beta^2(s)}\frac{N_3'(s)}{D_1'(s)}, \tag{2.34}$$

where

$$N_3'(s) = 2p(s)[\cos(p(s)L)\sinh(p(s)L) - \cosh(p(s)L)\sin(p(s)L)], \tag{2.35}$$

$$D_1'(s) = \cos(p(s)L)^2 + \cosh(p(s)L)^2. \tag{2.36}$$

2.2 Experimental Model Validation

2.2.1 Experimental Setup

Fig. 2.2 (a) and (b) show the schematic and the picture of the experimental setup, which can provide base excitation for a cantilevered IPMC beam and allow the measurement of base displacement, tip displacement, and the IPMC sensing current. An IPMC beam with a tip mass is clamped at the base by two rigid bars and the bars are fixed on a mini-shaker (Type 4810, Brüel & Kjær), which generates vibration stimulus (up and down) with some controlled frequency. A narrow strip of tape, used as the tip mass, is wrapped around the free end of the IPMC beam. The weight of the tip mass is controlled by the length of the tape strip. In order to verify the beam dynamics and identify some mechanical parameters, two laser displacement sensors (OADM 20I6441/S14F, Baumer Electric) are mounted above the IPMC beam, one measuring the tip displacement while the other measuring the base displacement. The mounting frame for the laser sensors is isolated from the table where the minishaker is mounted. A two-tier amplification circuit is used to measure the short-circuit current generated by the IPMC. Control signal generation, sensing data acquisition, and processing are performed through a dSPACE system (RTI 1104, dSPACE). The IPMC sample used in this study was obtained from Environmental Robots Inc., and then deposited with a layer of gold (0.2 μm thick) on each side in the e-beam physical vapor deposition system (Kurt Lesker AXXIS^{TM} PVD system), which significantly reduced the surface resistance. The dimensions of the sample can be found in Table 2.1. Its surface resistance was reduced from 65 Ω to about 2 Ω after gold deposition, which justifies the assumption of perfectly conducting electrodes used in the modeling part.

2.2.2 Parameter Identification and Model Validation

Table 2.1 lists the physical constants and the parameters obtained through direct measurement. The temperature is read directly from the thermometer in the room. The geometric dimensions, including length, width and thickness, are measured with a vernier caliper. For both width and thickness, multiple measurements are conducted at different points along the IPMC sample, and the average values are adopted. The mass per unit length of the beam is calculated by dividing the weight of the sample, which is obtained with a precision electronic balance, by the sample length.

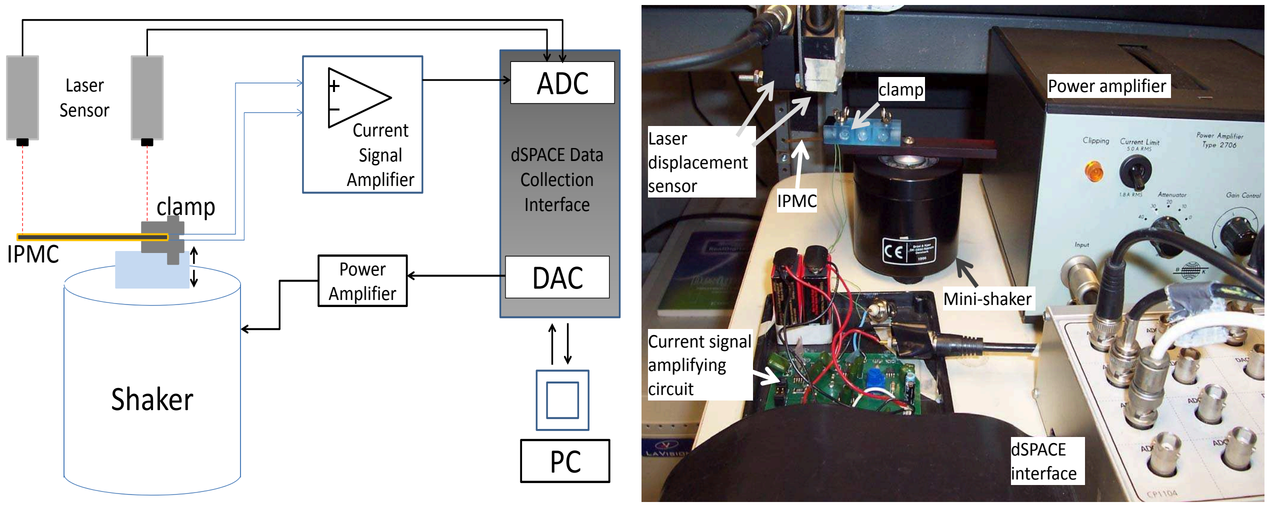

(a) (b)

Figure 2.2: The schematic (a) and photo (b) of the experimental setup for model validation.

The parameters that remain to be determined include the Young's modulus Y, viscous air damping coefficient C_a, strain-rate damping coefficient C_s, diffusion coefficient d, anion concentration C^-, dielectric constant κ_e, and charge-stress coupling constant α_o.

Table 2.1: Physical constants and directly measured parameters.

F (C mol^{-1})	R (J mol^{-1}K^{-1})	T (K)	L (mm)	b (mm)	h (μm)	m (kg/m)
96487	8.3143	300	29.45	6.05	160	3.797×10^{-3}

Considering that there are as many as seven parameters to be identified, it is better to separate the Young's modulus Y, viscous air damping coefficient C_a, and strain-rate damping coefficient C_s from other parameters, and identify these three first, since they can be determined using only the base-excited beam dynamics as shown in (2.13). To be specific, we fix an excitation frequency f and acquire the base vibration $u(t)$ and tip mechanical deformation $w(L,t)$. Both $u(t)$ and $w(L,t)$ are measured by the laser sensors. The amplitudes and phases of these two signals are extracted through fast Fourier transform and then used to compute the magnitude gain and phase shift of the beam dynamics at that particular frequency. Repeating this process for other actuation frequencies results in the empirical frequency response for the beam dynamics. Our experimental setup allows reliable control and signal acquisition for the excitation frequency range of 10 – 150 Hz. The lower frequency bound is determined by the mini-shaker characteristics while the upper bound is determined by the response time of the laser sensors (close to 1 ms). Despite the limitation, this frequency range covers the relevant frequency spectrum of many applications that are of interest. The three parameters Y, C_s and C_a are tuned by curve-fitting the frequency response of the mechanical dynamics using the Matlab function $fminsearch$. Once Y and C_s are identified, they are plugged into $H(s)$ for estimating the four remaining parameters using a similar curve-fitting strategy for the sensing model.

Table 2.2: Identified parameters by curve-fitting.

Y (Pa)	C_a (kg/(m $\cdot$ s))	C_s (Pa s)	d (m^2/s)	C^- (mol/m^3)	κ_e (F/m)	α_o (J/C)
$5.116e8$	0.024	$1.91e5$	$1.973e-15$	1085	$1.07e-3$	94.64

Fig. 2.3 shows the result of curve-fitting for the mechanical model, $W(L,s)/U(s)$, and Fig. 2.4 shows the result of curve-fitting for the sensing model, $H(s)$. For each figure, there are four groups of experimental results, one of which corresponds to the IPMC sample without tip mass, while the other three corresponding to the same sample with different tip masses (10 mg, 20 mg, 30 mg). Only the experimental data without tip mass were used for parameter identification. Then the identified parameters are applied to predict the frequency response of the mechanical and sensing dynamics of the IPMC sensor with different tip masses. All the identified parameters are listed in Table 2.2. Generally they have good agreement with the values reported in the literature [7, 28, 29], while the moderate parameter discrepancies can be explained by the fact that the IPMC sample used in this study is different and is tested in different ambient environments (humidity,

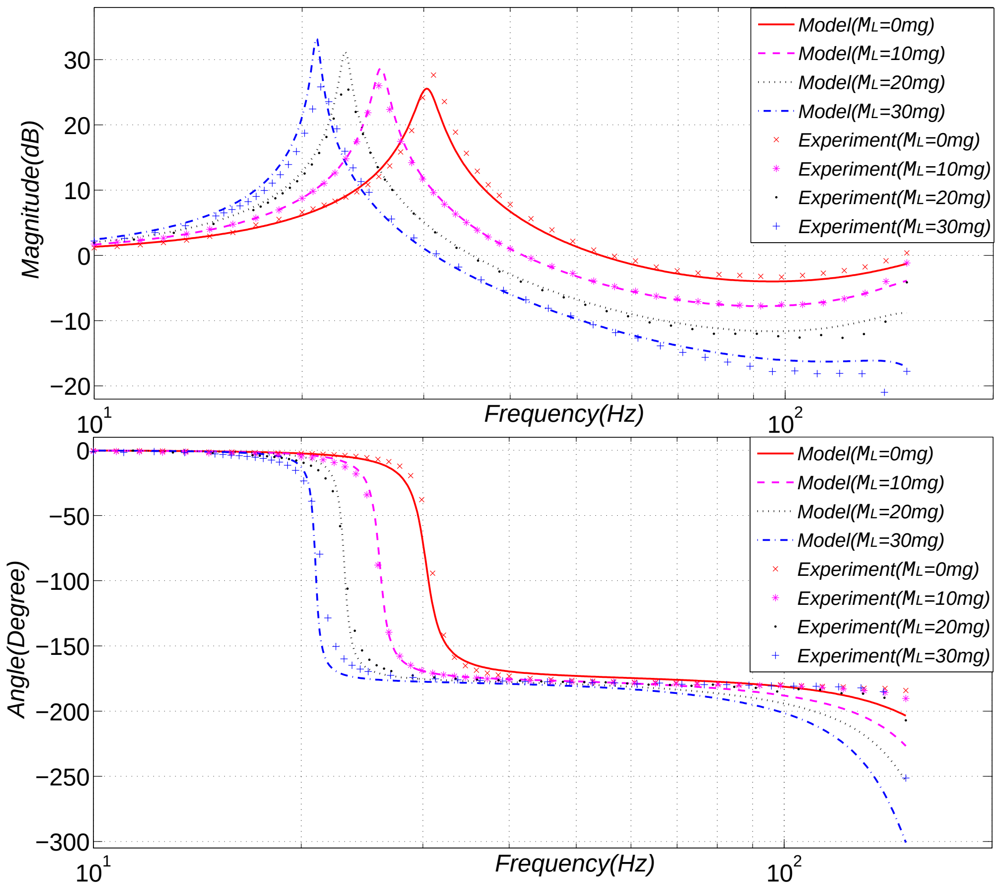

Figure 2.3: Comparison of the measured frequency responses with model predictions for different tip masses (0 mg, 10 mg, 20 mg, 30 mg): Mechanical dynamics (input: base excitation; output: tip displacement).

temperature) from those reported in the literature. The identified in-air damping coefficient C_a is very small and can be neglected without affecting the model prediction too much, which is assumed to be so in some literature [18].

As shown in Fig. 2.3 and Fig. 2.4, although the parameters are fitted based on one group of experiment data in the case of zero tip mass, the model predictions match well the experimental data for all four cases with different tip masses, over the considered frequency range, for both the magnitude and phase responses, which provides strong support for the physical nature of the proposed modeling approach. The discrepancies between the model prediction and the experimental data are attributed to idealistic assumptions in the modeling that are not fully satisfied by the experimental setup, uncertainties in ambient environmental conditions including the temperature and the humidity, and bandwidth limitations of the laser sensors. Both the temperature [63] and the humidity [39] influence the dynamic behavior of an IPMC. There are several approaches that can be adopted to mitigate the impact of environmental variations and improve the model accuracy. For example, one can follow a similar approach proposed in [63] to characterize the temperature/humidity-dependence of the physical parameters, approximate such dependencies with simple functions such as polynomials, and then use auxiliary measurements of temperature and/or humidity to obtain the corresponding parameters. The influence of humidity can also be greatly reduced by encapsulating the IPMC with materials such as parylene to set up barriers against water permeation [64].

Given the Young's modulus and the beam dimensions, the natural frequencies for a based-excited cantilever beam with zero tip mass can be calculated by the following formula:

$$f = \frac{R_{ch}^2}{2\pi}\sqrt{\frac{YI}{mL^4}}, \tag{2.37}$$

where $\mathrm{R_{ch}}$ is the root of the characteristic equation, with the value of 1.8751 and 4.6941 for the first and second mode respectively [65]. By plugging the sample dimensions shown in Table 2.1 and the Young's modulus in Table 2.2 into (2.37), we get the natural frequency of 30 Hz for the first mode vibration of the proposed IPMC sample with zero tip mass and 189 Hz for the second mode. Limited by the response time of the laser displacement sensors, which determines the upper bound of the excitation frequency for reliable motion measurement, the considered frequency range is up to 150 Hz, in which the second mode has also been activated, as can be observed from the magnitude and phase responses beyond 100 Hz in Fig. 2.3. We suspect that the relatively large phase discrepancies between the model and the experimental measurement in the higher frequency

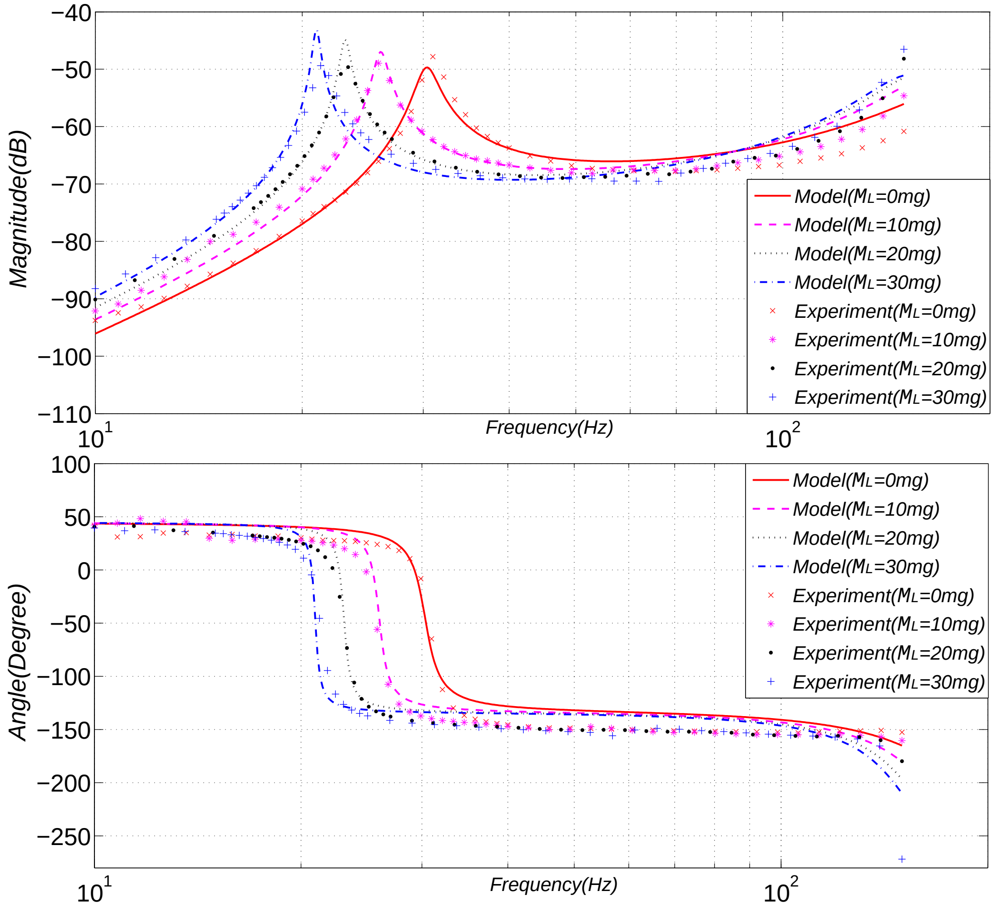

Figure 2.4: Comparison of the measured frequency responses with model predictions for different tip masses (0 mg, 10 mg, 20 mg, 30 mg): Sensing dynamics (input: base excitation; output: IPMC short-circuit current).

range close to 150 Hz are due to the less precise laser measurement.

From Fig. 2.3 and Fig. 2.4 we can clearly see how the tip mass influences the mechanical and sensing dynamics of the IPMC sensor by changing its gain and resonant frequency. In particular, with larger tip mass, the resonant frequency is lower. This observation will be useful for real applications, where one can tune the tip mass to make the resonant frequency close to the dominant frequencies in the excitation stimuli, to maximize the sensor response.

2.3 Model Reduction

The sensing model $H(s)$, shown in (2.33), is infinite-dimensional since it involves non-rational functions such as $\sinh(\cdot)$, $\cosh(\cdot)$,$\sqrt{\cdot}$, etc. For practical use of the model, it is of interest to reduce the model to a finite order. Without losing generality, we will focus on the case of zero tip mass for ease of presentation. We first decompose $H(s)$ as $H(s) = H^E(s) \cdot H^M(s)$, where

$$H^E(s) = \frac{sbY[\beta(s)h\coth(\beta(s)h) - 1]}{\alpha_o \beta^2(s)}, \;\; H^M(s) = \frac{N_3'(s)}{D_1'(s)}. \tag{2.38}$$

Note that H^M and H^E are related to the mechanical and electrical dynamics, respectively. First consider H^E. Since $\left|C^-\Delta V\right| \ll 1$ [7], we take $1 - C^-\Delta V \approx 1$. Based on the physical parameters (see Table 2.1 and Table 2.2 in Section 2.2), for $s = j\omega$, one has $|\beta(s)| = \left|\sqrt{\frac{s+K}{d}}\right| > 10^6$, when the angular frequency ω is relatively low. Furthermore, we have $\coth(\beta(s)h) \approx 1$. $H^E(s)$ can then be simplified as

$$H^E(s) \approx \frac{sbY(\beta(s)h - 1)}{\alpha_o \beta^2(s)} = \frac{sbY\sqrt{d}(\sqrt{s+K}h - \sqrt{d})}{\alpha_o(s+K)}. \tag{2.39}$$

We need to further approximate $\sqrt{s+K}$ with a rational function of s. After comparing with the approximation result using Taylor series expansion, we have found that Padé approximation [66] provides better performance. Given a function of $f(s)$ and two integers $m \geq 0$ and $n \geq 1$, the Padé approximation of order (m/n) around a point s_0 is the rational function $P_{m,n}(s-s_0)$:

$$f(s) \approx P_{m,n}(s-s_0) = \frac{\sum_{l=0}^{m} q_l (s-s_0)^l}{1+\sum_{k=1}^{n} d_k (s-s_0)^k}. \tag{2.40}$$

It is found that the Padé approximation of the order (3/2) can provide adequate approximation with minimal complexity for $\sqrt{s+K}$ around some point s_0, where $s_0 = |j\omega_0|$ and ω_0 is close to the midpoint of the angular frequency range one is interested in. In this dissertation, we take $s_0 = 500$, because the frequency range considered in our experiments is from 10 Hz to 150 Hz.

The resulting finite-dimensional approximation to $H^E(s)$ is

$$\hat{H}^E(s) = \frac{sbY\sqrt{d}}{\alpha_o} \frac{u_3 s^3 + u_2 s^2 + u_1 s + u_0}{r_3 s^3 + r_2 s^2 + r_1 s + r_0}, \tag{2.41}$$

where $u_0, \cdots, u_3$ and $r_0, \cdots, r_3$ are coefficients dependent on K and s_0. The detailed forms of these coefficients are shown in Appendix A.

Now consider the model reduction for $H^M(s) = \frac{N_3'(s)}{D_1'(s)}$. When there is no tip mass, $N_3'(s)$ and $D_1'(s)$ are denoted by (2.35) and (2.36). First, recall

$$\begin{aligned} N_3'(s) &= 2p(s)[\cos(p(s)L)\sinh(p(s)L) - \cosh(p(s)L)\sin(p(s)L)] \\ &= 2\sqrt[4]{r_s}[\cos(\sqrt[4]{r_s}L)\sinh(\sqrt[4]{r_s}L) - \cosh(\sqrt[4]{r_s}L)\sin(\sqrt[4]{r_s}L)], \end{aligned} \tag{2.42}$$

where

$$r_s = \frac{(C_a + ms)s^2}{4Is(Y + C_s s)} = \frac{s(C_a + ms)}{4I(Y + C_s s)}. \tag{2.43}$$

Similarly, one can rewrite $D_1'(s)$ as

$$D_1'(s) = \cosh^2(\sqrt[4]{r_s}L) + \cos^2(\sqrt[4]{r_s}L). \tag{2.44}$$

It is found that good approximation of $H^M(s)$ can be achieved by using Taylor series expansion for $N_3'(s)$ and $D_1'(s)$ separately. Considering up to the second-order Taylor series, which provides satisfactory approximation with minimal complexity, we can get the following approximation to $H^M(s)$ around $r_s = r_0$:

$$\hat{H}^M(s) \approx \frac{b_2(r_s - r_0)^2 + b_1(r_s - r_0) + b_0}{d_2(r_s - r_0)^2 + d_1(r_s - r_0) + d_0}, \tag{2.45}$$

for some coefficients b_0, b_1, b_2 and d_0, d_1, d_2. The detailed expressions for these coefficients are found in Appendix B. Based on the experimental results of parameter identification (see Section 2.2.2), $|r_s|$ is of the order from 10^5 to 10^7, so the value of r_0 can be chosen with large flexibility. Simulation results indicate that any real number of r_0 from 0.01 to 10^6 will give almost the same good approximation results. Without loss of generality, we take $r_0 = 1000$ in this study.

According to the parameter identification result, $C_a << m|s|$, when the frequency is 10 Hz or above, which enables one to make the approximation:

$$r_s \approx \frac{ms^2}{4I(Y + C_s s)}. \tag{2.46}$$

Substituting (2.46) into (2.45), we have

$$\hat{H}^M(s) = \frac{b_2(\frac{ms^2}{4I(Y+C_s s)} - r_0)^2 + b_1(\frac{ms^2}{4I(Y+C_s s)} - r_0) + b_0}{d_2(\frac{ms^2}{4I(Y+C_s s)} - r_0)^2 + d_1(\frac{ms^2}{4I(Y+C_s s)} - r_0) + d_0} = \frac{b_4' s^4 + b_3' s^3 + b_2' s^2 + b_1' s + b_0'}{d_4' s^4 + d_3' s^3 + d_2' s^2 + d_1' s + d_0'}, \tag{2.47}$$

for some coefficients $b_0', \cdots, b_4'$, and $d_0', \cdots, d_4'$. The detailed expressions for these coefficients are found in Appendix B.

Combining (2.41) and (2.47) leads to a reduced model for a based-excited IPMC sensors:

$$\hat{H}(s) = \hat{H}^E(s)\hat{H}^M(s) = \frac{sbY\sqrt{d}}{\alpha_o}\frac{u_3s^3+u_2s^2+u_1s+u_0}{r_3s^3+r_2s^2+r_1s+r_0}\cdot\frac{b_4's^4+b_3's^3+b_2's^2+b_1's+b_0'}{d_4's^4+d_3's^3+d_2's^2+d_1's+d_0'}. \quad (2.48)$$

Note that this reduced model of (2.48) is still a physics-based model and geometrically scalable, since it is expressed in terms of fundamental physical parameters and sample dimensions. Such a characteristic distinguishes this model from other low-order, black-box or grey-box models. Fig. 2.6 shows the comparison of simulation results between the original, infinite-dimensional model $H(s)$ and the reduced model $\hat{H}(s)$, for the IPMC sensor with zero tip mass. From the figure, it can been seen that, although there are some noticeable discrepancies at the high-end of the frequency range, overall the reduction from (2.33) to (2.48) does not produce significant approximation error, indicating the feasibility of the proposed model reduction strategy.

In order to further validate the proposed model and the reduction approach, we have excited the IPMC base with a multi-tone oscillatory signal, which has not been used in the parameter identification process. In particular, the used excitation signal is $u(t) = 0.1742\sin(2\pi\cdot 60t+0.5)+0.1944\sin(2\pi\cdot 80t)+0.0621\sin(2\pi\cdot 100t+1)$ mm. The measured base excitation is fed to the reduced model, to predict the sensing signal in the time domain. Fig. 2.5 shows the comparison between the measured and predicted sensing currents, where one can see that excellent agreement in both magnitude and phase is achieved.The reduced model will be used for reconstructing the base excitation stimulus through inverse compensation.

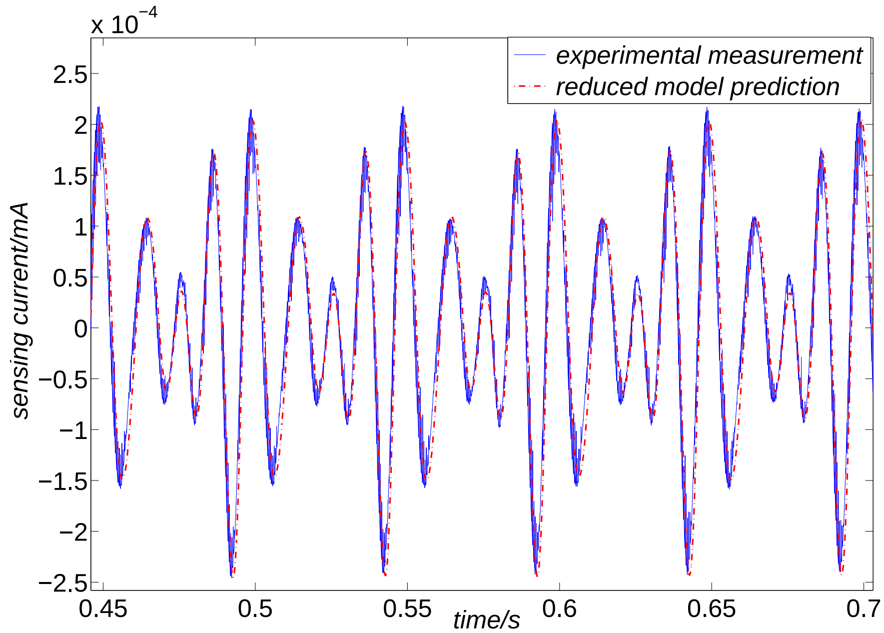

Figure 2.5: Prediction of the sensing response versus experimental measurement under a multi-tone oscillatory excitation, when no tip mass is added.

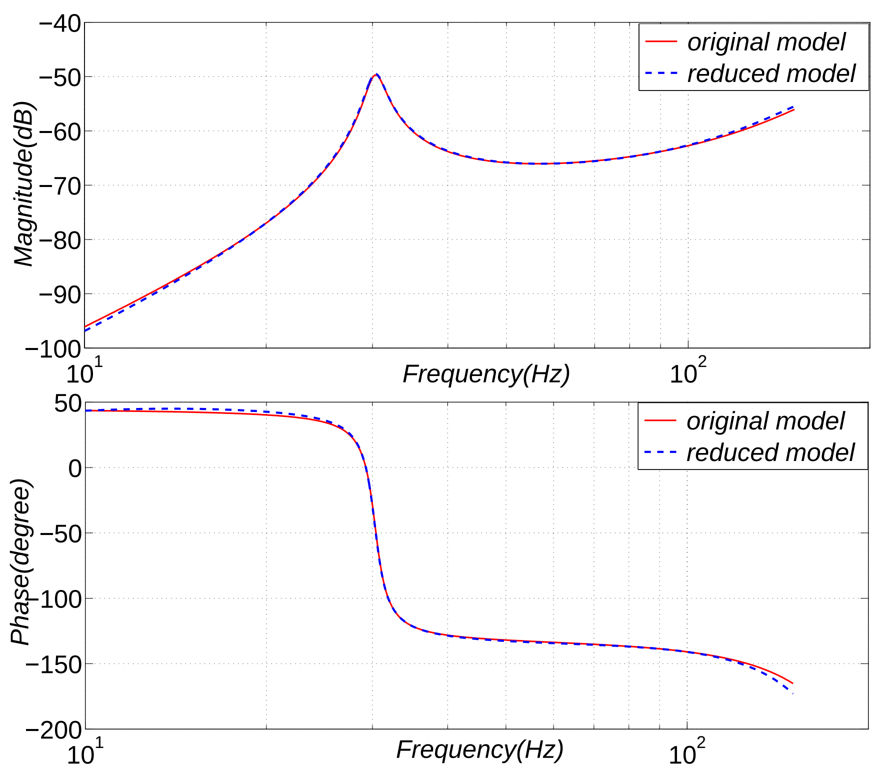

Figure 2.6: Comparison of simulation results between the original model $H(s)$ and the reduced model $\hat{H}(s)$ for the based-excited IPMC sensor.

2.4 Inverse Compensation Scheme

2.4.1 The Inversion Algorithm

An important motivation for deriving a transfer function-type sensing model $H(s)$ for base-excited IPMC sensors is its potential use in structural vibration monitoring. In such applications, we need to infer the underlying mechanical stimulus given the current output of an IPMC sensor. In particular, we are interested in reconstructing the original mechanical signal $u(t)$ based on the sensor output $i(t)$, either online or off-line. Intuitively, the reconstruction can be achieved by inverting the sensing model

$$U(s) = H_{inv}(s)I(s),$$

where $H_{inv}(s)$ represents the inverse dynamics

$$H_{inv}(s) = \frac{1}{\hat{H}(s)}.$$

However, the reduced model $\hat{H}(s)$ obtained is of non-minimum phase (having zeros with positive real parts) and thus the resulting $H_{inv}(s)$ would be unstable and not implementable. For example, based on the parameters in Section 2.2.2 , the resulting transfer function $\hat{H}(s)$ has three stable zeros (-35.98, -500.2, -6965), and one zero at the origin for the mechanoelectric portion of $\hat{H}^E(s)$, and two stable zeros (-1176, -9.38) and two unstable zeros ($+2096$, $+9.413$) for the beam dynamics portion of $\hat{H}^M(s)$. Note that those zeros which are on the origin or close to origin are also problematic for inverse implementation.

In this dissertation, we explore the use of techniques for stable inversion of non-minimum phase systems [63, 67] to reconstruct the base excitation on the IPMC sensor using the sensing current output. It is first assumed that $\hat{H}(s)$ is hyperbolic, meaning that it has no zeros on the imaginary axis. Therefore, the zeros at the origin and close to the origin will be treated separately. The inversion problem is formulated as follows: given the sensor output function $i(t)$, $0 \leq t < \infty$, find the function $u(t)$, $0 \leq t < \infty$, such that

$$i(t) = \hat{H}(s)[u](t), \tag{2.49}$$

where the mixed frequency-time domain notation $\hat{H}(s)[u](t)$ represents the signal obtained by passing $u(\cdot)$ through the system $\hat{H}(s)$. If $\hat{H}(s)$ is a minimum-phase system, the solution $u(t)$ can be computed easily using

$$u(t) = H_{inv}(s)[i](t). \tag{2.50}$$

For a non-minimum phase $\hat{H}(s)$, as in the case of an IPMC sensor, $H_{inv}(s)$ contains unstable poles and thus the algorithm above is not implementable. To solve the inversion problem, we decompose $H_{inv}(s) = H_{\mathrm{s}}(s) + H_{\mathrm{u}}(s)$ where all poles of $H_{\mathrm{s}}(s)$ have negative real parts while all poles of $H_{\mathrm{u}}(s)$ have positive real parts. Note that by the hyperbolic assumption on $\hat{H}(s)$, $H_{inv}(s)$ has no poles on the imaginary axis. The solution $u(t)$ to the inversion problem will correspondingly have two parts: $u(t) = u_{\mathrm{s}}(t) + u_{\mathrm{u}}(t)$, where $u_{\mathrm{s}}(t) = H_{\mathrm{s}}(s)[i](t)$ and $u_{\mathrm{u}}(t)$ is computed as follows; see Fig. 2.7 for illustration.

We first mirror the signal $i(t)$ with respect to $t = 0$ and obtain $\tilde{i}(t) = i(-t)$. Then, we pass the time-reversed signal $\tilde{i}$ through a stable system $\tilde{H}_{\mathrm{u}}(s) \triangleq H_{\mathrm{u}}(-s)$ and get $\tilde{u}_{\mathrm{u}} = \tilde{H}_{\mathrm{u}}(s)[\tilde{i}](t)$. We then obtain u_{u} from $\tilde{u}_{\mathrm{u}}$ by reversing the time again, $u_{\mathrm{u}}(t) = \tilde{u}_{\mathrm{u}}(-t)$. Note that evaluating $u_{\mathrm{u}}(t^*)$ for some t^*, requires knowing $i(t)$, for all $t > t^*$. Therefore, the essence of stable inversion of a non-minimum phase system lies in converting an originally unstable but causal system to a stable but noncausal system. The stable inversion algorithm can be easily adapted so that it requires a finite amount of "preview time" (as opposed to all time into the future) [63, 67], with arbitrarily

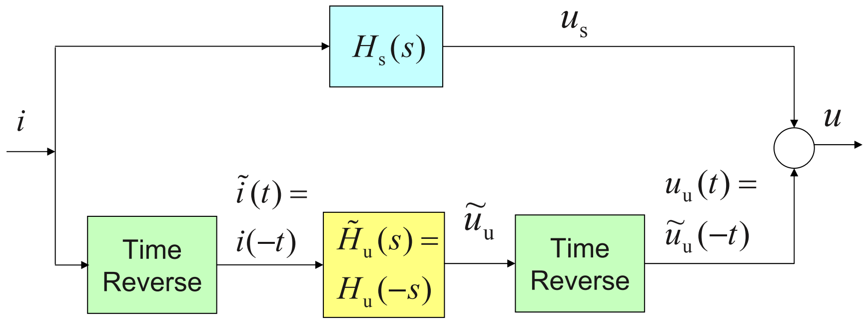

Figure 2.7: Schematic of the stable inversion algorithm for a non-minimum phase system.

small approximation errors.

Finally, we need to deal with the zero of $\hat{H}(s)$ at the origin, we approximate it by $-\varepsilon > 0$. In our implementation, ε is chosen to be -0.1. This is reasonable since $s + 0.1 \approx s$ within the considered frequency range 10–150 Hz.

2.4.2 Simulation Results

The inversion scheme for the reduced model is first illustrated through reconstructing the mechanical excitation from sensing current in simulation. A multi-tone oscillatory base excitation signal is generated, where $u(t) = 0.2\sin(35 \cdot 2\pi t + \pi/3) + 0.1\sin(20 \cdot 2\pi t + \pi/4) + 0.05\sin(15 \cdot 2\pi t)$ mm. The resulting sensing current, evaluated using the reduced model, is then used to infer the base displacement using the proposed inverse compensation scheme. Fig. 2.8 shows that good agreement has been achieved between the predicted and original base excitation signals, indicating that the inverse compensation scheme is effective. The slight mismatch is likely due to the approximation of s by $s + 0.1$, and investigation is underway to understand how to minimize the mismatch.

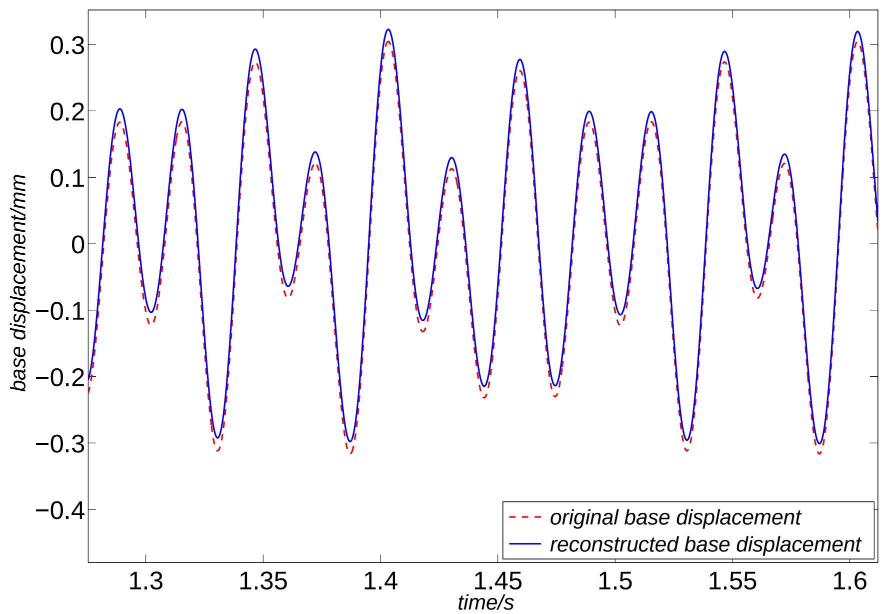

Figure 2.8: Simulation results on the comparison of the base excitation signal reconstructed through model-based inverse compensation with the actual signal.

2.4.3 Structural Vibration Monitoring

2.4.3.1 Experimental Setup

The proposed model and inverse compensation scheme are further validated in structural vibration monitoring experiments. In these experiments, we use the current output of an IPMC sensor to reconstruct the time-domain vibration signal on a mechanical structure. Fig. 2.9 shows the experimental setup. The base of the IPMC beam is attached to an aluminum frame structure. Two types of stimuli are applied to the structure. First, a periodic stimulus is generated by a subwoofer that sits on the aluminum structure. The subwoofer receives oscillatory actuation signals generated from the dSPACE system and produces the corresponding mechanical vibration, which is then transferred to the aluminum frame. The second type of stimulus is an impact, generated by hitting the frame with an iron hammer. A laser displacement sensor is amounted above the base of the IPMC sensor, detecting the actual mechanical displacement at the base. The same current-amplifier circuit in Fig. 2.2 is used to measure the IPMC sensing current. The reconstructed mechanical

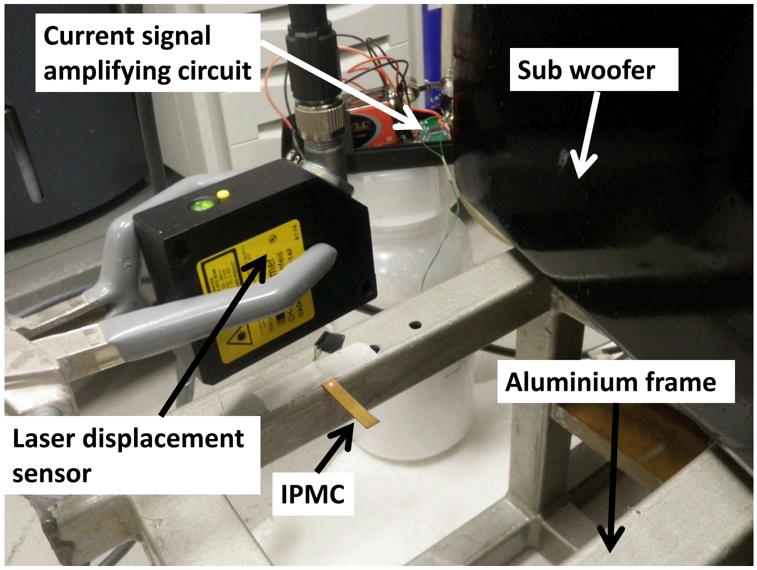

Figure 2.9: Experimental setup for structural vibration monitoring.

stimulus signal will be compared with the measured vibration displacement.

2.4.3.2 Experiment Results

Fig. 2.10 shows the experimental result for the case of a multi-tone oscillatory excitation generated by the subwoofer. As we can see from the figure, there is a reasonable agreement at the steady s-tate between the reconstructed vibration signals and the measured displacement from laser sensor. Fig. 2.11 shows the comparison between the measured base vibration with its sensor-based reconstruction for the case of an impact stimulus, where good agreement is achieved again. Notice that the temperature and the humidity level of the ambient environment in which these experiments are conducted might be different from those for the parameter identification process, which can contribute to the errors between the reconstructed signals and the real measurement. As we discussed in Subsection 2.2.2, impacts of these factors can be mitigated in several ways.

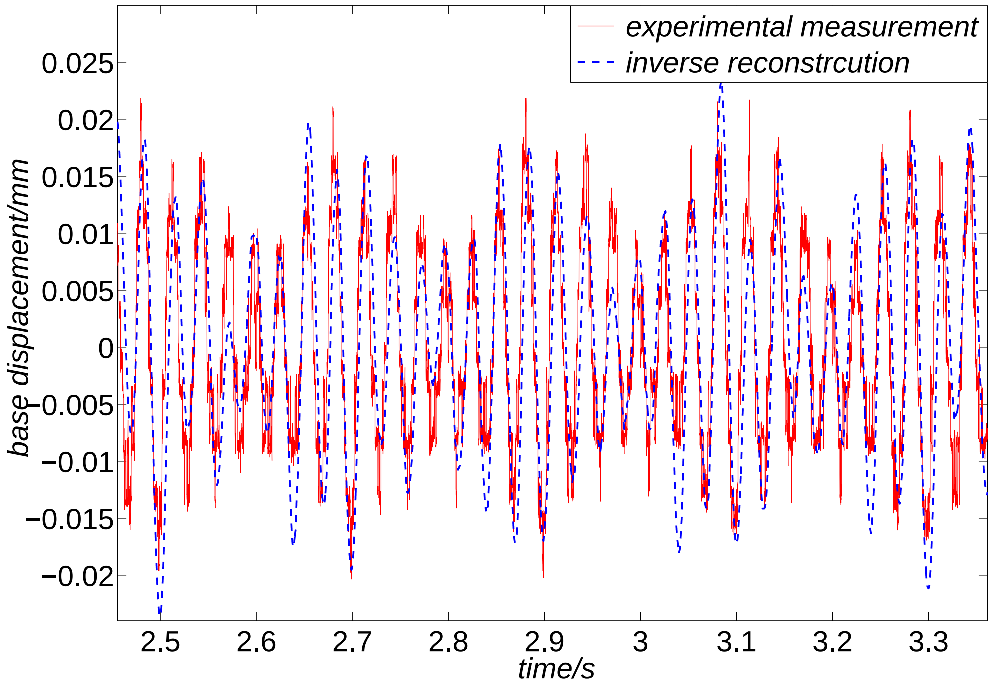

Figure 2.10: Experimental results on structural vibration monitoring: comparison of the reconstructed signal at the base with the actual multi-tone oscillatory excitation.

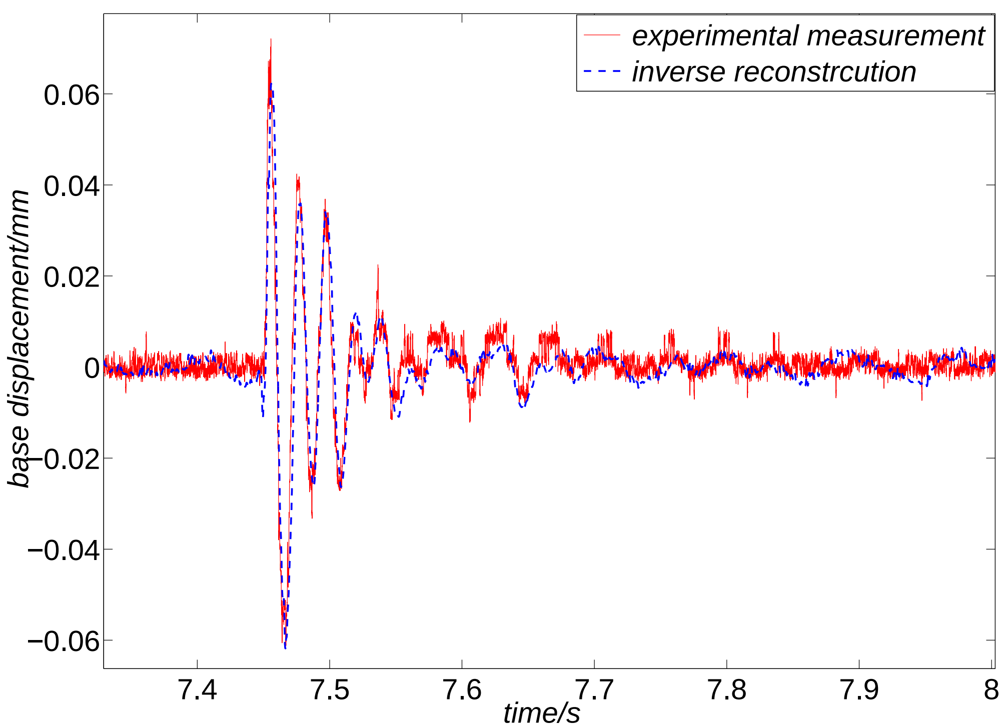

Figure 2.11: Experimental results on structural vibration monitoring: comparison of the reconstructed signal at the base with the actual impact excitation.

Chapter 3

Characterization and Modeling of Humidity-dependence of IPMC Sensing Dynamics

In this chapter, we have characterized and modeled the humidity influence on IPMC sensors from a physical perspective by identifying the humidity-dependence of the physical parameters, including the Young's modulus, strain-rate damping coefficient, viscous air damping coefficient, effective dielectric constant, and ionic diffusivity. The dynamic, physics-based model for base-excited IPMC sensors, which is proposed in Chapter. 2, is used to understand the underlying physics of this humidity dependence. The empirical frequency responses of the sensor under different humidity levels are obtained using a custom-built humidity chamber. Constant-voltage charging experiments of the IPMC sensor are also conducted under each humidity level in the chamber. Data from the charging experiments are directly used to estimate the effective dielectric constant. The rest humidity-dependent physical parameters are identified by curve-fitting the measured frequency responses with the model predictions. These parameters show a clear trend of change with the humidity. We have further modeled the humidity-dependence of the physical parameters with polynomial functions, which are then plugged into the physics-based model to predict the sensing outputs under other humidity conditions. Experimental results have validated the humidity-dependent

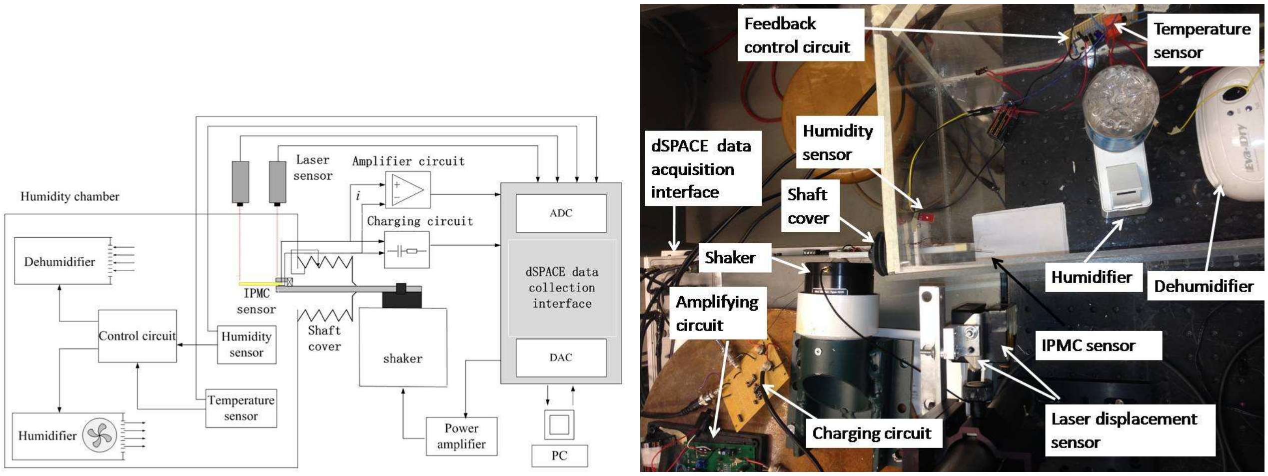

(a) (b)

Figure 3.1: The schematic (a) and photo (b) of the experimental setup.

model.

3.1 Experimental Methods

The humidity-dependence of the IPMC sensor is characterized based on the identification of the humidity-dependent physical parameters of interest at different humidity levels. To create an environment with controlled humidity levels, a customized humidity chamber is built, where the humidity level inside is feedback-controlled by properly activating/deactivating a humidifier or dehumidifier. Under different humidity levels, the empirical frequency responses for the beam dynamics and the sensing output are obtained, and the static charging responses of the IPMC are collected. Then at each given humidity level, the physical parameters are acquired by curve-fitting the measured frequency response with the aforementioned sensing model, except for the effective dielectric constant κ_e, which is identified based on the effective capacitance of the IPMC under static charging.

3.1.1 Experimental Setup

Fig. 3.1 (a) and (b) show the schematic and the picture, respectively, of the experimental setup, including the custom-built humidity chamber which is made of acrylite sheet and well sealed. Inside the chamber, the humidity sensor (HIH-4030, Honeywell) measures the relative humidity (RH) level and sends the results to the data acquisition system (RTI 1104, dSPACE). If the RH level consistently deviates from the preset value, a control signal will be sent to the feedback control circuit inside the chamber, which then turns on/off the humidifier (EMS-200, Stadler Form) or the dehumidifier (EDV1100, Eva-Dry) accordingly. A temperature sensor is also used for monitoring purpose. An IPMC sensor is clamped at the base on a rigid bar which goes through the chamber wall and is fixed on a mini-shaker (Type 4810, Brüel & Kjær). Outside of the humidity chamber, the shaker generates vibration stimulus (up and down) with some controlled frequency. A 3D-printed flexible shaft cover allows the rigid bar to vibrate freely while maintaining good sealing at the same time. In order to identify the mechanical parameters separately, two laser displacement sensors (OADM 20I6441/S14F, Baumer Electric) are mounted above the IPMC beam, one measuring the tip displacement while the other measuring the base displacement. The mounting frame for the laser sensors is isolated from the table where the mini-shaker is mounted. The signal conditioning module consists of a two-tier amplification circuit used to measure the short-circuit sensing current generated by the IPMC in the base-excitation experiments, a current sensor used to measure the charging current in the static charging experiments, and a switch circuit to switch the measurement between sensing current and charging current. Control signal generation, sensing data acquisition, and processing are all performed through the dSPACE system. The IPMC sample used in this study was obtained from Environmental Robots Inc. (Na^+ based), and then deposited with a layer of gold (0.2 μm thick) on each side in the e-beam physical vapor deposition system

(Kurt Lesker AXXIS^{TM} PVD system), which significantly reduced the surface resistance.

Table 3.1 lists the physical constants and the parameters obtained through direct measurement. The temperature and the geometric dimensions are read directly from the temperature sensor and a vernier caliper, respectively. Note that there are two values for both the thickness and the mass per unit length. For each case, the first value was obtained by measuring the sample at 0% RH level and the second one at 100% RH level. Assuming that the change of the thickness and the mass per unit length is linear with the RH level, we use linearly humidity-dependent h and m for the rest of the discussion to minimize the influence of varying geometry and weight of the IPMC sensor caused by the different humidity levels. For the length L and width b, there are much less noticeable changes in their measurement, hence they are treated as constants in this study.

Table 3.1: Physical constants and directly measured parameters.

F (C/mol)	R (J mol^{-1}K^{-1})	T (K)	L (mm)
96487	8.3143	293	27.68
b (mm)	h (μm)	m (g/m)	
5.26	130-150	$3.48-3.68$	

3.1.2 Parameter Identification

To investigate the IPMC sensing dynamics under different humidity levels, experiments for the base-excitation and the static charging are repeated at varying RH levels ranging from 38% to 80%. The lower bound of RH levels is determined by the capability of the dehumidifier and the sealing of the humidity chamber, while the upper bound is determined by the measuring limitation of laser sensors (the chamber wall loses transparency under high RH levels). At each testing RH level, the IPMC sample is first base-excited under a sweep frequency ranging from 10 to 150 Hz, followed by switching off the circuit for the base-excitation experiment. After stabilization for $10s$, the circuit for the static charging experiment is switched on and the charging current of the IPMC is collected. By switching on/off the measurement circuit for sensing current or charging current, the electrical correlation between the two measurements is minimized. It takes $80s$ to complete both of the experiments, during which the RH level inside the chamber is controlled to maintain consistent. The lower frequency bound is determined by the mini-shaker characteristics and the base-excitation configuration (sensing signal is weak under low frequency), while the upper bound is determined by the response time of the laser displacement sensors (close to 1 ms). Despite the experimental limitation, the test range of RH level and vibration frequency covers many applications that are of interest.

The Young's modulus Y, strain-rate damping coefficient C_s, and viscous air damping coefficient C_a are first identified by the empirical frequency response for the beam dynamics with the IPMC base displacement $u(t)$ as input and the tip displacement $w(L,t)$ as output, as shown in (2.13). Both $u(t)$ and $w(L,t)$ are measured by the laser sensors. To be specific, we fix an excitation frequency f and acquire $u(t)$ and $w(L,t)$. Fast Fourier transform (FFT) is performed on $u(t)$ and $w(L,t)$ to extract the amplitudes and phases of these two signals, which are then used to compute the magnitude gain and phase shift of the beam dynamics at that particular frequency. By repeating this process for other vibration frequencies, we obtains the empirical frequency response for the beam dynamics. Since the viscous air damping coefficient C_a is much smaller than Y and C_s, C_a is first assumed to be zero; then the two parameters Y and C_s are tuned by curve-fitting the frequency response of the mechanical dynamics using the Matlab function *fminsearch*. Next, the fitted values of Y and C_s are used as the initial values for a new run of curve-fitting which includes Y, C_s, and C_a together. By estimating the three mechanical parameters in this way, we can avoid local optimal solutions of *fminsearch*. One result of curve-fitting under RH of 68% is shown in Fig. 3.2.

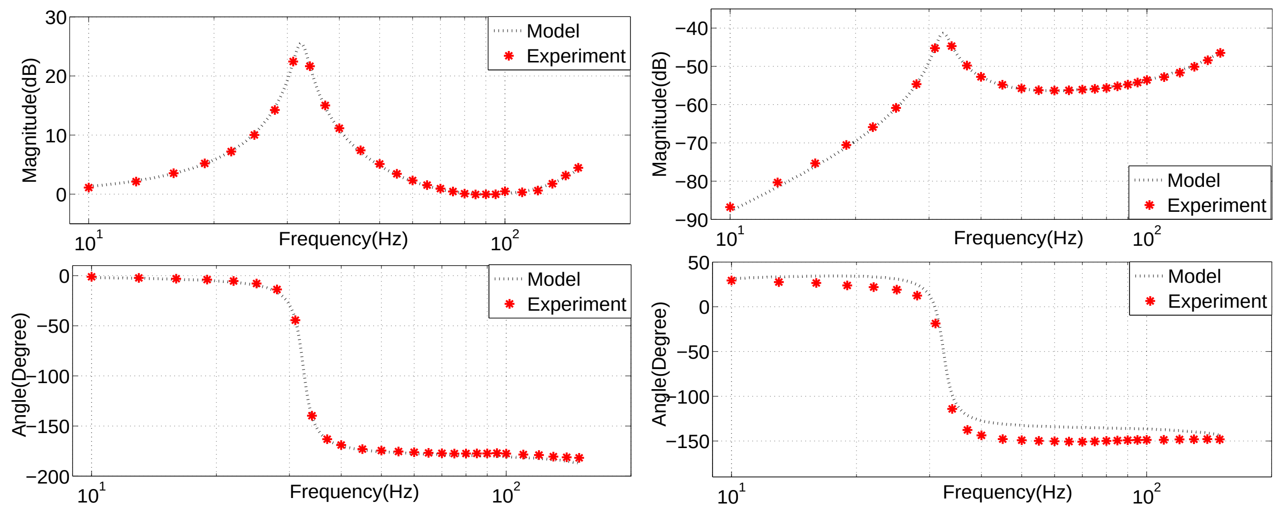

(a) (b)

Figure 3.2: Comparison of the measured frequency response with model predictions (with identified parameters) under relative humidity of 68% for: (a) beam dynamics (input: base excitation; output: tip displacement); (b) sensing dynamics (input: base excitation; output: IPMC short-circuit current).

The effective dielectric constant κ_e is identified through the constant-voltage charging process, where a voltage of 0.1V is used. IPMC can be seen as a parallel-plate capacitor which contains the hydrated polymer that completely fills the space between the plates, and the capacitance is given by: $C_{cap} = \kappa_e \frac{WL}{2h}$ [68]. Therefore, κ_e can be calculated via $\kappa_e = C_{cap}\frac{2h}{WL}$ with $C_{cap} = \frac{Q_c}{U_c}$, where U_c is the fixed charging voltage and the accumulated charge Q_c is measured by integrating the charing current. Once Y, C_s, C_a and κ_e are identified, they are plugged into the sensing model $H(s)$ for estimating the remaining parameters (see below) using a similar curve-fitting strategy.

3.2 Results and Discussion

There are eight physical parameters in total in the sensing model $H(s)$, of which three (Y, C_s, and C_a) are from the beam dynamics in (2.1), four ($\triangle V$, C^-, d, and κ_e) are from the charge dynamics in (2.21), and one (α_o) is from the assumption in [7,28]. For those four parameters from the charge

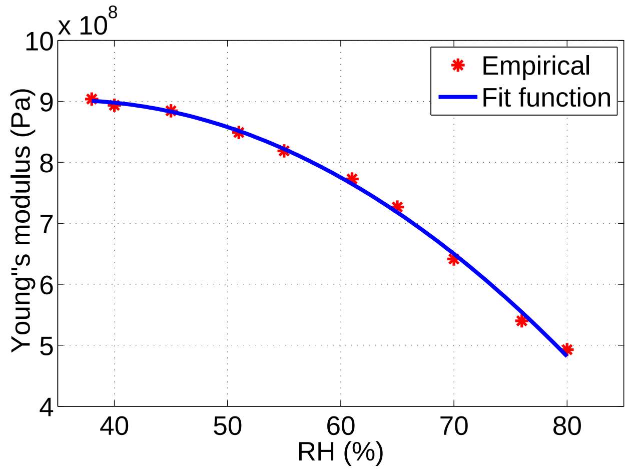

Figure 3.3: Fitting functions for Young's modulus Y.

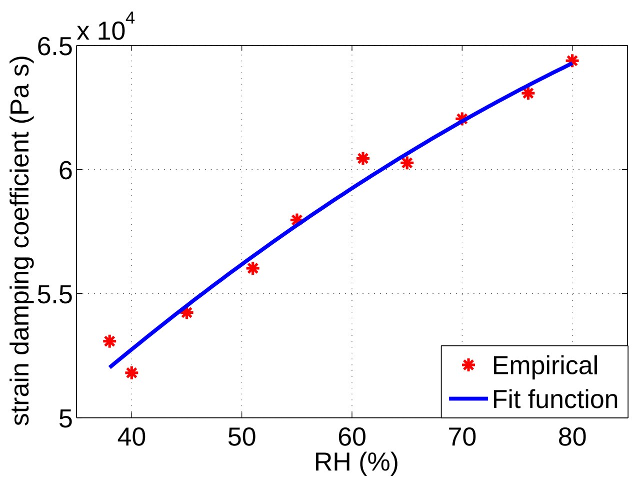

Figure 3.4: Fitting functions for strain-rate damping coefficient C_s.

dynamics and the charge-stress coupling constant α_o, we only focus on the discussion on the ionic diffusivity d and the dielectric constant κ_e, both of which have explicit physical properties and have showed considerably large humidity-dependence in the experimental results. Since $\left|C^{-}\Delta V\right| \ll 1$ [7], we take $1 - C^{-}\Delta V \approx 1$, thus the volumetric change $\triangle V$ is ignored in the sensing model $H(s)$. Instead, the volumetric change is taken into account by using the linear humidity-dependent linearly humidity-dependent h and m (see Table 3.1). The anion concentration and charge-stress coupling coefficient did not show clear dependence on humidity in our experiments and are thus treated as constants (94.64 J/C).

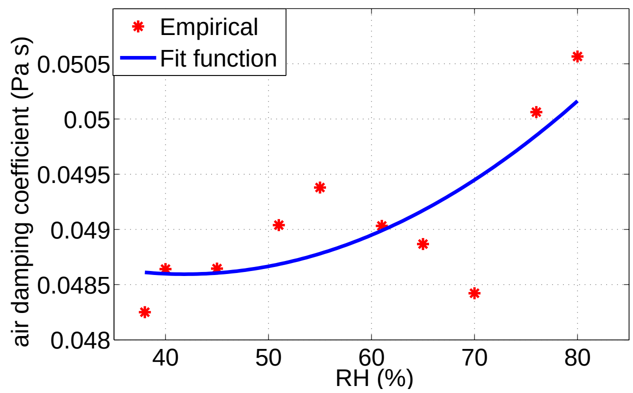

Figure 3.5: Fitting functions for viscous air damping coefficient C_a.

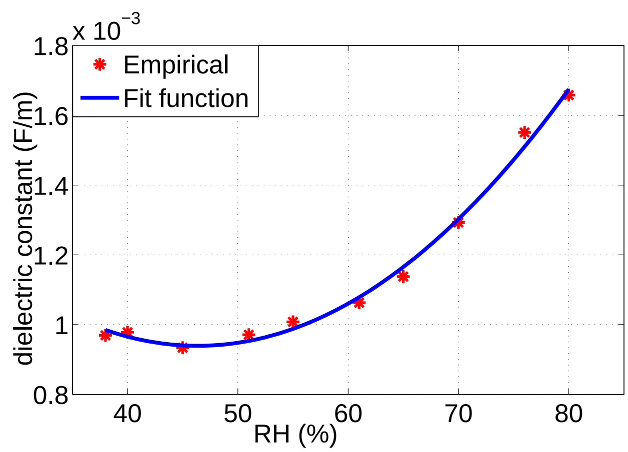

Figure 3.6: Fitting functions for dielectric constant *ke*.

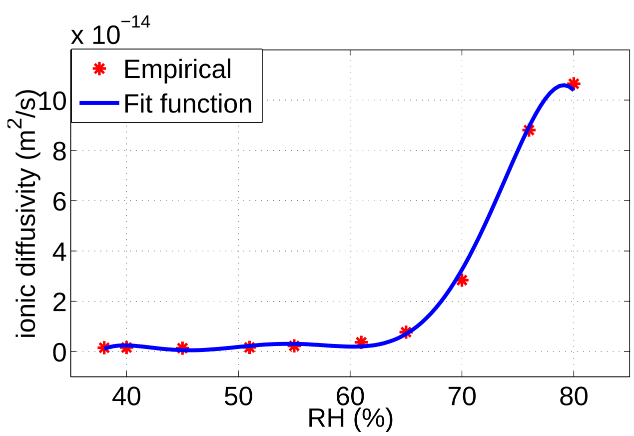

Figure 3.7: Fitting functions for ionic diffusivity d.

3.2.1 Humidity-dependent Parameters

Fig. 3.3 to Fig. 3.7 show the identified five physical parameters corresponding to a set of ten relative humidity levels (38% and from 40% to 80% with each increment of 5%). By fitting the values of each parameter at different RH levels with the least-square method (”polyfit” function in Matlab), we obtain low-order polynomial functions of the RH (ranging from 38% to 80%) for these five parameters. To be specific, Fig. 3.3 shows the identified Young's modulus Y at different relative humidity levels (denoted as ϕ_r), along with the approximating quadratic function

$$Y(\phi_r) = -2.134\times10^5\phi_r^2 + 1.521\times10^7\phi_r + 6.309\times10^8, \tag{3.1}$$

Fig. 3.4 shows the identified strain-rate damping coefficient C_s along with the approximation by the quadratic function

$$C_s(\phi_r) = -1.812\phi_r^2 + 5.057\times10^2\phi_r + 3.542\times10^4, \tag{3.2}$$

Fig. 3.5 shows the identified viscous air damping coefficient C_a along with the approximation by the quadratic function

$$C_a(\phi_r) = 1.080\times10^{-6}\phi_r^2 - 9.044\times10^{-5}\phi_r + 0.051, \tag{3.3}$$

Fig. 3.6 shows the measured effective dielectric constant κ_e along with the approximation by the quadratic function

$$ke(\phi_r) = 6.499\times10^{-7}\phi_r^2 - 6.026\times10^{-5}\phi_r + 0.0023, \tag{3.4}$$

and Fig. 3.7 shows the estimated ionic diffusivity d along with the approximation by the six-order polynomial function

$$
\begin{aligned}
& d(\phi_r) = -1.285\times10^{-21}\phi_r^6 + 4.307\times10^{-19}\phi_r^5 \\
& -5.928\times10^{-17}\phi_r^4 + 4.291\times10^{-15}\phi_r^3 - 1.724\times10^{-13}\phi_r^2 \\
& +3.645\times10^{-12}\phi_r - 3.1713\times10^{-11}.
\end{aligned}
\tag{3.5}
$$

Among those three parameters (Y, C_s, C_a) which were identified through beam dynamics, the Young's modulus Y and the strain-rate damping coefficient C_s continuously decreases and increases, respectively, as the humidity level goes up. Based on the understanding of their physical characteristics, it is reasonable to have such observation for Y and C_s. Young's modulus is a measure of the material stiffness, and is expected to drop when the material becomes softer under increasing RH levels. Strain-rate damping accounts for the structural damping due to the internal energy dissipation of the beam. When the beam absorbs more water moisture into its polymer structure, the internal energy dissipation is expected to be faster, thus the damping coefficient C_s becomes larger. The air viscous damping coefficient C_a is also expected to increase with the RH level. While Fig. 3.5 shows that the identified C_a overall shows an increasing trend, the values between 60%-70% RH seem to be deviating from this trend. While the exact explanation for this phenomenon is still under investigation, we believe that the relatively weak contribution of the air viscous damping in the beam dynamics equation (2.1) reinforces the randomness of the identified C_a through curve-fitting with the non-ideal experimental conditions..

The effective dielectric constant κ_e is directly measured through the constant-voltage charging process, during which the IPMC sensor is treated as a parallel-plate capacitor containing the hydrated ionic polymer as the dielectric. Since the dielectric constant of water is larger than that of the ionic polymer, it is expected to see that κ_e continuously increases when the RH level goes up. Similarly, for ionic diffusivity d, it is straight forward to expect continual growth when the humidity level increases. The general trends of the identified parameters in Fig. 3.6 and Fig. 3.7 are consistent with these expectations. It can be seen in Fig. 3.7, d grows very slowly at the RH levels less than 60%. Beyond this point, d starts to keep increasing quickly. Note that the ionic diffusivity d varies in a relatively large range from the scale of 10^{-15} to 10^{-13}; therefore, a high-order polynomial function is used to approximate it.

3.2.2 Validation of Humidity-dependent Model

To verify its prediction capability, we construct the humidity-dependent models for beam dynamics (2.13) and IPMC sensing (2.33) at the relative humidity of 68% based on the humidity-dependent parameters of $Y(\phi_r)$, $C_s(\phi_r)$, $C_a(\phi_r)$, $ke(\phi_r)$, and $d(\phi_r)$ evaluated at $\phi_r = 68$, respectively, based on (3.1), (3.2), (3.3), (3.4), and (3.5). Note that $68\%RH$ was chosen arbitrarily, but not used in data-fitting for approximating the polynomial functions. We have also constructed the similar models based on some fixed parameters, which were parameters identified under the RH level of 45%. $45\%RH$ was also chosen arbitrarily and for comparison purpose only. These models are denoted as humidity-independent models. Fig. 3.8 shows the comparison of beam dynamics between the measured frequency response and the two predicted frequency responses based on the humidity-dependent models and humidity-independent models, and Fig. 3.9 shows the comparison of sensing dynamics. It can be seen from both figures that good agreement is achieved both in magnitude gain and phase shift between the experimental measurement and the prediction of the humidity-dependent model, but the prediction of the humidity-independent model shows large discrepancy from the measured frequency response, indicating that the proposed modeling approach is effective in capturing the humidity-dependent mechanical and sensing dynamics for IPMC.

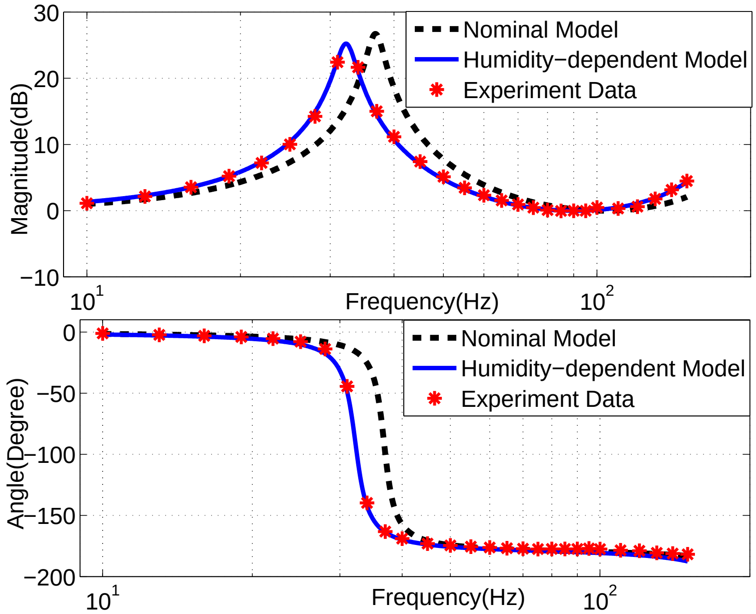

Figure 3.8: Comparison of the measured frequency responses of beam dynamics with the two model predictions at the relative humidity of 68%. The base displacement and the tip displacement are the input and output of the system, respectively.

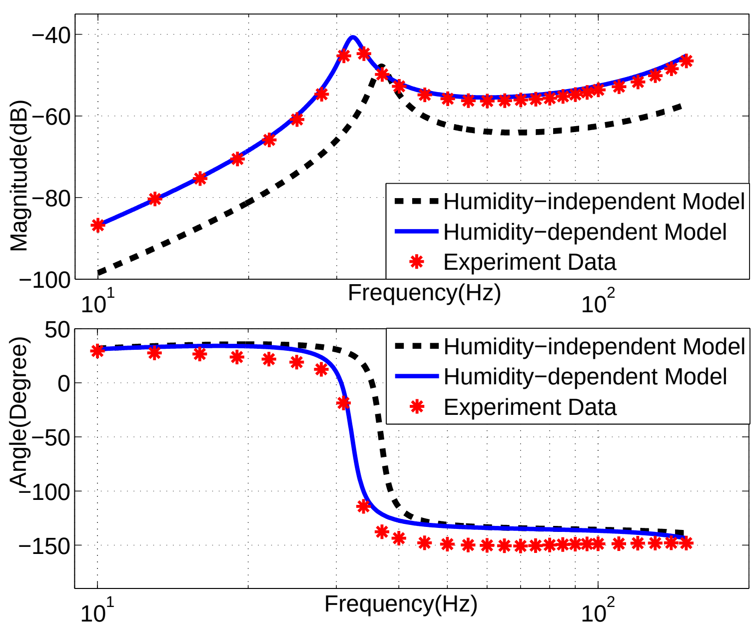

Figure 3.9: Comparison of the measured frequency responses of sensing with the two model predictions at the relative humidity of 68%. The base displacement and the short-circuit current are the input and output of the system, respectively.

Chapter 4

Fabrication and Evaluation of Parylene-encapsulated IPMC Sensor

In this chapter we have investigated the performance of encapsulated IPMC sensors based on thick parylene C coating. To solve the problem of water evaporation inside the parylene deposition chamber and control the hydration level of the IPMC sensor, the proposed fabrication process features thick parylene coating and adjustable water drive-in process. The stiffness of the IPMC sensor before and after the encapsulation is measured to investigate the sensor's mechanical property. The water impermeability of the parylene encapsulated sample is tested under heating and soaking conditions, respectively, and compared with the uncoated sample. The control of hydration level by water drive-in step is proven to help adjust the resonance frequency of the parylene-encapsulated IPMC sensor to achieve larger sensing outputs in different applications.

The galvanic metal corrosion on IPMC sensors in water is introduced and evaluated by experiments in terms of the contact resistance. Experiments have also been conducted to evaluate the performance of the coated IPMC sensor in a humidity chamber with controlled humidity levels, in solutions with different cations, and in two organic solvents. Experimental results show that the proposed thick parylene encapsulation can effectively keep the water content inside the IPMC, isolate the IPMC sensor from various ambient environments, and maintain the sensing consistency, which allows IPMC sensors to be used in more practical applications.

4.1 Fabrication Process

4.1.1 Coating Material

Parylene C was adopted as the encapsulation material for the following three reasons. First, parylene C is well known for its effectiveness as water barrier because it has very low water vapor transmission rate (WVTR), as shown in Tab. 4.1. The reported WVTRs were measured under certain conditions of temperatures, relative humidities (RH), and thicknesses of thin films. Note that the WVTR is not identical for different thicknesses of parylene films. For example, the actual WVTR for 25 μm thick parylene should be much smaller than that measured with 8 μm. The WVTR at 20 °C, 30% RH and WVTR at 20 °C, 90% RH from [69] are used in this study to estimate the water permeation of parylene encapsulation in air and in water respectively, as shown in Tab. 4.2. Second, the Young's modulus of parylene C is only 0.4 MPa, which would minimize the influence of the encapsulation layer on the IPMC sensor stiffness and thus the sensitivity, considering that the Young's modulus of a typical IPMC sample is around 300 MPa [29]. Finally, parylene deposition is conducted in a chemical vapor deposition (CVD) system at room temperature, which enables conformal, uniform and true pin-hole-free coating on surfaces with various geometries. Compared with other encapsulation approaches reported in the literature, the CVD system offers the advantage of accurately controlling the deposition thickness and rate. The deposition process is also compatible with standard microfabrication technologies, which makes it possible to integrate high-density IPMC sensor arrays with electronics on a single platform.

4.1.2 IPMC Sensor Fabrication

IPMC sensors were fabricated with the traditional impregnation-reduction ion-exchange process [6]. Nafion-1110 (254 μm) films from Dupont were first roughened with fine sandpapers. The

Table 4.1: Reported water vapor transmission rate (WVTR) for parylene C. The unit is $(\mathrm{g}\cdot\mathrm{mil})/(100\mathrm{in}^2\cdot\mathrm{day})$, where mil and $100\mathrm{in}^2$ refer to the thickness and the size of the membrane, respectively.

WVTR of parylene C $(\mathrm{g}\cdot\mathrm{mil})/(100\mathrm{in}^2\cdot\mathrm{day})$	WVTR at 37 °C, 90% RH	WVTR at 20 °C, 90% RH	WVTR at 20 °C, 30% RH
Hubbel *et al.* [70]	3.3-7.3	N/A	N/A
Loeb *et al.* (Union Carbide) [71]	0.5	N/A	N/A
Specialty Coating System, Inc.	0.2031	N/A	N/A
P.R. Menon *et al.* [69]	0.207	0.08675	0.04515

Table 4.2: Estimated water permeation for encapsulated IPMC sensor, where the parylene layer is assumed to be 10 μm (0.394 mil). The size of the IPMC is 0.626 inch $\times$ 0.121 inch and the weight is 32 mg. Note that the encapsulation area is computed as $2\times$ length $\times$ width.

Encapsulated IPMC sensor	WVTR $(\mathrm{g}\cdot\mathrm{mil})/(100\mathrm{in}^2\cdot\mathrm{day})$	Water permeation rate (mg/day)	Water permeation (wt%)
in air	0.04515	0.1736	0.5425
in water	0.08675	0.3338	1.0431

residues on the film were removed with ultrasonic cleaner. The films were boiled in dilute 2 wt% hydrochloric acid for 30 min to remove ions and impurities. Then the films were boiled in deionized (DI) water for another 30 min to remove the acid and swell the films, and immersed in a platinum complex solution ($[Pt(NH_3)_4]Cl_2$) for more than 12 h to allow Pt ions to completely diffuse into the Nafion films through the ion-exchange process. After that, the films were rinsed with DI water and immersed in a water bath at 40 °C. We then added 2 ml of sodium borohydride solution (5 wt% $NaBH_4$ aq) as the reducing agent every 30 min when the temperature went up to 60 °C gradually. Once the platinum deposition was complete, the films were cut into beam-shaped samples with proper sizes. Finally, an IPMC sensor was formed by soldering two electric wire connectors to the IPMC platinum electrodes.

4.1.3 Parylene Encapsulation

Parylene encapsulation was conducted with a parylene coater (PDS2035, Specialty Coating System, Inc.), where parylene C was deposited conformally on the IPMC sensors under a low pressure of 30mTorr. The adhesion between the parylene and the platinum electrodes can be improved by plasma treatment. Please refer to [48] for more details. According to the experimental results reported in [48], IPMC samples with 1 μm thickness of parylene coating still had complete water swelling when soaked in water for 24 h, showing that 1 μm thickness of parylene encapsulation failed to isolate the IPMC from outside media effectively. It was reported in [72] and [73] that 8 μm might be a threshold value for the thickness of the parylene C film in terms of whether the film would be affected by defects or not. Thus, thick parylene coatings larger than 10 μm were selected for the proposed encapsulation process.

IPMC sensors need ionic hydration to operate; however, it is challenging to deposit parylene on IPMC while maintaining the moisture inside, because the water molecules will evaporate completely in the deposition chamber under the low pressure. To address this challenge and furthermore, to control the hydration level inside the encapsulated IPMC, we propose a novel fabrication recipe that consists of parylene deposition and water drive-in processes, as shown in Fig. 4.1. Based on the reported data in Tab. 4.1, the WVTR of parylene C is greatly affected by the temperature. Under the room temperature, parylene has excellent water barrier capability; but when the temperature goes up to 37 °C, the WVTR almost doubles. The water drive-in process was realized by taking advantage of this temperature effect: after the parylene deposition, the encapsulated IPMC sensors were soaked in a hot water bath of 80 °C for sufficient time. During this process, the water molecules diffused through the parylene layer with a high WVTR and hydrated the IPMC sensor. The hydration level was controlled by the water bath temperature and the length of soaking time,

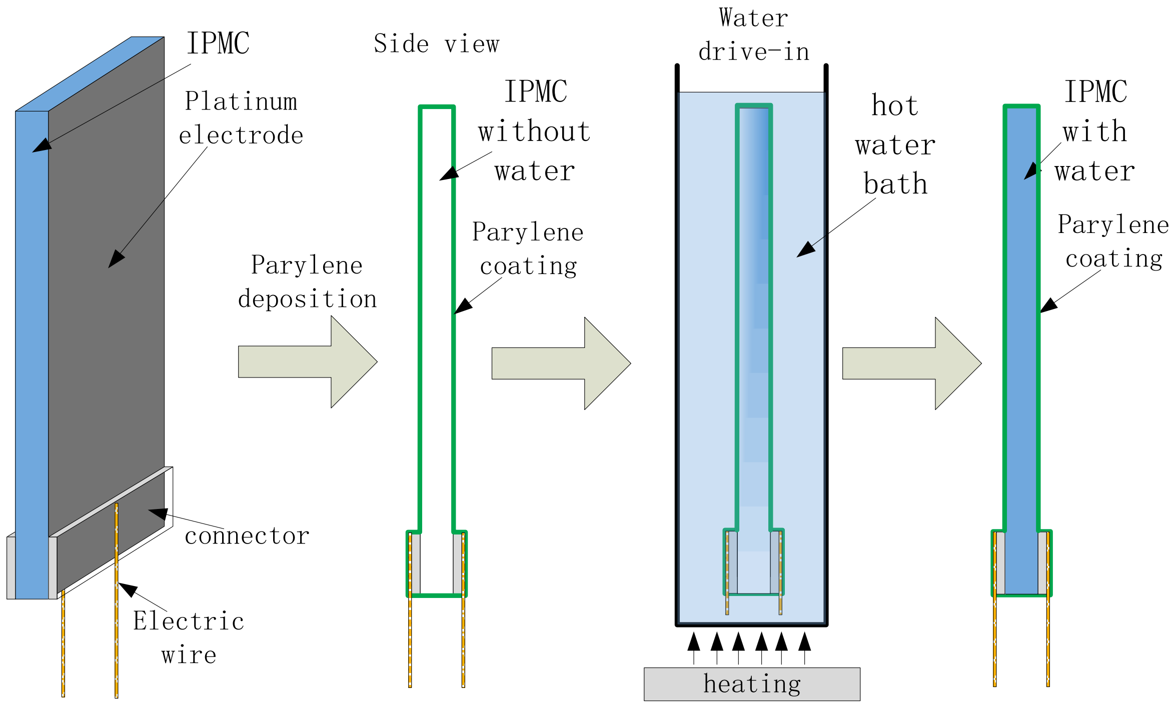

Figure 4.1: Fabrication procedure for encapsulated IPMC sensor.

and thus we can adjust the water content inside the IPMC sensor so that the best sensitivity can be achieved. After the water drive-in process is finished, the diffused water molecules will be sealed inside by the encapsulation layer under the room temperature. Fig. 4.2 shows the experimental result for the water drive-in process for three parylene-encapsulated IPMCs (with 25 μm parylene coating) submerged in hot water baths under 60 °C, 70 °C and 80 °C, respectively. The value of the water content is obtained by weighing the IPMC sample before and after the soaking. It can be seen that the proposed drive-in process gives a nearly linear relationship between the soaking time and the increased weight when the hydration level is relatively low, indicating the feasibility of using this method to hydrate and re-hydrate a coated IPMC sensor. From Fig. 4.2, one can also see that the rate of water drive-in shows a pronounced dependence on the bath temperature, as one would expect.

Evaluation of the parylene-encapsulated IPMCs has been conducted on four aspects: physical

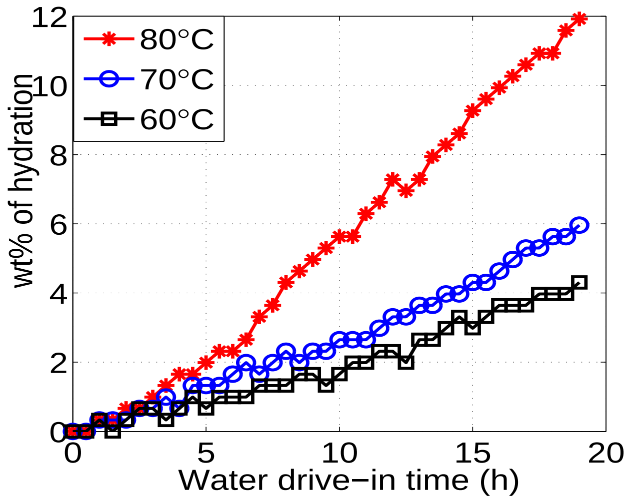

Figure 4.2: Water drive-in process for parylene-encapsulated IPMCs with 25 μm parylene coating (water bath of 60 °C, 70 °C and 80 °C).

properties, control of hydration level and its impact on sensing performance, anti-corrosion effect, and sensing consistency in different media. All the experiments were done with the comparison between the coated and the naked samples, which had the same dimensions (25 mm by 3 mm by 270 μm and were cut from the same big piece of IPMC (50 mm by 50 mm by 270 μm), so that the differences of original properties for each sample were minimized.

4.2 Characterization of Physical Properties

4.2.1 Surface Morphology

Scanning electron microscopy (SEM) images of surface morphology were taken to directly investigate the deposition results for different thicknesses of parylene (Fig. 4.3). Parylene was deposited on the surface of the IPMC samples and these images in Fig. 4.3 show the roughness of the coated parylene surface. Since parylene is transparent, a thin layer (around 2 nm) of gold has been sputtered onto the surface of the parylene layer to better capture the SEM images. Note that the globules observed in Fig. 4.3(b) are most likely the gold particles. From these SEM pictures, one can see that the surface of the sample with thick parylene coating was much smoother than that with thin coating. In particular, pinholes through the encapsulation layer can be observed with 1 μm coating (see Fig. 4.3(a)), indicating that there is significant improvement of the surface condition with thick parylene deposition, which is consistent with the relevant results reported in [73]. When the thickness of the parylene coating increases from 10 μm to 25 μm, there is no significant improvement of the surface condition, as shown in Fig. 4.3(b) and (c). Ideally, the encapsulation layer always has better water barrier capability with thicker deposition, but considering the increasing stiffness of the whole sensor and the cost of thick parylene deposition, a good balance of the encapsulation thickness would be 10-25 μm, which increases the mass of the sample by approximately 1.9-4.8 mg based on the density of the parylene C (1.289 g/cm^3).

4.2.2 Stiffness of the Composite Beam

Compared with a naked IPMC sensor, the most noticeable change of mechanical characteristics for an encapsulated IPMC sensor is the stiffness. Fig. 4.4 shows the schematic and photo of the experimental setup for measuring the stiffness of a beam. The base of the beam was fixed on a frame which could be moved up and down, and the beam tip rested on a load cell used to measure the force. A laser displacement sensor was mounted above the beam measuring the tip displacement. Given the measured force, the corresponding tip displacement and the beam dimensions, we can calculate the stiffness of the composite beam.

IPMC samples with different thicknesses of encapsulation were tested to evaluate the influence of the parylene encapsulation on the stiffness of the sensor beam. The uncoated sample has a nominal dimension of 25 mm by 3 mm by 270 μm, while the coated samples have the nominal dimension plus the thickness of encapsulation. The coated samples were tested without hydration while the uncoated sample was tested in the ambient relative humidity of 40% For each sample, the

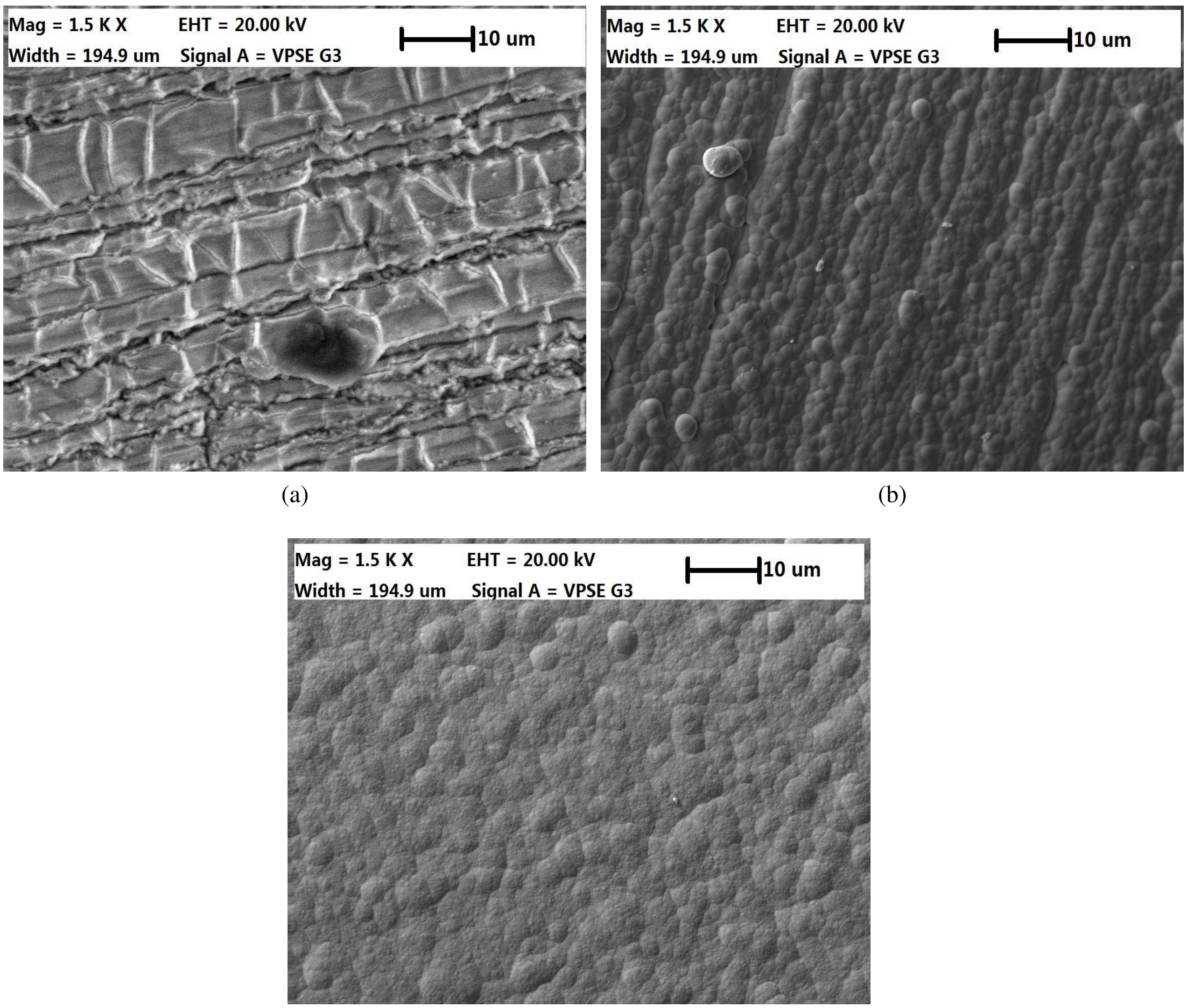

(a) (b)

(c)

Figure 4.3: The SEM images of surface morphology for samples with parylene coating thickness of (a) 1 μm, (b) 10 μm, (c) 25 μm.

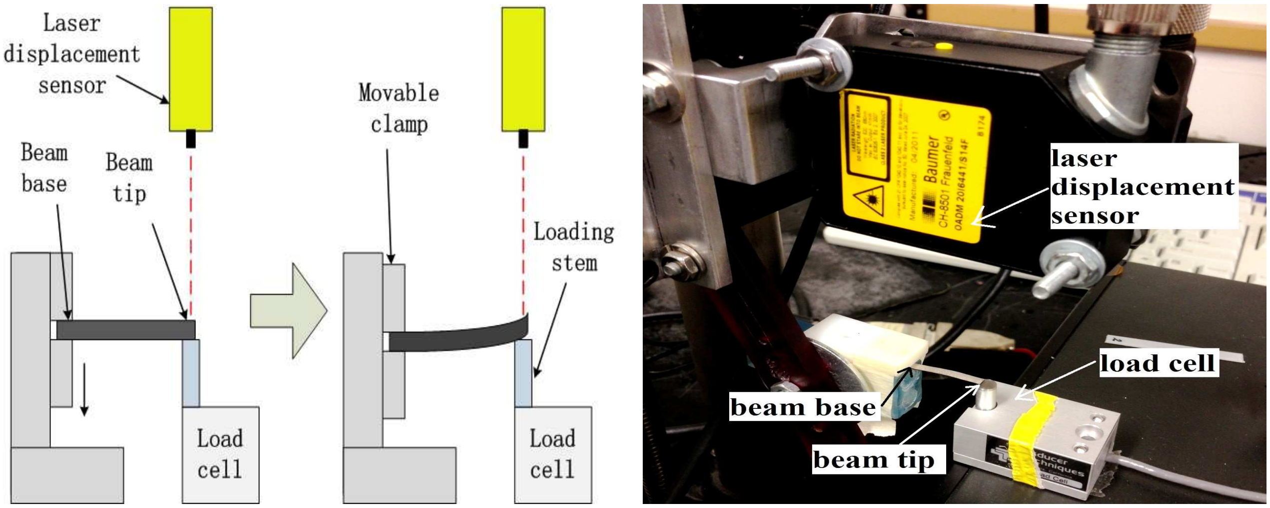

(a) (b)

Figure 4.4: The schematic (a) and photo (b) of the experimental setup for measuring the beam stiffness.

tip bending and the resulting force at 60 positions were collected, and the stiffness was calculated by linear fitting so that the measurement error was minimized, as illustrated in Fig. 4.5. Fig. 4.6 shows the measured stiffness for the IPMC sensors with various thicknesses of parylene coating. It can be seen from Fig. 4.6 that the stiffness of the encapsulated IPMC sensor increases with the thickness of the parylene layer, which is expected considering the constraint of the encapsulant on the beam bending. Unless noted otherwise, we adopted the IPMC sensor with 25 μm encapsulation for the rest of the testing.

4.2.3 Impermeability Characterization

To evaluate the water permeation of the parylene coating layer, a test was first conducted on the evaporation loss of water from the inside of the IPMC sensors under heating. A naked IPMC sample and coated samples with different parylene thicknesses were heated on a hot plate at 60 °C for 60 min. They were weighed every 3 min during the test to measure the water evaporation loss. The test results are shown in Fig. 4.7. The naked sample lost almost all the water after 10 min

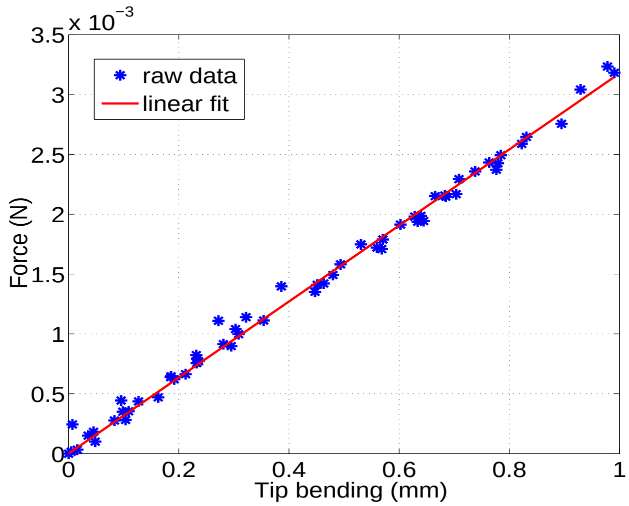

Figure 4.5: Experimental data for the stiffness measurement of a sensor with parylene thickness of 25 μm.

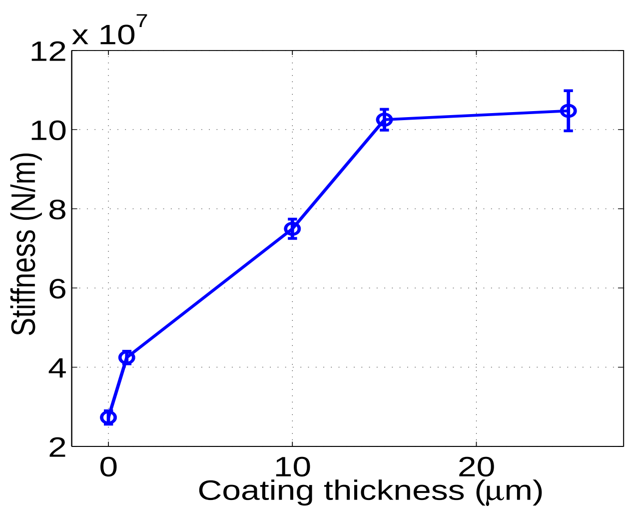

Figure 4.6: Measured stiffness for IPMC sensors with different thicknesses of coating.

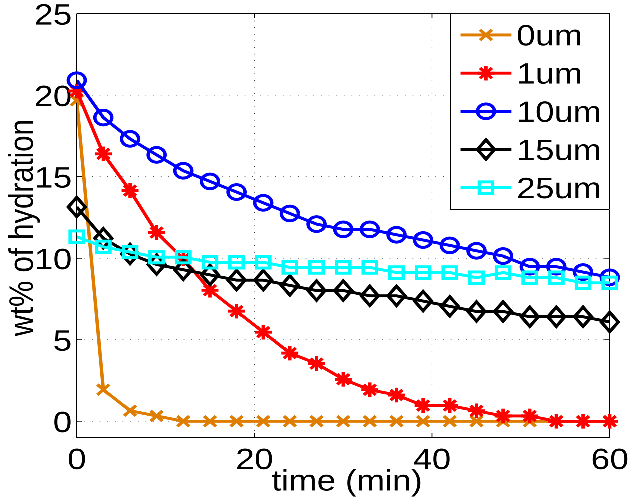

Figure 4.7: Experimental results of water impermeability test under heating.

baking, while the encapsulated ones did not show such a quick water loss. For coated samples with different parylene thicknesses, it can be seen that the water evaporation rate decreases noticeably as the encapsulation layer gets thicker. In particular, the sample with 25 μm coating held its hydration level without significant changes during the one hour baking. Note that the water evaporation through the electrode surface and the parylene layer was greatly accelerated by the heating in this test. When operating under room temperature for most applications, the encapsulated IPMC sensors would have much slower evaporation loss.

Another test was conducted by soaking the parylene-coated IPMC samples in deionized water for up to 10 days to further evaluate the water barrier capability of the proposed encapsulation. The water absorption of IPMC sensors was evaluated by measuring the weight of the samples every 12 h. The sensors were cleaned gently with dry cloth and dried in air for 5 min to eliminate the residual water on the surface. After the weighing process, they were put back into DI water. The experimental results are shown in Fig. 4.8. For the sample encapsulated with 10 μm thick parylene, the WVTR reported by Menon *et al.* [69] can be used to estimate the water permeation rate, since they measured WVTR on a film of 8 μm thickness. During the 10-day test, the 10 μm sample had

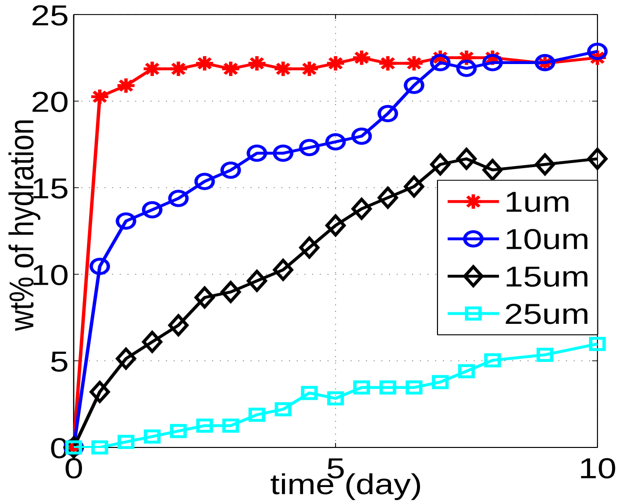

Figure 4.8: Experimental results of impermeability test under soaking in water.

water absorption of 7 mg and an average water permeation rate of 0.7 mg/day. Compared with the estimated water permeation rate of 0.3338 mg in Tab. 4.2, the measured higher water absorption is reasonable since the estimation was based on 90% RH. Also parylene deposition was conducted under different conditions in [69] in terms of the deposition pressure and rate, which would affect the properties of the parylene layer. For the samples with different parylene thicknesses, the test results in Fig. 4.8 show that the water permeation rate drops consistently with an increasing coating thickness, and this rate under 25 μm coating is significantly lower than that under 15 μm coating.

4.3 Control of IPMC Hydration Level and Its Impact on Sensing Performance

It has been discussed in [48] that an IPMC actuator requires particular content of water to operate effectively. For IPMC sensors, it is observed in [39] that while the signal amplitude of the sensor increased with the ambient humidity level, the sensor noise increased as well. Therefore, it is of interest to investigate the impact of hydration level on IPMC sensing performance. In the following experiments, both an uncoated IPMC sensor and an encapsulated one were tested in ambient air under 20 °C and 60% RH. The sensors were tested with different levels of hydration. The uncoated sample was first soaked in deionized water to get saturated hydration and then exposed in air for different amounts of time to obtain different water contents. Testing time was much shorter than the exposure time, so the sample's hydration level stayed nearly constant under each test. For example, in one test the uncoated sample was exposed in air for 5 min after saturation; then it was clamped on the mini-shaker for base-excitation. The sensor output became stable after several seconds and was then collected for 5 sec. Immediately after the testing, the sample was weighed to measure the water content. For the uncoated sample, 0 wt% water content was obtained by heating it on hotplate at 60 °C for 20 min (see Fig. 4.7). For the encapsulated IPMC sample, different levels of hydration were achieved by controlling the soaking time in the water bath during the water drive-in process, as described in Section 4.1.3, and the hydration level of encapsulated sample before the water drive-in process was assumed to 0 wt% because the water molecules inside the IPMC would evaporate completely during the parylene deposition process.

The sensing outputs of both uncoated and encapsulated IPMC sensors under base-excitation were collected with the same experimental setup, as shown in Fig. 4.9. The IPMC samples were excited at their clamping ends by a mini-shaker (Type 4810, Brüel & Kjær) with a frequency of 10 Hz and a base-excitation amplitude of 1 mm. The short-circuit sensing current was conditioned through an amplifying circuit and collected by a dSPACE data acquisition system (RTI 1104, dSPACE). The amplitudes of the IPMC sensor outputs at 10 Hz were extracted as the signals through fast Fourier transform. The noise levels were obtained by calculating the root mean square (RMS) of the amplitudes at other frequencies. The signal-to-noise ratio (SNR) was computed for each case to evaluate the sensor performance at different hydration levels.

The experiment results are shown in Fig. 4.10 and Fig. 4.11. For the uncoated IPMC sample,

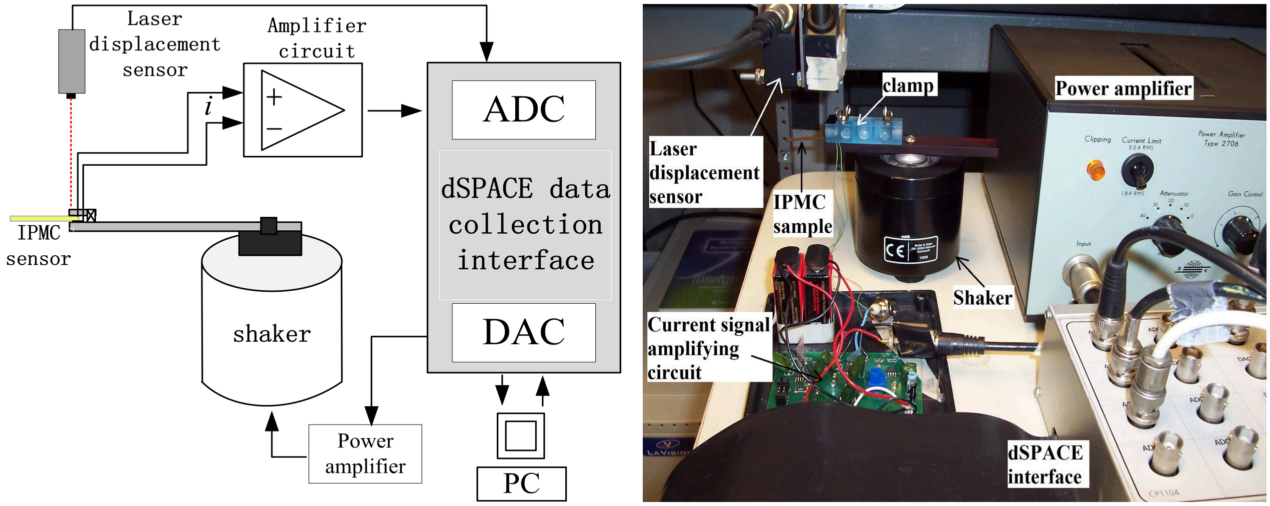

(a) (b)

Figure 4.9: The schematic (a) and photo (b) of the base-excitation experimental setup for characterizing IPMC sensing performance.

under the condition of 0 wt% water content, it failed to generate any noticeable signal as expected. When the water content went up, both the signal and the noise showed an increasing trend initially, but the SNR of the sensor did not show the same trend. Beyond 3.5 wt% water content, both the signal and the noise started to drop as the water content kept increasing. When the water content was higher than 8 wt%, it was difficult to collect accurate sensor outputs experimentally since the water evaporated too fast. Note that this experiment was conducted under the relative humidity of 60%; it is conceivable that the sensor outputs will be different under other relative humidities, given the fact that the sensing properties of a naked IPMC are affected by the ambient humidity level [40]. However, we expect the general trend observed in Fig. 4.10 to hold for other humidity levels.

The performance of the parylene-encapsulated IPMC sensor at different hydration levels is shown in Fig. 4.11. Unlike the case for the naked IPMC sensor, the impact of water evaporation and the ambient humidity level could be ignored for the coated sample due to the parylene encapsulation, thus a larger range of water content had been tested. Compared with the performance of the naked IPMC sensor in Fig. 4.10, the coated sensor had similar patterns for both the signal and the noise amplitudes when the water content went up, while the SNR was slightly more consistent. In both Fig. 4.10 and Fig. 4.11, peak points can be found for the amplitude of the signal. At the peak point, it is believed that the excitation frequency matched the sensor resonance frequency, which varies with the change of IPMC beam mass at different hydration levels. Therefore, adjustment of the resonance frequency can be done for the parylene-encapsulated IPMC sensors to achieve larger sensing outputs in different applications, while it is not feasible for the naked IPMC sensors. Note that the peak point in Fig. 4.11 (around 8 wt%) is different from that in Fig. 4.10 (around 3.5 wt%), and at each peak point, the signal amplitude of the coated sample is twice larger than that of the naked sample. This difference between the naked sample and the coated sample is attributed to their respective mechanical properties which are different due to the added mass and constraint of the parylene layer.

4.4 Evaluation of Anti-corrosion Effect

For a typical IPMC sensor, conductive wires need to be connected to the surface metal electrodes in some appropriate ways to form the contact points for practical applications. The latter can be done through soldering, clamping, taping, or pasting with conductive ink. In any case the contact between different metals leads to nonnegligible galvanic corrosion effect on the more active metal when the IPMC sensor is working in a solution, as shown in the Fig. 4.12 for the soldering case. The corrosion effect can result in an increment of the contact resistance between the surface electrode and the wire, which will reduce the sensing output of the IPMC sensor and result in inconsistent sensing behavior. If the corrosion process lasts too long, the sensor will eventually fail to function due to the large contact resistance.

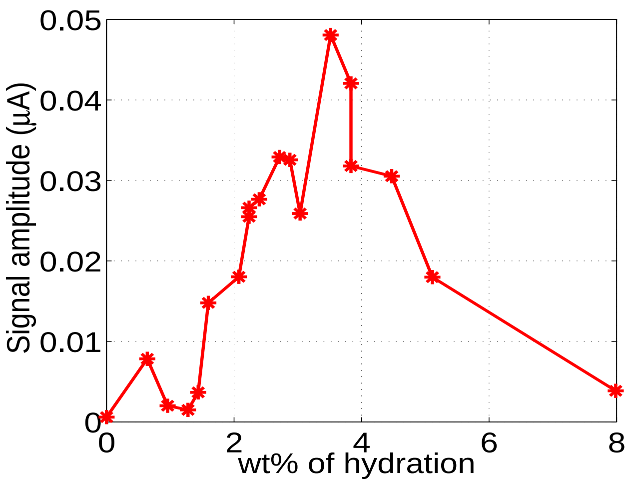

(a)

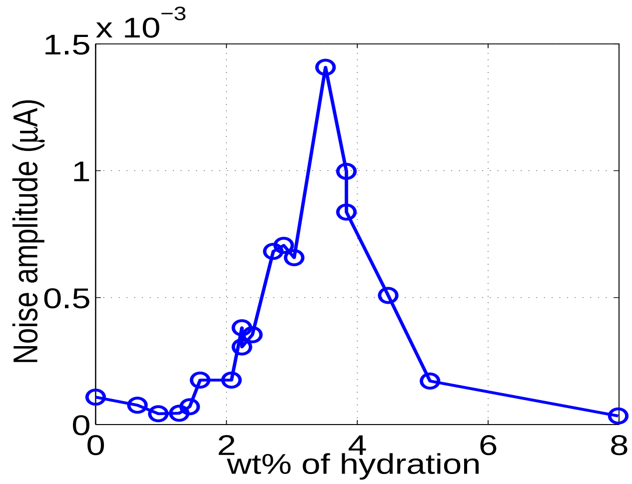

(b)

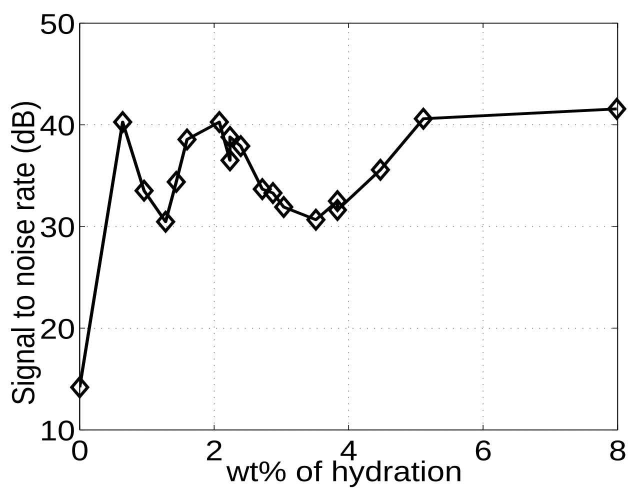

(c)

Figure 4.10: Performance of the uncoated IPMC sensor at different hydration levels: (a) signal magnitude (b) noise magnitude (c) signal-to-noise ratio.

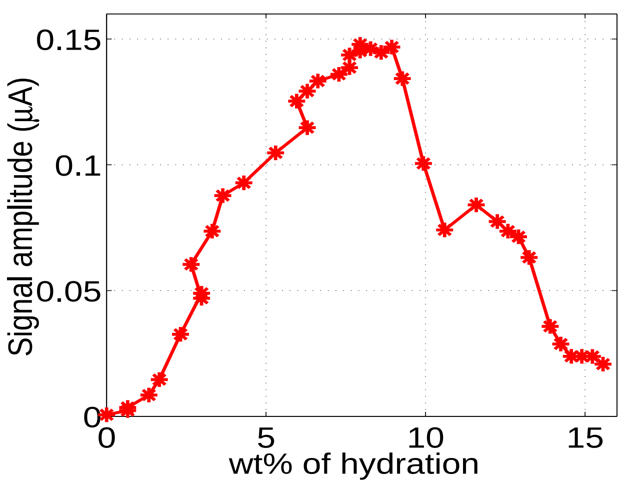

(a)

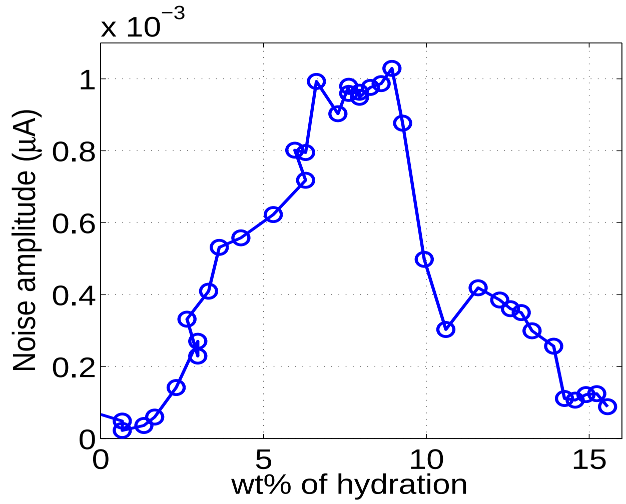

(b)

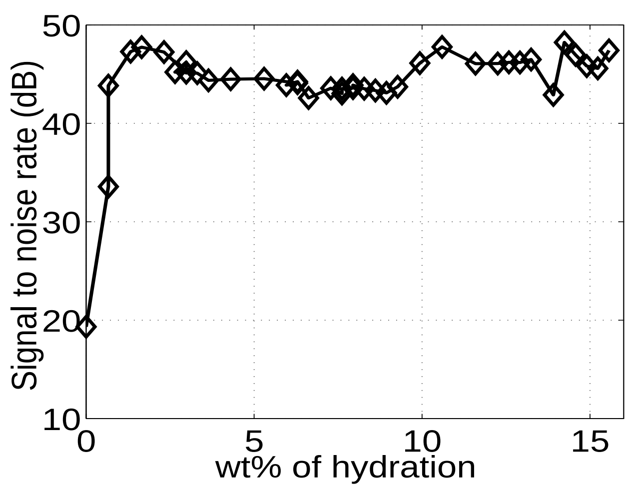

(c)

Figure 4.11: Performance of the coated IPMC sensor at different hydration levels: (a) signal magnitude (b) noise magnitude (c) signal-to-noise ratio.

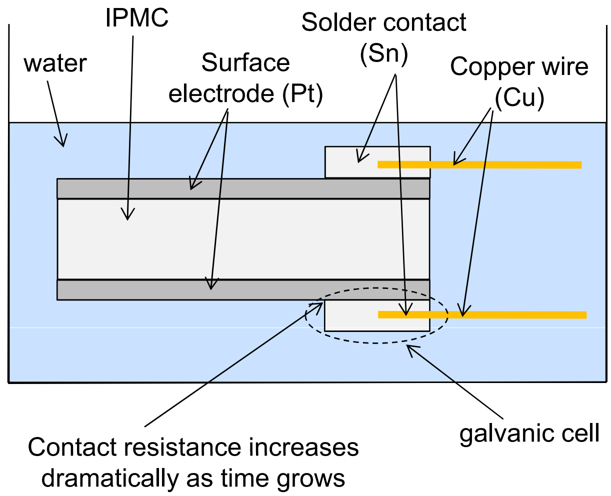

Figure 4.12: Illustration of galvanic corrosion for a soldered IPMC sensor.

In this study, the parylene-encapsulated IPMC sensor was evaluated in terms of its anti-corrosion performance, and compared with some other approaches used to form the contact points. Specifically, the following schemes were compared:

- Solder: copper wires were soldered with tin to the platinum electrodes; the galvanic corrosion would mainly occur between platinum and solder tin;

- Silver conductive epoxy (MG chemicals): copper wires were pasted to the electrodes by the silver epoxy; the corrosion would mainly occur between platinum and silver;

- Solder and epoxy sealing: copper wires were first soldered to the electrodes, and then the whole end of sensor where the soldering tin existed were covered with epoxy, leaving the rest of the sensor naked; the corrosion would occur between platinum and solder tin;

- Parylene encapsulation: the copper wires were first soldered to the electrodes and the whole sensor was encapsulated with thick parylene. The corrosion, if any, would take place between platinum and soldering tin. This is the proposed method.

All of the four samples were soaked in tap water for four days, and their contact resistances between the wires and the electrodes were measured for comparison. The measurement was conducted in air immediately after the sensor was taken out of water and wiped dry. The experimental results are shown in Fig. 4.13. Note that the first point for each case was measured under dry condition and the second point was measured five minutes after soaking the samples in the tap water. The immediate increase of contact resistance at the second point is believed to be the result of the surface electrode expansion when the IPMC samples went into the tap water from the dry condition. For the parylene coated sample, there were only two points available: one was at the beginning of the experiment and the other in the end, because it was not feasible to directly measure the contact resistance during the experiment, given that the whole sample was encapsulated with parylene. One can see from the figure that the contact resistances of the three naked samples kept increasing as the soaking time went up, while the encapsulated sample did not show any noticeable change after four days of soaking in tap water. The sample with soldered wires and no epoxy sealing had the worst performance, due to the fact that its contact points were completely exposed to the water. The silver conductive epoxy was much better than the bare soldering mainly because silver is more stable than tin. When the soldered sample was covered with epoxy around the soldering portion, the contact points were protected by the cured epoxy from the direct water penetration, which significantly lowered the rate of electrochemical reaction between the soldering tin and the platinum electrodes. However, the epoxy sealing could not completely block the water attack, since water will still reach the soldering portion through the IPMC itself, given that the polymer is highly permeable to water. From Fig. 4.13, with parylene encapsulation, the IPMC was isolated from the ambient medium almost completely, thus preventing the galvanic corrosion on the contact points.

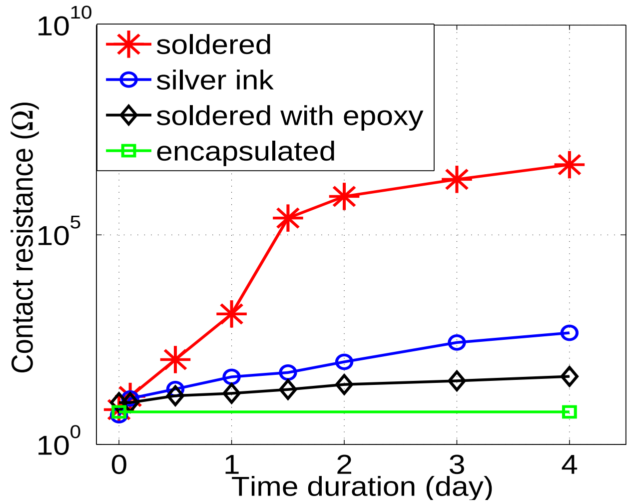

Figure 4.13: Experimental results of contact point corrosion in tap water.

4.5 Evaluation of Sensing Consistency in Different Ambient Environments

As mentioned in previous sections, IPMC sensors could operate with different levels of water content and in different environments. But it is highly desirable for practical applications that IPMC sensors have consistent sensing properties; otherwise, when the ambient environment changes, the sensors either need to be calibrated every time or even fail to work. In this section we present the evaluation results on the consistency of encapsulated IPMC sensing behavior obtained from two sets of experiments. In the first set of experiments, the sensor was placed in a humidity chamber and its sensing output was obtained under different humidity levels. In the second set of experiments, the sensor was first exposed to a series of different media and its sensing output was then obtained in a base-excitation mode in the same humidity chamber. In all experiments the comparison between an encapsulated sensor and a naked sensor was conducted. For the encapsulated sensor, the hydration level was set to be 8 wt

4.5.1 Sensing Consistency Test under Different Humidity Levels

To evaluate the consistency of sensing behavior in air, one naked IPMC sample and one encapsulated sample were tested experimentally under different humidity levels. Fig. 4.14 (a) and (b) show the schematic and the picture of the experimental setup, respectively, including a custom-built humidity chamber made of acrylic panels. Inside the chamber, a humidity sensor (HIH-4030, Honeywell) was used to measure the relative humidity (RH) level, which was then acquired by the dSPACE data acquisition system (RTI 1104, dSPACE). A temperature sensor is also used for monitoring purpose [63]. A control signal would then be sent to the feedback control circuit inside the chamber, to turn on/off the humidifier (EMS-200, Stadler Form) or the dehumidifier (EDV1100, Eva-Dry) accordingly to achieve a given RH value. Limited by the capability of the dehumidifier and the sealing constraints, this humidity chamber could only achieve 40% or higher. Both the naked IPMC sample and the encapsulated one were clamped at the base on a rigid bar which penetrated the chamber wall and was connected to the output shaft of a mini-shaker (Type 4810, Brüel & Kjær) so that both samples received the same mechanical excitation. Outside the humidity chamber, the shaker generated vibration stimulus (up and down) with a frequency of 10 Hz and some fixed amplitude. A 3D-printed flexible shaft cover allows the rigid bar to vibrate freely while maintaining good sealing at the humidity chamber wall. In order to monitor the mechanical motion of the two samples, two laser displacement sensors (OADM 20I6441/S14F, Baumer Electric) were mounted above to measure the tip displacement of each sensor separately. The mounting frame for the laser sensors was isolated from the table where the mini-shaker was mounted. A two-tier two-channel amplification circuit was used to measure the short-circuit current generated by the IPMC samples. All the signals were collected half an hour after the RH level became stable at the preset value, so that the naked IPMC sensor got sufficient time to reach the water vapor trans-

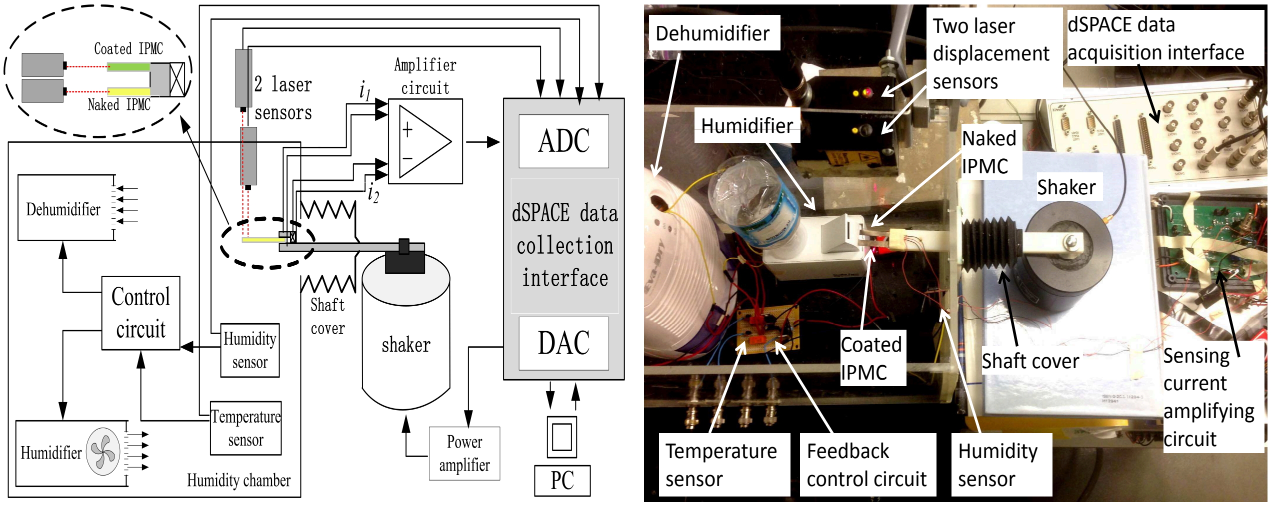

(a) (b)

Figure 4.14: The schematic (a) and photo (b) of the experimental setup for evaluating IPMC sensor performance in a custom-built humidity chamber.

mission balance with the ambient humidity. The weights of two samples are not measured during the test since it is infeasible to weigh the sensors within the humidity chamber. Control signal generation, sensing data acquisition, and processing were all performed through the dSPACE system. Fast Fourier transform was used to extract the amplitudes of the IPMC sensor outputs and the tip displacements at 10 Hz, which were used to evaluate the sensor performances under different humidity levels.

The experimental results for the sensing currents of each IPMC sample under different humidity levels are shown in Fig. 4.15. For the convenience of comparison, all the data points were normalized with respect to the sensing current amplitude of the encapsulated IPMC sample under 42% RH. First of all, the sensing current amplitude of the encapsulated IPMC sensor was larger than that of the naked one during the full range of the tested humidity levels. This was because the water contained in the coated IPMC sample was more than that absorbed by the naked sample from the ambient environment, even under almost 100% RH. For the uncoated sample, one can also see that there was no peak for the sensing current amplitude as the ambient RH rose up to

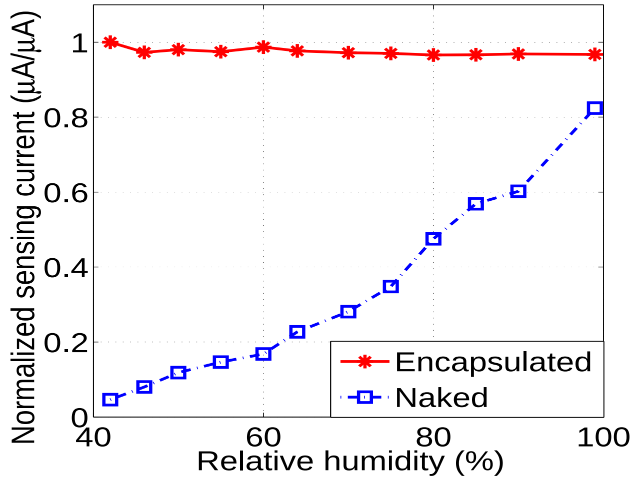

Figure 4.15: Sensing responses of IPMC sensors under different humidity levels.

almost 100%. In view of the result in Fig. 4.10 (a), the latter indicates that the water content in the naked IPMC sensor, even under almost 100% RH, had not reached the optimal hydration level observed in Fig. 4.10 (a).

From Fig. 4.15, one can see that the sensing current of the uncoated sensor varied significantly as the environmental humidity changes, while the encapsulated sensor maintained excellent sensing consistency. The experimental results for the tip placements of each IPMC sample under different humidity levels are shown in Fig. 4.16. Similarly, the results were normalized with respect to the initial point under 42% RH for the encapsulated IPMC sample. It can be seen that the tip displacement of the naked IPMC sample kept going up as the ambient RH increased, while the coated sample maintained a stable mechanical property.

4.5.2 Sensing Consistency Test Following Exposure to Liquid Media with Different Cations

For a naked IPMC sensor working in a liquid medium, it is expected that the sensing properties will be affected by both the solute and the solvent in the ambient fluid. For example, if the solution

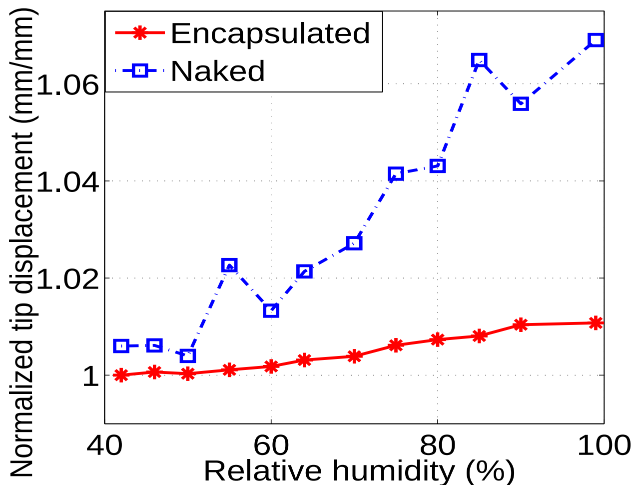

Figure 4.16: Tip displacements of IPMC sensors under different humidity levels.

where the IPMC sensor operates contains sufficient amount of other cations which are different from the cations within the IPMC (typically Li^+), those cations tend to exchange with each other given the intrinsic ion-exchange property of Nafion. With different cations, IPMCs have different performances in both actuation and sensing, as discussed in [41, 42]. Therefore, it is desirable to protect the IPMC sensor from the outside media.

To evaluate the sensing consistency of the IPMC sensors in the solutions, one naked IPMC sample and one parylene-coated sample were immersed in solutions with different cations, including Li^+, Na^+, K^+, Ca^{2+}, Mg^{2+}, H^+. The concentrations of those solutions were all 1 mol/L and the anions were all chloride. The naked and coated IPMC samples were first soaked in one solution together for 12 hours; then they were taken out, dried and put one by one into the same experimental setup with humidity chamber shown in Fig. 4.14. The mini-shaker provided 10 Hz excitation on the base, and the circuit and the laser sensor collected the sensing currents and the tip displacements of the IPMC samples, respectively. To make sure the consistency of the testing conditions, the base-vibration had fixed amplitude and the humidity level inside the humidity chamber was always set to 40% RH. After the testing in the humidity chamber, the same naked and coated samples were soaked in another solution together for 12 hours. Considering the metal corrosion problem mentioned in Section 4.4, the naked IPMC sample was submerged in the solutions without wires soldered on its electrodes; it was clamped with wires attached onto the surface electrodes when tested in the humidity chamber.

The experimental results for the sensing current amplitude of the naked IPMC sample after its soaking in different solutions is shown in Fig. 4.17. On the x-axis, the label order from left to right is the same order of the solutions that the naked IPMC sample was soaked in. All the data points were normalized with respect to the first point on the left for the case of Li^+. It should be noticed that the naked sample had been soaked in each solution with different cations and tested in humidity chamber for twice. The reason for repeating the experiments is to accommodate the influence of the soaking order, since all the experiments were done on the same IPMC sample. From the figure one can see that the naked IPMC sensor showed strong dependence on the cations, indicating that there was significant exchange of ions with the ambient fluid within the 12-hour soaking. Unlike the case for the IPMC actuation where Li^+ shows the best performance in terms of force generation [41], in this experiment H^+ has shown much better sensitivity than other cations tested (in terms of the sensing current amplitude), which echoes the results reported in [42] to some degree. Note that the sensing currents for all the other cations (except H^+) have increased greatly following the second round of soaking. This is believed to be caused by that some residual H^+ ions staying in the IPMC sample after it was soaked in H^+ solution for the first time, which contributed to the increased sensing output during the repeated experiments for other ions.

Fig. 4.18 shows the experimental results for the sensing current of the coated IPMC sample. Similarly, the results were normalized with respect to the first point on the left for the case of Li^+. It can be seen that the encapsulated IPMC sensor maintained excellent sensing consistency after being soaked in solutions with different cations, indicating that the parylene encapsulation

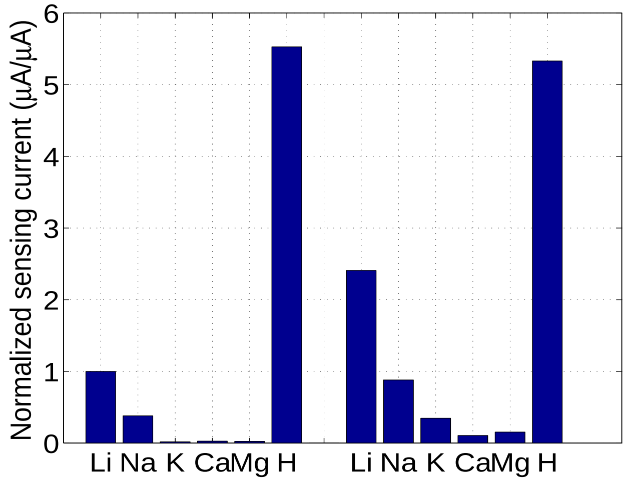

Figure 4.17: Sensing current of naked IPMC sensor in solutions with different cations.

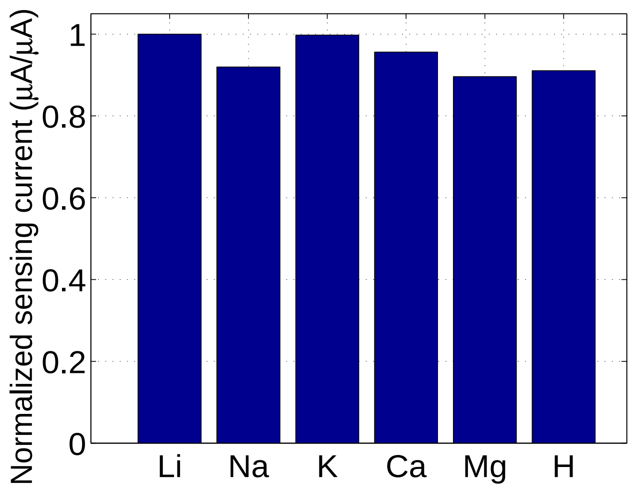

Figure 4.18: Sensing current of coated IPMC sensor in solutions with different cations.

effectively prevented ion exchange with the ambient media. Unlike the case for the uncoated IPMC sample in Fig. 4.17, the coated sample had only been soaked in each solution for once, since it was already enough to draw a solid conclusion based on the experimental results shown in Fig. 4.18. The tip displacements of the naked IPMC sample and the coated one were also collected during the experiments, which did not show any noticeable dependence on the types of the cations, suggesting that the cations have much more influence on the electromechanical properties of IPMC rather than the pure mechanical properties.

Table 4.3: Uncoated IPMC expansion in organic solvent.

Naked IPMC sensor	Length (mm)	Width (mm)	Thickness (μm)	Volume (mm^3)
before ethanol	25	3	270	20.25
after ethanol	32.8	4.5	460	67.90
before gasoline	25	3	270	20.25
after gasoline	26.8	3.6	300	28.93

4.5.3 Sensing Consistency Test Following Exposure to Organic Solvent

IPMC sensors also have potential applications in some organic fluid media, such as detecting the gasoline flow in automotive engines [74], where the sensor properties could be influenced by the ambient organic solvent. Therefore, similar experiments have been conducted to evaluate the sensing performance of the IPMC sensors in organic fluid media. Both the naked IPMC sensors and the parylene-coated sensor were soaked in ethanol and gasoline under room temperature for 12 hours, respectively; then they were taken out and tested immediately in the same humidity chamber mentioned above. Note that ethanol is highly soluble to water while gasoline is not. Two naked IPMC samples were tested in ethanol and gasoline separately, while the same coated IPMC sample was used in ethanol and gasoline. The experimental results first showed that the naked IPMC sample expanded significantly in volume after being soaked in these two organic solvents, as shown in Tab. 4.3. Especially in ethanol, the expanded volume was more than twice larger, which was mainly due to the high water-solubility of ethanol. However, the parylene-coated IPMC sample did not show any noticeable change in volume after soaked in both of these solvents, indicating the excellent impermeability of the parylene layer.

The experimental results for the sensing currents and tip displacements of the tested sensors are shown in Fig. 4.19 and Fig. 4.20. All the data points were normalized with respect to the corresponding initial states. Note that in Fig. 4.19 (b) the tip displacement for the naked IPMC sample increased a little bit after the gasoline soaking, since the sample expanded by 28% in size and still held sufficient stiffness; for the ethanol soaking, the naked sample became so soft that it could not hold the shape of a cantilever beam and the tip dropped down, so the laser sensor could not detect the displacement of the beam tip, and it had no tip displacement in Fig. 4.19 (b). For the naked IPMC sensors, the sensing outputs had greatly dropped after they were submerged in ethanol and gasoline for sufficient time. It is believed that for the case of ethanol, the water contained in the IPMC sensor had mixed quickly with ambient ethanol given that they are mutually soluble, and for the solvent of gasoline, the water diffused gradually. Therefore, it can be seen that there exists one essential problem for the naked IPMC sensor working in organic fluid media, which is the significantly reduced sensor outputs, in other words, very weak sensitivity. Even if the organic media is insoluble to water (for example, the gasoline), the water contained in the IPMC sensor will not stay long to generate consistent output, but diffuse or be washed away gradually into the ambient media, resulting in the continuous loss of sensitivity and thus the sensing inconsistency. However, as indicated by Fig. 4.20, the parylene-encapsulated IPMC sensor did not show any clear sign of such problems; in particular, the coated IPMC sample had maintained very good mechanical property and sensing consistency after being soaked in both ethanol and gasoline for 12 hours.

All in all, with comparison to the naked IPMC sensor, these experiments have demonstrated that the parylene-encapsulation does not only improve the sensing consistency of the IPMC sensor in different ionic solutions, it also extends its potential application to other organic fluid media by protecting the IPMC from geometric expansion, mechanical change and water loss caused by the solvent pollution.

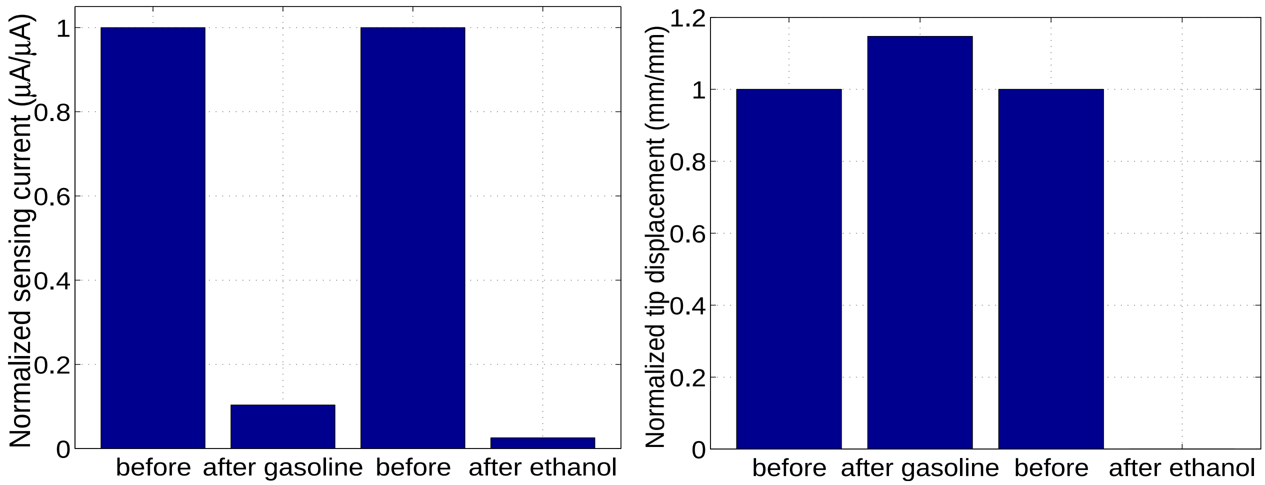

(a) (b)

Figure 4.19: Performance of the uncoated IPMC sensor after soaking in organic solvent: (a) sensing current (b) tip displacement.

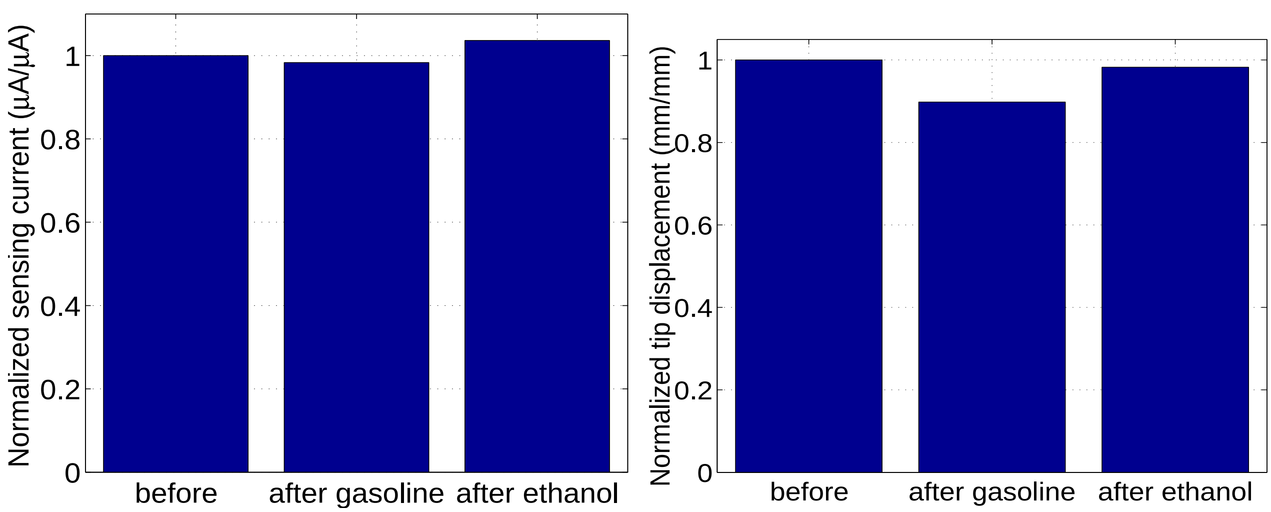

(a) (b)

Figure 4.20: Performance of the coated IPMC sensor after soaking in organic solvent: (a) sensing current (b) tip displacement.

Chapter 5

Fabrication and Modeling of Novel IPMC Sensors of Omnidirectional Sensing Capabilities

We have proposed in this chapter two types of novel IPMC sensors capable of omnidirectional sensing. The first one is fabricated based on the casting and solidification of Nafion solution. The sensor takes the form of a square column and is capable of omnidirectional sensing. We have characterized the sensor behavior in air with a base-excitation setup and discussed the correlation between the two sensing outputs. We have further modeled its flow sensing capability in water with an empirical model, which takes the *x*-direction component and *y*-direction component of the flow velocity as inputs and the two sensing currents as outputs. Experimental results have confirmed that the identified model is effective.

In order to investigate the coupling issue found in the square column IPMC sensor, a novel tubular thin-wall IPMC sensor is fabricated based on Nafion tubing. It has one common inner electrode and four outer electrodes, which form four routes of common-ground sensor outputs. With a custom-designed experimental setup, we further characterize the sensor response (sensing current) to tip deflection in different directions. The setup provides dynamic tip bending with adjustable orientations and controlled bending amplitude and frequency (1 to 20 Hz). As the orientation angle varies, it is observed that antagonistic routes generally have similar periodic properties with opposite signal polarities, while neighboring routes show a shift of response by approximately 90°. Based on the characterization results, we propose a physical dynamic model for the tubular IPMC sensor, by treating each infinitesimal slice (along the tube axis) of the tube as a beam-shaped IPMC sensor and performing integration around the tube. A governing partial differential equation (PDE) first introduced in [7] is used to describe the charge dynamics within IPMC, where the effect of contact resistance is captured. The model, which takes the form of an infinite-dimensional transfer function, is further reduced to a finite-dimension model, based on which a scheme is developed for computing the tip deflection stimulus given the sensor outputs. Experiments have been conducted to validate the proposed model and the stimulus-reconstruction scheme.

5.1 Square Column IPMC Sensor

5.1.1 Fabrication

An IPMC sensor is typically fabricated by chemically depositing a platinum layer as the electrode on both surfaces of a commercially available Nafion film (Dupont), which is usually no more than 10 mil (254 μm) in thickness. The proposed novel IPMC sensor in this study is fabricated in-house based on the Nafion solution (Nafion Dispersion D2021, Ion Power, Inc.). As illustrated in Fig. 5.1, our process flow starts with the refinement of the Nafion solution, which is then cast in a mold layer by layer and solidified gently by evaporating the solvent on a hotplate at 60°C. The solidified Nafion block, which turns to slightly yellow, needs to be heated at 165°C in a furnace for 90 min to obtain good properties. Re-acidification of the annealed Nafion is carried out using boiling nitric acid (20 wt%) for 60 min followed by the boiling water treatment. The Nafion block

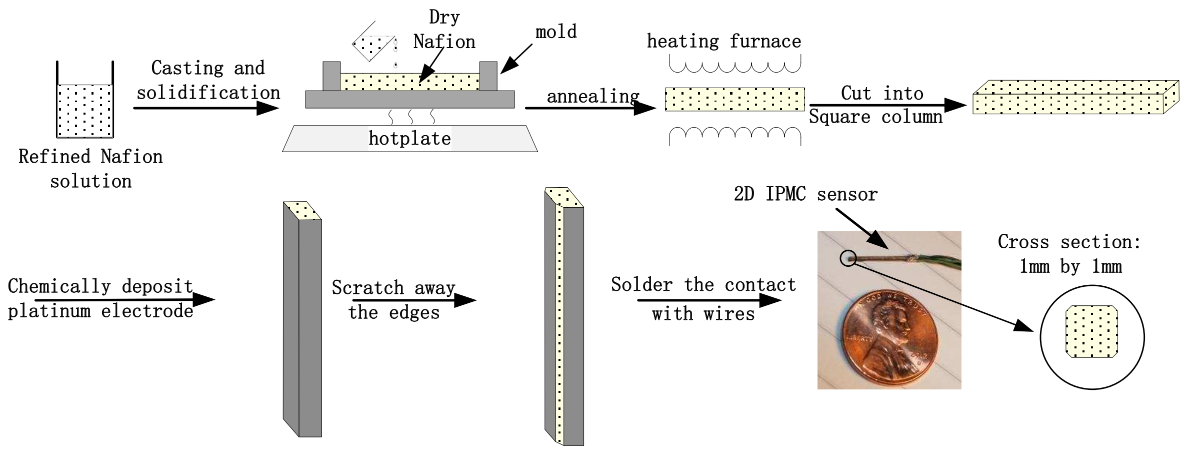

Figure 5.1: Outline of the proposed fabrication process flow for the square column IPMC sensor.

is then cut into suqare columns, each of which has the cross section of 1mm by 1mm and the length of 15mm. The traditional approach to IPMC fabrication is used to deposit platinum electrodes on all four surfaces based on the impregnation-reduction-ion exchange process. The neighboring electrodes are isolated from each other by scratching away the platinum on the four edges along the length direction. Finally, electrical wires are soldered onto the electrodes to form the contacts.

Before casting the Nafion solution, we refine the solution by replacing the solvent in order to avoid the cracking problem [46] and improve the conductivity of the Nafion [75]. The Nafion solution from the vendor contains water and propanol as solvents which need to be replaced by other organic solvents such as Dimethylformamide (DMF) [75]. The solidification process needs to be done very gently, otherwise there will be small bubbles forming inside the solidified Nafion block, and the Nafion solution should be continuously added into the mold due to the large volumetric shrinkage. The annealing process is necessary in order to obtain good chemical stability for cast IPMC, as reported in the literature [76]. Fig. 5.2 shows three potential configurations of sensing output for this square column IPMC sensor. The first configuration gives out three routes of sensing signals, while the other two have two routes of signals each. The third orthogonal configuration

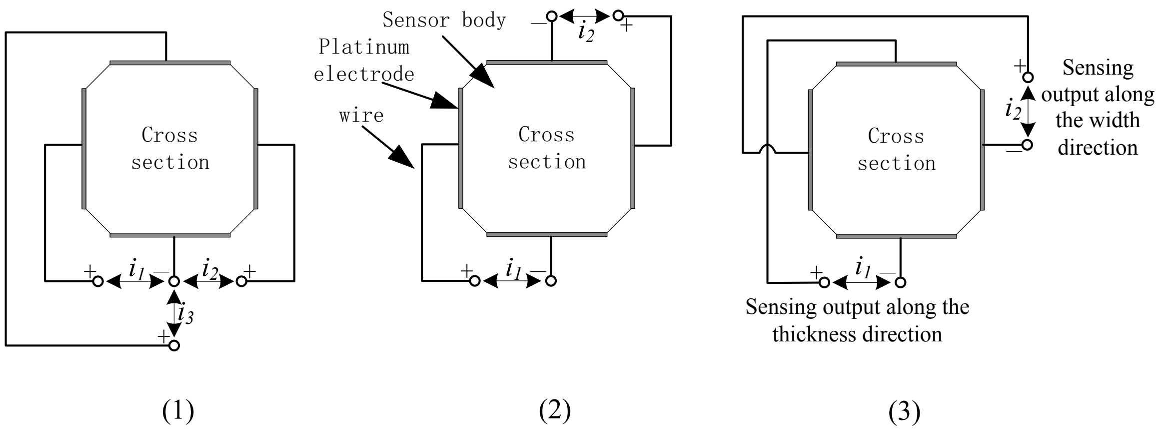

Figure 5.2: Three potential configurations of the sensor ouput.

has been adopted in this paper for the simple reason that it has the most relevance to the configuration of the traditional beam-shape IPMC sensor. Note that in the third configuration of Fig. 5.2, we define the width direction and thickness direction simply for the reference convenience, since the dimensions are the same across either directions, which is 1mm.

5.1.2 Sensor Characterization in Air

The square column sensor is first base-excited in air to study the empirical frequency response and the correlation between the two routes of sensing signals. In this paper, we collect the short-circuit currents of the IPMC sensor as the sensing output. Fig. 5.3 (a) and (b) show the schematic and picture of the experimental setup , providing base excitation for the sensor and allowing the measurement of base displacement and two routes of the sensing current. The sensor is clamped at the base by two rigid bars and the bars are fixed on a mini-shaker (Type 4810, Brüel & Kjær), which generates vibration stimulus (up and down) with some controlled frequency. One laser displacement sensor (OADM 20I6441/S14F, Baumer Electric) is mounted above the sensor base, measuring the base displacement. The mounting frame for the laser sensors is isolated from the table where the mini-shaker is mounted. A two-tier amplification circuit is used to measure the

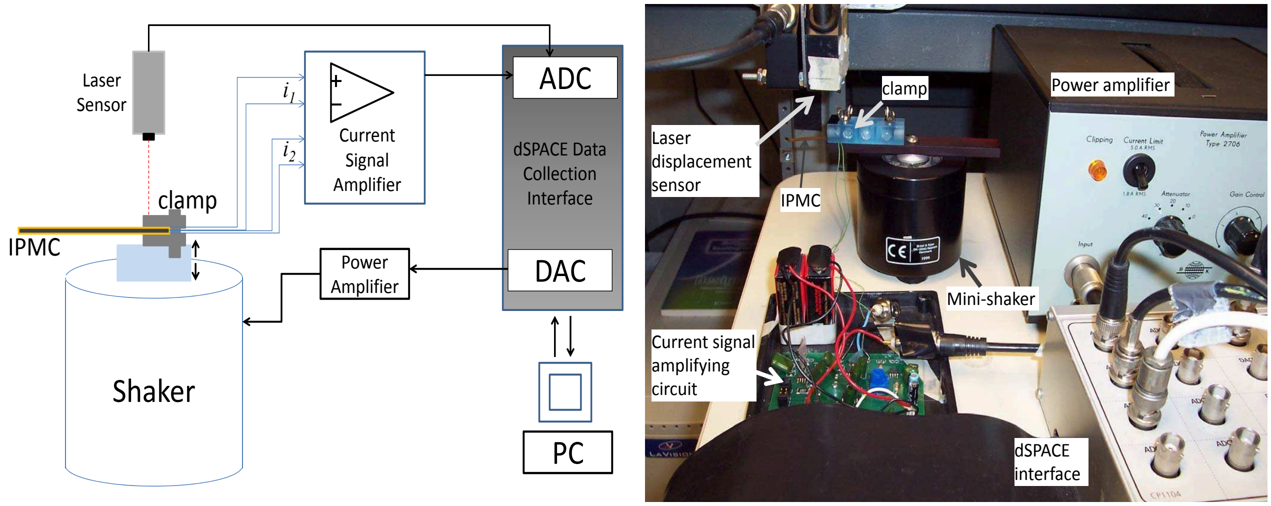

(a) (b)

Figure 5.3: The schematic (a) and photo (b) of the experimental setup for base-excitation in air.

short-circuit current generated by the IPMC. Control signal generation, sensing data acquisition, and processing are performed through a dSPACE system (RTI 1104, dSPACE).

As illustrated in Fig. 5.2, one pair of the sensor electrodes is across the width direction and the other pair is across the thickness direction. The sensor is first clamped in a way that the base vibration generated by the mini-shaker is along the thickness direction. It is then turned by 90° so that the vibration is along the width direction. For each case, the base excitation displacement as the input and two routes of sensing current signals as the output are collected from 10 to 100 Hz. The amplitudes and phases of these signals are extracted through fast Fourier transform to compute the empirical frequency response.

Fig. 5.4 (a) and (b) show the experimental results under base excitation along the thickness and width direction, respectively. First, it can be seen that there is strong correlation between the two sensing signals both in amplitude and phase. In particular, when the sensor is subjected to base excitation along its thickness direction, the sensing output along the width direction, which is expected to be much smaller, is actually comparable to the sensing signal along the thickness direc-

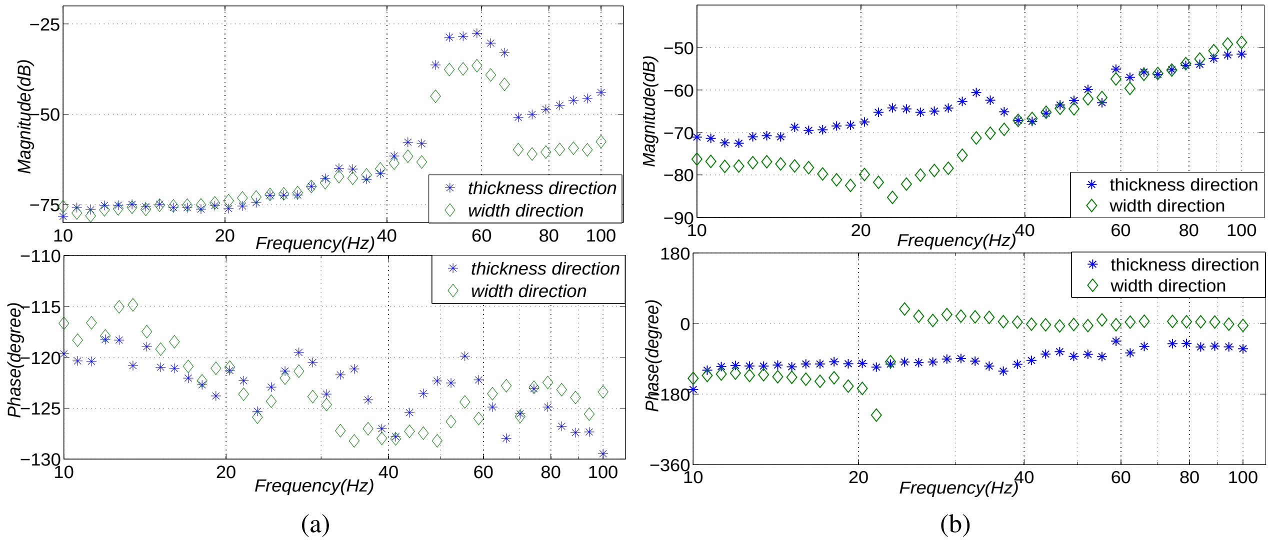

Figure 5.4: The empirical frequency responses of two sensing outputs when the sensor was subjected to base vibration along the thickness direction (a) and the width direction (b). Input: base excitation; output: IPMC short-circuit current.

tion in the low frequency range. This coupling is primarily rooted in the strain distribution inside a Nafion square column, and most likely strengthened by the asymmetric geometric dimensions and inhomogeneous material properties formed during the fabrication process, as evidenced in Fig. 5.4 (b). Compared with the results in Fig. 5.4 (a), the sensing outputs shown in Fig. 4(b) demonstrate significantly different coupling behavior, where the signal along the thickness direction is stronger than that along the width direction in the low frequency range while being comparable in the higher frequency range (above 40 Hz).

5.1.3 Characterization and Modeling in Water

One promising application of the IPMC sensor is to collect flow information in an artificial lateral system [33]. The traditional thin beam-shaped IPMC sensor can only capture the flow information along the thickness direction, while the proposed column-shaped IPMC sensor is potentially capable of two-dimensional flow sensing. Characterization has been done in water and an empirical model relating the sensor outputs to the flow velocity has been computed.

5.1.3.1 Characterization and Modeling Methods

In this study we consider a potential flow generated by a dipole source, which is a vibrating sphere in water. The velocity potential ϕ can be expressed as [77]

$$\phi(\mathbf{r}) = -\frac{a^3(\mathbf{v}_\mathrm{d}\cdot\mathbf{r})}{2\|\mathbf{r}\|^3}, \tag{5.1}$$

where a is the diameter of the vibrating sphere, $\mathbf{r}$ is the relative location of a spatial point of interest with respect to the center of the sphere , $\mathbf{v}_\mathrm{d}$ represents the instantaneous velocity of the dipole source, and $\|\cdot\|$ denotes the Euclidean norm of a vector. The flow velocity $\mathbf{v}(\mathbf{r})$ at a point indicated by $\mathbf{r}$ is

$$\mathbf{v}(\mathbf{r}) = \nabla\phi(\mathbf{r}) = \frac{a^3\left(3(\mathbf{v}_\mathrm{d}\cdot\mathbf{r})\mathbf{r} - \|\mathbf{r}\|^2\mathbf{v}_\mathrm{d}\right)}{2\|\mathbf{r}\|^5}. \tag{5.2}$$

By placing the dipole source under the water surface deep enough, we can limit our discussion to a two-dimensional horizontal plane, denoted as $x-y$ plane. The dipole source is first placed at $(x_{\mathrm{d}1}, y_{\mathrm{d}1})$ and vibrates along the x-direction with velocity v_x^d, as illustrated in Fig. 5.5 (a). For a point of interest (x,y) on the $x-y$ plane, from (5.2) we get

$$v_\mathrm{x}(x,y) = \frac{a^3 v_\mathrm{x}^\mathrm{d}}{2\|\mathbf{r_1}\|^5}\left(2(x-x_{\mathrm{d}1})^2 - (y-y_{\mathrm{d}1})^2\right), \tag{5.3}$$

$$v_\mathrm{y}(x,y) = \frac{a^3 v_\mathrm{x}^\mathrm{d}}{2\|\mathbf{r_1}\|^5} 3(x-x_{\mathrm{d}1})(y-y_{\mathrm{d}1}), \tag{5.4}$$

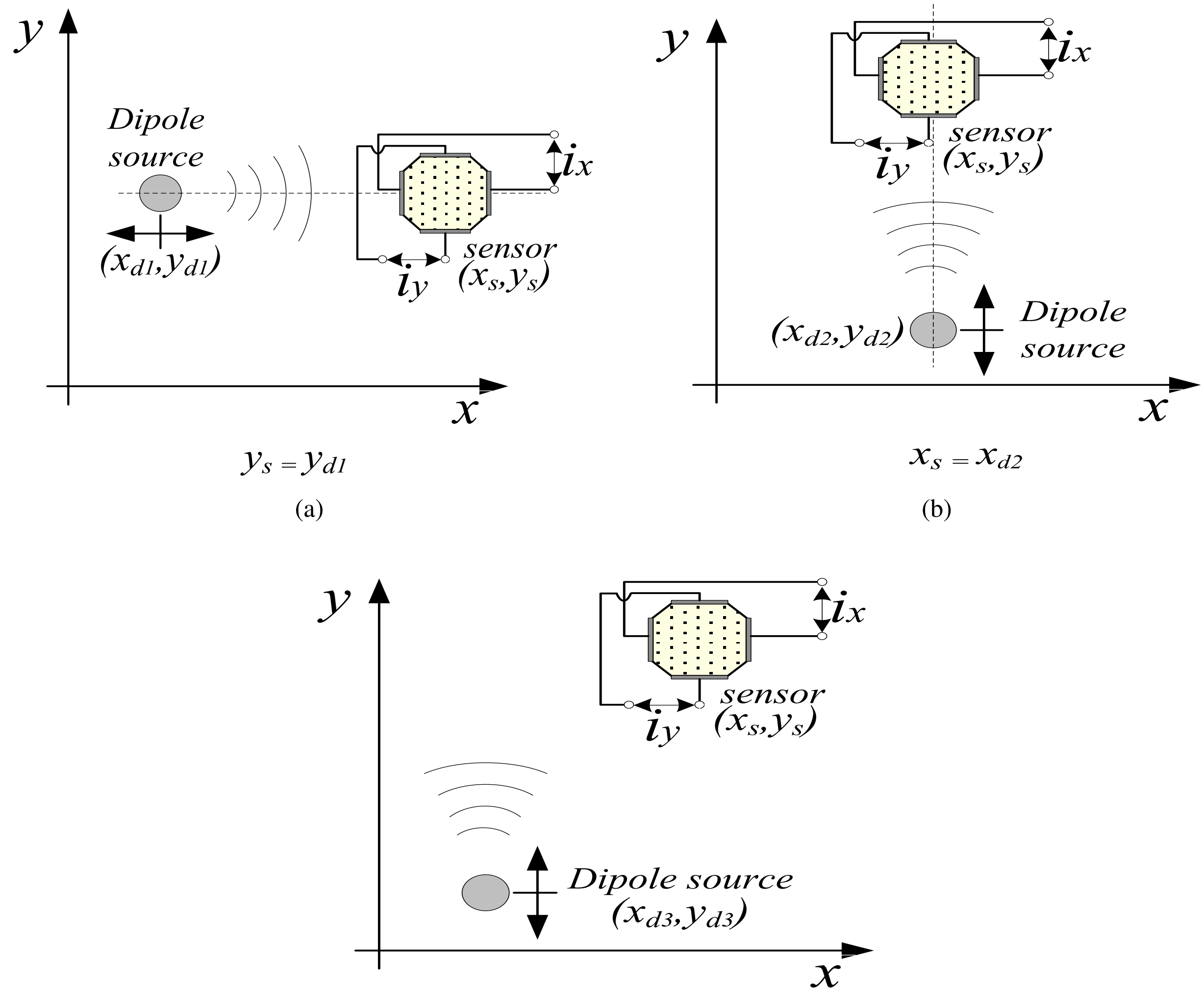

(a) (b) (c)

Figure 5.5: Different locations of dipole source with respect to the square column IPMC sensor.

where $\|\mathbf{r_1}\| = \sqrt{(x - x_{\text{d1}})^2 + (y - y_{\text{d1}})^2}$. The sphere is assumed to vibrate with angular frequency f and amplitude A_{x}:

$$v_{\text{x}}^{\text{d}} = A_{\text{x}} \sin(2\pi f t).$$

The square column IPMC sensor is amounted vertically with its length direction perpendicular to the $x-y$ plane and its tip on the $x-y$ plane, and the thickness direction of the sensor is oriented to the x-direction while the width to the y-direction, as the schematic shows in Fig. 5.5 (a). It is assumed that the flow distribution as characterized in (5.2) is not influenced by the presence of the sensor due to its small dimensions. The sensor is located on the $x-y$ plane at $(x_{\mathrm{s}}, y_{\mathrm{s}})$ with y_{s} equal to y_{d1}, thus we have

$$v_{\mathrm{x}}(x_{\mathrm{s}}, y_{\mathrm{s}}) = \frac{a^3 v_{\mathrm{x}}^{\mathrm{d}}}{2\|\mathbf{r_1}\|^5} 2(x_{\mathrm{s}} - x_{\mathrm{d1}})^2, \tag{5.5}$$

$$v_{\mathrm{y}}(x_{\mathrm{s}}, y_{\mathrm{s}}) = 0, \tag{5.6}$$

where $\|\mathbf{r_1}\|$ is simplified as $(x_{\mathrm{s}} - x_{\mathrm{d1}})$. Taking the flow velocity $v_{\mathrm{x}}(x_{\mathrm{s}}, y_{\mathrm{s}})$ as the input and the two sensing signals, i_{x} (along thickness direction) and i_{y} (along width direction), as the output, we can get the empirical frequency responses for the transfer function of $G_{\mathrm{xx}}(s)$ relating the sensing signal in the x-direction to the flow velocity in the x-direction

$$G_{\mathrm{xx}}(s) = \frac{i_{\mathrm{x}}(s)}{V_{\mathrm{x}}(s)} = \frac{i_{\mathrm{x}}(s)}{v_{\mathrm{x}}^{\mathrm{d}}(s)} \frac{(x_{\mathrm{s}} - x_{\mathrm{d1}})^3}{a^3}, \tag{5.7}$$

and the transfer function of $G_{\mathrm{xy}}(s)$ relating the sensing signal in the y-direction to the flow velocity in the x-direction

$$G_{\mathrm{xy}}(s) = \frac{i_{\mathrm{y}}(s)}{V_{\mathrm{x}}(s)} = \frac{i_{\mathrm{y}}(s)}{v_{\mathrm{x}}^{\mathrm{d}}(s)} \frac{(x_{\mathrm{s}} - x_{\mathrm{d1}})^3}{a^3}, \tag{5.8}$$

where $i_{\mathrm{x}}(s)$, $i_{\mathrm{y}}(s)$, $V_{\mathrm{x}}(s)$ and $v_{\mathrm{x}}^{\mathrm{d}}(s)$ denote the Laplace transform of i_{x}, i_{y}, $v_{\mathrm{x}}(x_{\mathrm{s}}, y_{\mathrm{s}})$ and $v_{\mathrm{x}}^{\mathrm{d}}$, respectively. The sphere vibration $v_{\mathrm{x}}^{\mathrm{d}}$ and two short-circuit current signals of i_{x} and i_{y} are directly measured from the experiments.

The dipole source is then moved to another point at $(x_{\mathrm{d2}}, y_{\mathrm{d2}})$ with x_{d2} equal to x_{s}, where it vibrates only along the y-direction, as illustrated in Fig. 5.5 (b). Similarly, from (5.2), we can get the empirical frequency response for $G_{\mathrm{yx}}(s)$ relating the sensing signal in the x-direction to the flow velocity in the y-direction

$$G_{\mathrm{yx}}(s) = \frac{i_{\mathrm{x}}(s)}{V_{\mathrm{y}}(s)} = \frac{i_{\mathrm{x}}(s)}{v_{\mathrm{y}}^{\mathrm{d}}(s)} \frac{(y_{\mathrm{s}} - y_{\mathrm{d2}})^3}{a^3}, \tag{5.9}$$

and that for the transfer function of $G_{\mathrm{yy}}(s)$ relating the sensing signal in the y-direction to the flow velocity in the y-direction

$$G_{\mathrm{yy}}(s) = \frac{i_{\mathrm{y}}(s)}{V_{\mathrm{y}}(s)} = \frac{i_{\mathrm{y}}(s)}{v_{\mathrm{y}}^{\mathrm{d}}(s)} \frac{(y_{\mathrm{s}} - y_{\mathrm{d2}})^3}{a^3}. \tag{5.10}$$

The empirical frequency responses are then used to identify the transfer functions for $G_{\mathrm{xx}}(s)$, $G_{\mathrm{xy}}(s)$, $G_{\mathrm{yx}}(s)$ and $G_{\mathrm{yy}}(s)$ respectively in the form of rational functions of the Laplace variable s. These four identified transfer functions form an empirical model for the two-dimensional flow sensing of the square column IPMC sensor.

To verify the identified model, the dipole source is moved to the third point at $(x_{\mathrm{d3}}, y_{\mathrm{d3}})$ that is 45° from the sensor location, where it vibrates only along the y-direction, as illustrated in Fig. 5.5 (c). The flow velocities at the sensor location in both x-direction and y-direction are first calculated from the measured sphere vibration $v_{\mathrm{x}}^{\mathrm{d}}$, and then fed into the obtained empirical model to predict two sensing outputs of $i_{\mathrm{x}}^{\mathrm{p}}(s)$ and $i_{\mathrm{y}}^{\mathrm{p}}(s)$:

$$\begin{aligned} i_{\mathrm{x}}^{\mathrm{p}}(s) &= V_{\mathrm{x}}(s)G_{\mathrm{xx}}(s) + V_{\mathrm{y}}(s)G_{\mathrm{yx}}(s) \\ &= \frac{a^3}{2\|\mathbf{r_3}\|^5} v_{\mathrm{y}}^{\mathrm{d}}(s)(3(x_{\mathrm{s}} - x_{\mathrm{d3}})(y_{\mathrm{s}} - y_{\mathrm{d3}})G_{\mathrm{xx}} + (2(y_{\mathrm{s}} - y_{\mathrm{d3}})^2 - (x_{\mathrm{s}} - x_{\mathrm{d3}})^2)G_{\mathrm{yx}}), \end{aligned} \tag{5.11}$$

$$\begin{aligned} i_{\mathrm{y}}^{\mathrm{p}}(s) &= V_{\mathrm{x}}(s)G_{\mathrm{xy}}(s) + V_{\mathrm{y}}(s)G_{\mathrm{yy}}(s) \\ &= \frac{a^3}{2\|\mathbf{r_3}\|^5} v_{\mathrm{y}}^{\mathrm{d}}(s)(3(x_{\mathrm{s}} - x_{\mathrm{d3}})(y_{\mathrm{s}} - y_{\mathrm{d3}})G_{\mathrm{xy}} + (2(y_{\mathrm{s}} - y_{\mathrm{d3}})^2 - (x_{\mathrm{s}} - x_{\mathrm{d3}})^2)G_{\mathrm{yy}}), \end{aligned} \tag{5.12}$$

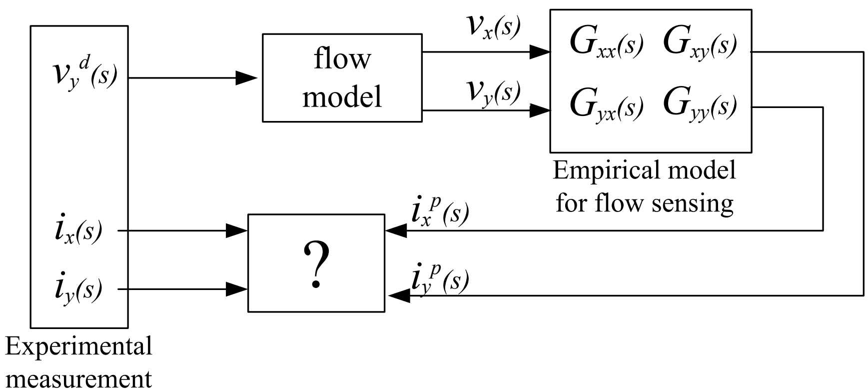

Figure 5.6: The experimental verification process for the identified empirical model.

where

$$\|\mathbf{r_3}\| = \sqrt{(x_\mathrm{s} - x_\mathrm{d3})^2 + (y_\mathrm{s} - y_\mathrm{d3})^2}.$$

The predictions are finally compared with the actual sensing outputs from the measurement, as illustrated in Fig. 5.6.

5.1.3.2 Experimental Results

Experiments are conducted in a water tank which measures $6 \times 2 \times 2$ ft^3, as shown in Fig. 5.7. The mini-shaker is amounted on an aluminum frame above the tank, generating vibration stimulus (back and forth) on the horizontal plane ($x-y$ plane) from 1 to 150 Hz. The dipole source used in this paper is a metallic sphere with diameter of 19.4 mm and excited by the mini-shaker. To meet the assumption that the generated flow is two-dimensional on the $x-y$ plane, the sphere is placed in a depth of 90 mm in the water. The IPMC sensor is tied to a thin stick and extended to the same depth as the dipole source, as shown in Fig. 5.7 (a) and (b). The same data acquisition system in Fig. 5.3 is used to collect the sphere vibration displacement and sensing current signals. With the sensor located in the origin $(0,0)$ mm, the dipole source is placed in three different locations on the same $x-y$ plane: $(-42,0)$ mm, $(0,-50)$ mm, $(-40,-35)$ mm, as illustrated in Fig. 5.5. The

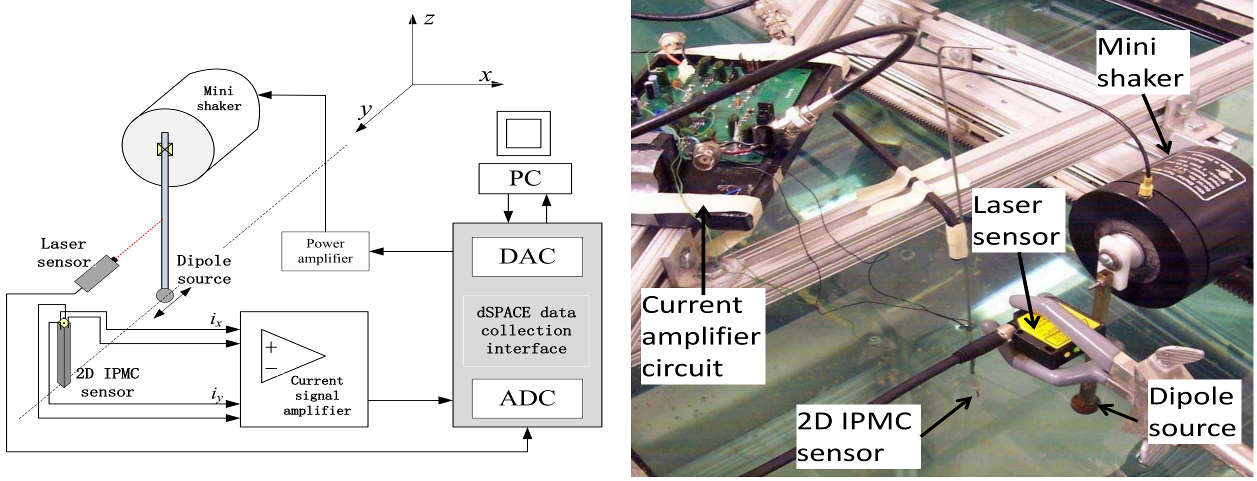

(a) (b)

Figure 5.7: The schematic (a) and photo (b) of the setup for the flow sensing experiments.

signals collected at the first two locations are used to identify the transfer functions while those at the third location are used to verify the identified model.

Fig. 5.8 shows the measured empirical frequency responses and the corresponding transfer function models for $G_{\mathrm{xx}}(s)$, $G_{\mathrm{xy}}(s)$, $G_{\mathrm{yx}}(s)$ and $G_{\mathrm{yy}}(s)$ that are identified based on the measurements. It can be seen that in general the sensor responds well to the flow stimuli in the full frequency range of 1 to 150 Hz. The results also indicate that there possibly exists one or two resonance frequencies around 60 Hz, although the experimental data have been significantly corrupted by the noise around 60 Hz from the power line hum. Further investigation is underway to remove the noise and confirm the existence of resonance frequencies. The identification process of the transfer functions is conducted in Matlab using the function *invfreqs*. Each transfer function is approximated by a rational function of order (8/7) to best match the empirical frequency response both in amplitude and phase. Fig. 5.9 and Fig. 5.10 show the comparison of the measured frequency responses of the sensing currents with the model prediction in the x and y directions, respectively, based on the scheme described in Fig. 5.6. It can be seen that reasonable agreement is achieved

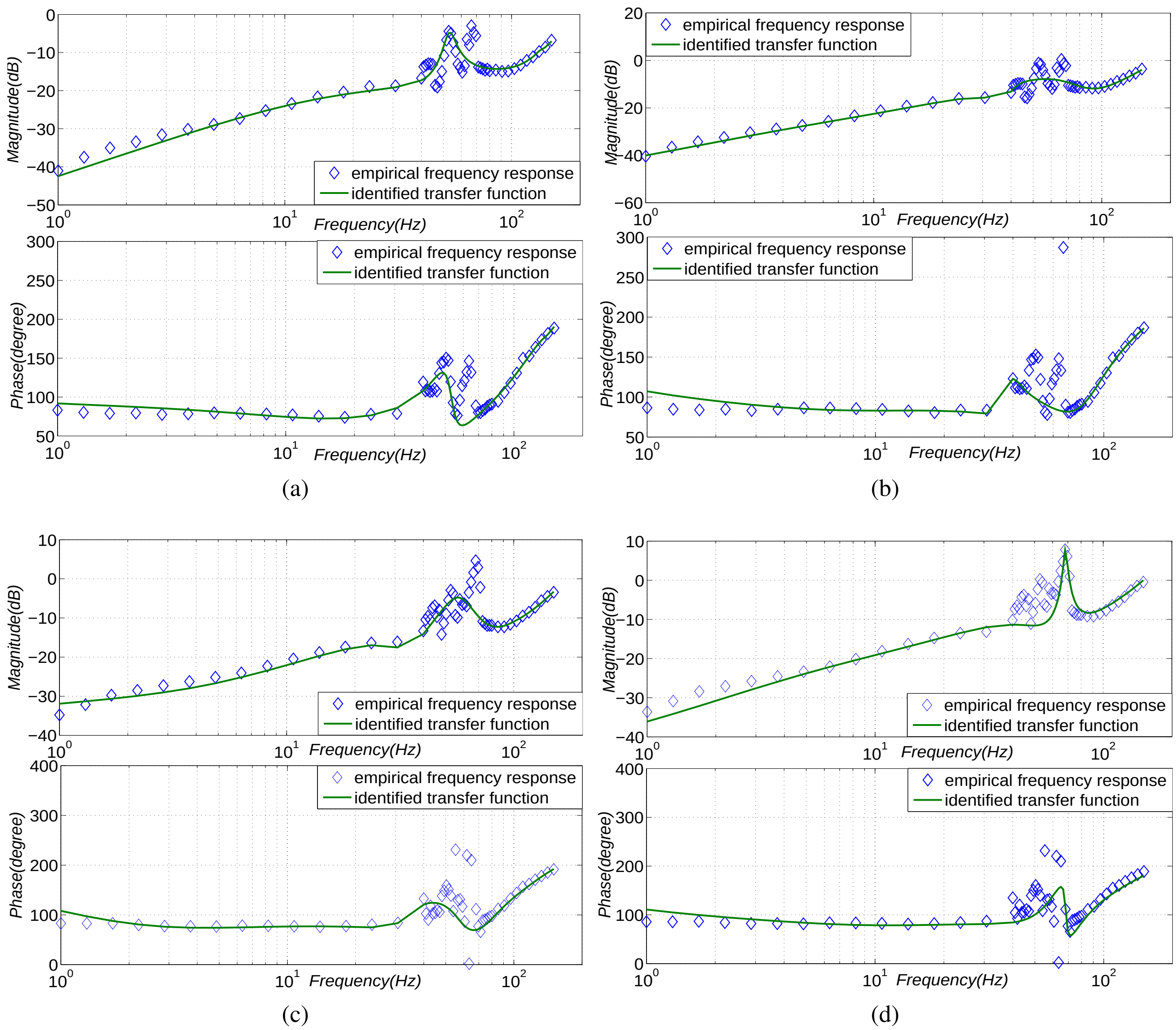

Figure 5.8: Empirical frequency responses and the corresponding identified transfer function models ((a): $G_{\mathrm{xx}}(s)$; (b): $G_{\mathrm{xy}}(s)$); (c): $G_{\mathrm{yx}}(s)$; (d): $G_{\mathrm{yy}}(s)$).

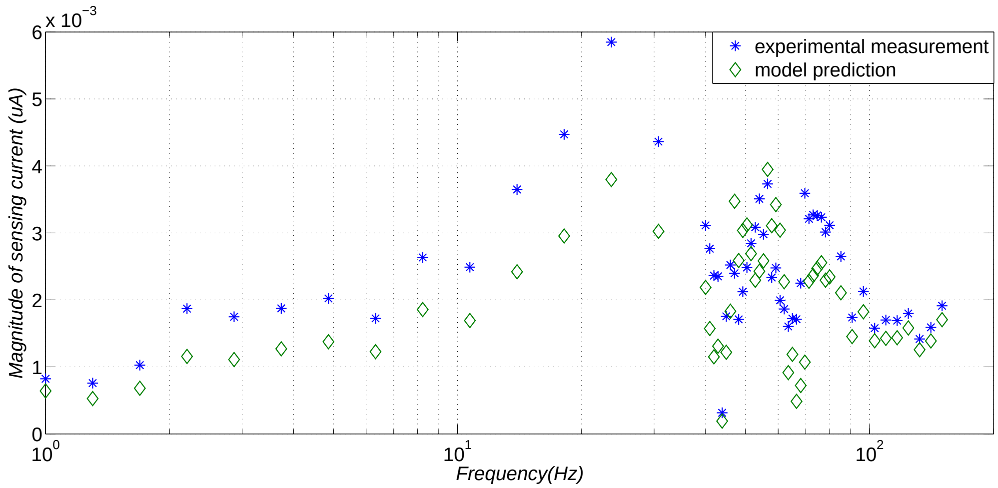

Figure 5.9: Comparison of the measured frequency responses of the sensing currents in x direction with the model prediction.

overall, indicating the promise of the identified empirical model. The discrepancies between the model prediction and the experimental data are attributed to idealistic experimental assumptions in the identification process that the dipole source strictly vibrates along x or y directions, inaccuracies of location measurement under the water, and deviations of the actual flow velocities from the potential flow model.

5.2 Tubular IPMC Sensor: Fabrication, Characterization, and Modeling

The aforementioned IPMC sensor with a shape of square column shows strong coupling effect between two routes of sensing outputs, which make it difficult to develop a promising physical model for such a square-column IPMC sensor. This coupling is primarily rooted in the strain distribution inside a Nafion square column, and most likely strengthened by the asymmetric geometric dimensions and inhomogeneous material properties formed during the fabrication process. In order to deal with this coupling issue, it is necessary to change the geometric structure of the IPMC sensor

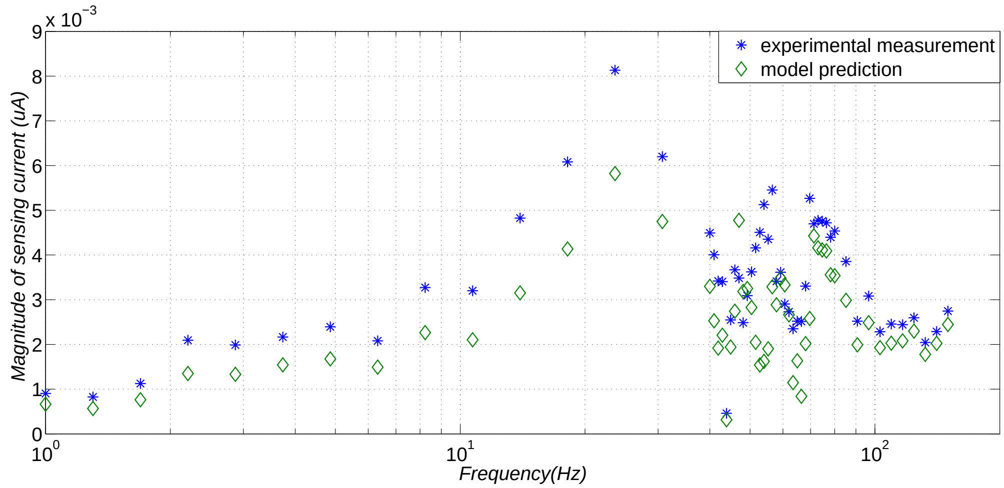

Figure 5.10: Comparison of the measured frequency responses of the sensing currents in y direction with the model prediction.

and improve the fabrication process. Therefore, we further develop a tubular thin-wall IPMC sensor which is capable of two-dimensional sensing as well. The tubular thin-wall structure enables us to simplify the coupling issue by limiting the electrical field in the radial direction, and the new fabrication process based on Nafion tubing minimizes those uncertainties that are encountered in the fabrication of square column IPMC.

5.2.1 Sensor Fabrication and Packaging

5.2.1.1 Tubular IPMC Fabrication

The fabrication of the tubular IPMC uses Nafion tubing (TT-110, Perma Pure LLC) as the starting material, and the process flow otherwise follows the traditional IPMC fabrication approach [6]. First, the Nafion tubing is boiled in dilute hydrochloric acid (2 wt%) for an hour to release the internal stress and remove impurities. Then the tubing is boiled in the deionized (DI) water for another hour to further release the stress and remove the acid. After these pre-treatments, the tubing is submerged in a platinum complex solution ($[Pt(NH_3)_4]Cl_2$) for overnight so that the platinum ions would diffuse into the Nafion polymer and exchange with the hydrogen ions. Followed by the DI water rinse, the Nafion tubing is gently stirred in a water bath where the reducing agent of sodium borohydride solution (5 wt% $NaBH_4$ aq) is added for every half an hour with the amount of 2 ml, as the temperature of the water bath is raised from 40 °C to 60 °C gradually. After the reduction process, the platinum is deposited on the inner and outer surfaces as electrodes. To reduce the surface resistance, a second deposition of platinum is conducted by repeating those steps from the acid treatment to the reduction. The tubular IPMC sensor reported in this work has an inner diameter of 2.24 mm, outer diameter of 2.77 mm, wall thickness of 265 μm, and length of 30 mm.

5.2.1.2 Sensor Packaging

Before we use the fabricated tubular IPMC as a sensor, we first need to cut off the two tubing ends to avoid short-circuit between the inner and outer electrodes. The outer electrode is then patterned into four sub-electrodes equally, while the inner electrode is left untouched. In particular, a 3D-printed device is used to facilitate the electrode patterning, as shown in Fig. 5.11. The tubular IPMC is first fit on the holding stick tightly and covered with four mask pieces. These mask pieces are designed to form a tubular shape with small gaps (around 0.2 mm) between the neighboring pieces. Then a blade is used to carefully remove the outer electrode along the gaps. Fig. 5.12 illustrates the tubular IPMC sensor with four equally divided outer electrodes.

Compared with the common beam-shaped IPMC sensors, it is relatively difficult to connect conductive wires to the electrodes of the tubular IPMC. A custom-made apparatus is used to make electrical contacts for the sensor. A substrate is first 3D-printed, with a base stem on the center to hold the tubular IPMC and with hollow arrows on the surface for the alignment purpose. Bare copper wires are then wrapped around the loading area of the stem to achieve perfect peripheral

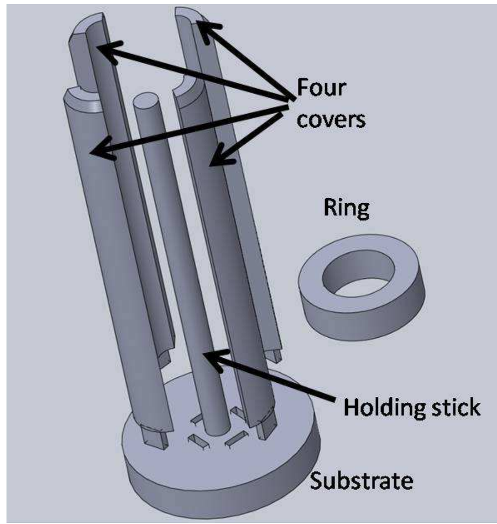

Figure 5.11: 3D-printed device for patterning the outer electrode.

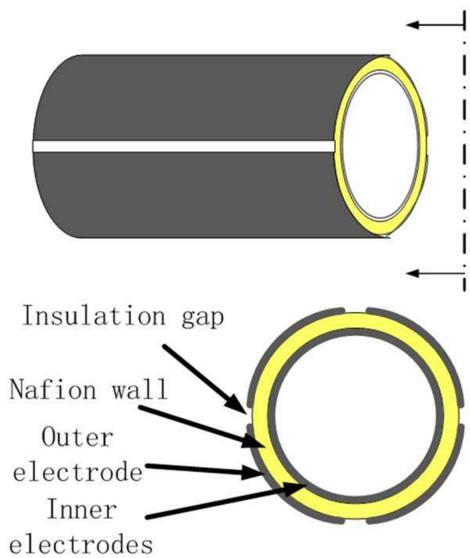

Figure 5.12: Illustration of tubular IPMC with four equally divided outer electrodes (dimensions are not to scale).

contact between the wires and the inner electrode. Note that the stem is only 3.5 mm high and used to hold the sensor base only, so the tubular IPMC can still bend freely. After the sensor is placed on the base stem and its insulation gaps are aligned with the hollow arrows, four base covers attached with wires are inserted into the substrate to connect the conductive wires to each outer sub-electrode. At last, the base covers are fastened by a ring to enhance the contact.

The completed tubular IPMC sensor has five wires, as shown in Fig. 5.13. There are several ways to configure these wires as outputs. One configuration is to ignore the inner electrode and use each pair of wires (i_1 and i_3, or, i_2 and i_4) as one route. This configuration would suffer from severe electrical coupling between the two routes through inner electrode. Unless noted, for the rest of the paper, we adopt a four-route configuration, where the wire connected with the inner electrode is used as the common ground and the other four wires are used as separate sensor signals.

5.2.2 Sensor Characterization

5.2.2.1 Experimental Setup

To evaluate its omnidirectional sensing behavior, we subject the tubular IPMC sensor to tip bending at different orientations. Fig. 5.14 shows the experimental setup, including a custom-designed angle plate, on which the tubular IPMC sensor package can be mounted with different orientations by aligning the hollow arrow on the sensor substrate (see Fig. 5.13) with the angle scale (from 0° to 360°) on the angle plate. The angle plate together with the tubular IPMC sensor package is fixed on an aluminum frame, while the tip of the IPMC sensor is excited by a 3D-printed stick, which is mounted on a mini-shaker (Type 4810, Brüel & Kjær). The shaker generates vibration stimuli with frequencies ranging from 1 Hz to 20 Hz. The vibration orientation of the shaker is fixed (up and down), but its amplitude is controllable. A laser displacement sensor (OADM 20I6441/S14F,

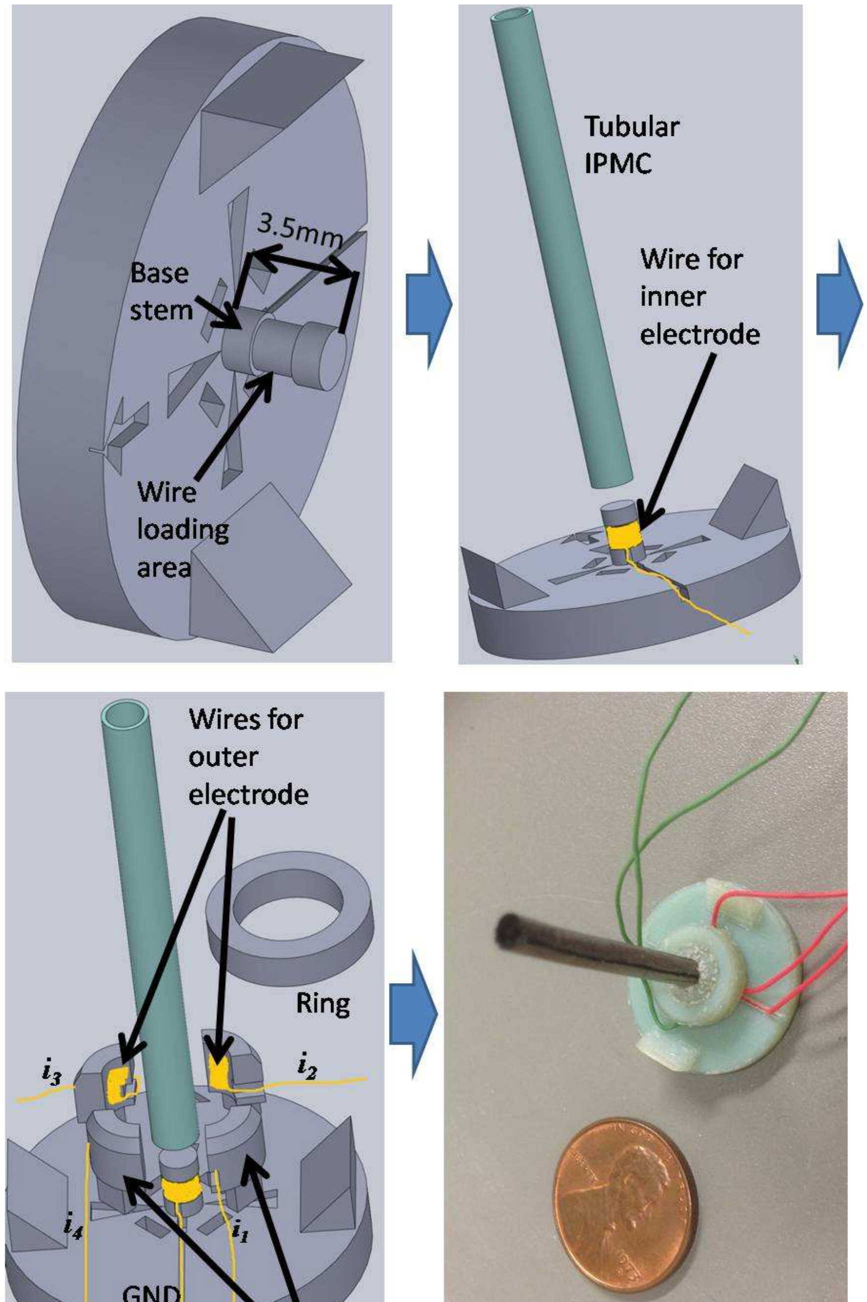

Figure 5.13: Packaging and wiring scheme of a tubular IPMC sensor.

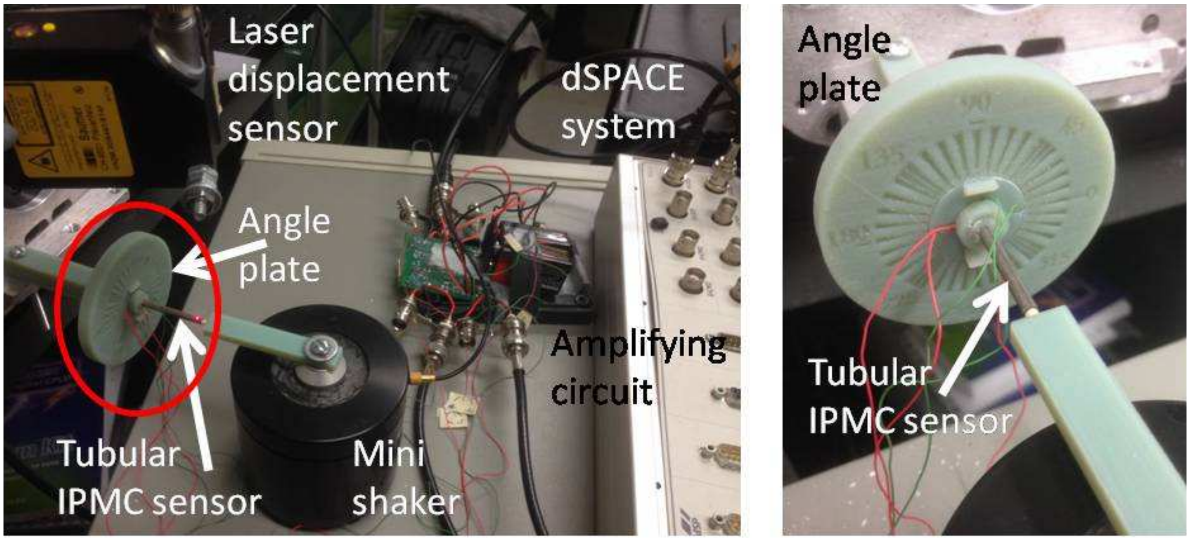

Figure 5.14: Experimental setup for the characterization of the tubular IPMC sensor.

Baumer Electric) is mounted above the tubular IPMC sensor to measure its tip displacement. The mounting frame for the laser sensor is isolated from the table where the mini-shaker is placed. A two-tier, four-channel amplification circuit [63] is used to measure the short-circuit currents in all four routes of the IPMC sensor. Control signal generation, sensing data acquisition, and processing are all performed through a dSPACE system.

Starting from 0° on the angle plate for the sensor orientation, frequency responses of all four routes under tip excitations are collected every 10°. Fast Fourier transform is used to extract the amplitudes of the four sensor outputs and the tip displacements at each frequency and each orientation, which are used to evaluate the sensor performances. Unless noted otherwise, all the data points in the rest of this paper are processed in this way and presented in the form of gain and phase shift, with the tip displacement as the input and the four routes of sensing currents as the outputs. For the convenience of discussion, we fix the local two-dimensional coordinate system $x-y$ in the cross-section plane of the tubular IPMC sensor, and the orientation of the tip excitation $u(t)$ in this coordinate system is denoted as γ, as illustrated in Fig. 5.15. Note that the wall of the IPMC sensor is divided into four portions denoted as A to D, corresponding to four routes 1 to 4.

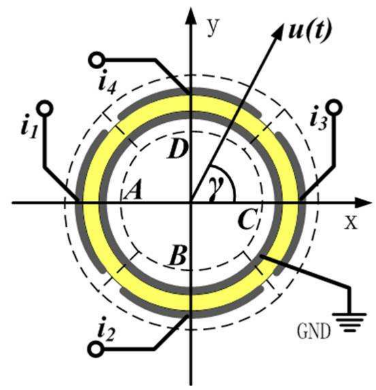

Figure 5.15: Local 2D coordinate system on the cross-section of the tubular IPMC.

5.2.2.2 Results and Discussion: Frequency Responses at a Fixed Orientation

Empirical frequency responses of all four routes of the tubular IPMC sensor are first examined for some fixed-orientation tip excitation. Fig. 5.16 shows the experimental results when the orientation angle γ is fixed at 45°. For the frequency response of each route, it can be seen that, with an increasing frequency (within the tested range) the magnitude increases while the phase shift (for the most part) drops. The latter trend represents similarity to that observed in beam-shaped IPMC sensors [29, 78]. Comparing different routes in Fig. 5.16, one can see that the sensing responses of all four routes have slightly different magnitudes at each frequency, which is not expected at the orientation angle of 45°. Due to the symmetric configuration shown in Fig. 5.15, the signal amplitudes of all four routes are expected to be equal when the orientation angle is 45°, 135°, 225° or 315°. The differences of sensitivity among the four routes are believed to be caused by the inhomogeneous material properties formed during the IPMC fabrication process, the imperfect patterning of the outer electrode, and the different contact resistances for the routes. The proposed model in Section 5.2.3 will capture the effect of contact resistance.

The phase shifts for all the routes in Fig. 5.16 show excellent consistency and their relationships match expectations. For example, route 4 and route 3 always have phase shifts close to each other at every frequency, while route 4 and route 1 always have a phase difference close to 180°. This can

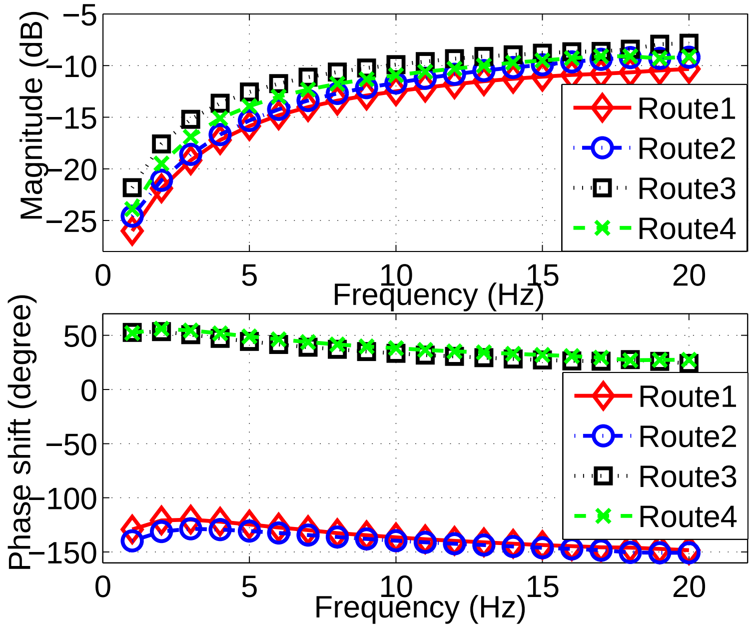

Figure 5.16: Measured frequency responses at the stimulus orientation of 45°.

be explained by the axial stress distribution as illustrated in Fig. 5.17 for $\gamma = 45^\circ$. In particular, the axial stress distributions on segments A and D (likewise for segments B and C) are always skew-symmetric, and thus the sensing currents of routes 1 and 4 always have a phase difference of 180°. Similarly, at $\gamma = 45^\circ$, routes 1 and 2 (and routes 3 and 4) always have the same polarities.

5.2.2.3 Results and Discussion: Sensor Responses under Omnidirectional Stimulus

The response of the tubular IPMC sensor is further characterized with the tip excitation applied at different orientations. Fig. 5.18 shows the response of route 3 at the fixed frequency of 5 Hz. Similar trends are observed at other frequencies. Note that the unit of the frequency response magnitude has been changed from decibel to the physical unit of μA/mm to present the experimental results more directly. First, one can see that there exists some periodic trend for the sensing response as the tip-excitation orientation γ varies. In particular, when γ is close to 90° and 270°, the signal magnitude drops to almost zero and the phase shift jumps with reversed polarity. This can be explained qualitatively by the induced normal stress distributed on the specific region of segment

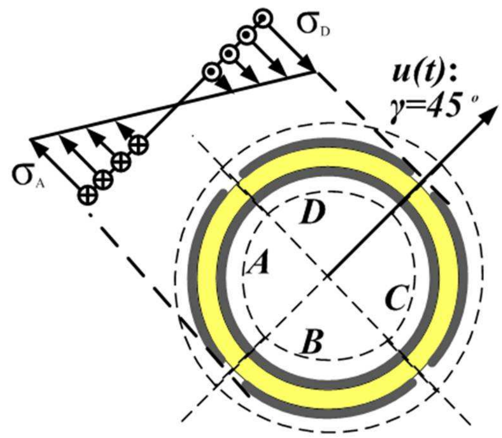

Figure 5.17: Illustration of axial stress distribution for route 1 and 4 at the orientation stimulus of 45°.

C (corresponding to route 3) in the tube cross-section, as shown in Fig. 5.19. When the excitation is along the orientation of 90° or 270°, the upper and lower parts of *C* (with respect to the *x*-axis) have skew-symmetric induced stress distribution, canceling out each other's contributions to the sensing output. In addition, except around several jumping points, the phase shift maintains consistent, indicating that the varying orientations of the tip excitation only affect the signal polarity of each route while the phase shift is primarily determined by the charge dynamics inside the tubular IPMC.

Fig. 5.20 and Fig. 5.21 show the sensor responses at 10 Hz at varying orientations for antagonistic routes and neighboring routes, respectively. Note that similar responses have been observed at other frequencies. First, one can see that all the routes have similar trends as shown in Fig. 5.18, including the periodic feature of the magnitude response and the jumping points in the phase shift. In particular, for a pair of antagonistic routes, like 2 and 4 in Fig. 5.20, they generally have similar periodic properties except that their signal polarities are opposite. For a pair of neighboring routes, like 2 and 3 in Fig. 5.21, their sensing responses (both magnitude and phase shift) have a shift of about 90° with respect to the stimulus orientation angle. These characterization results suggest that the relationships between the sensing outputs of different routes are primarily determined by

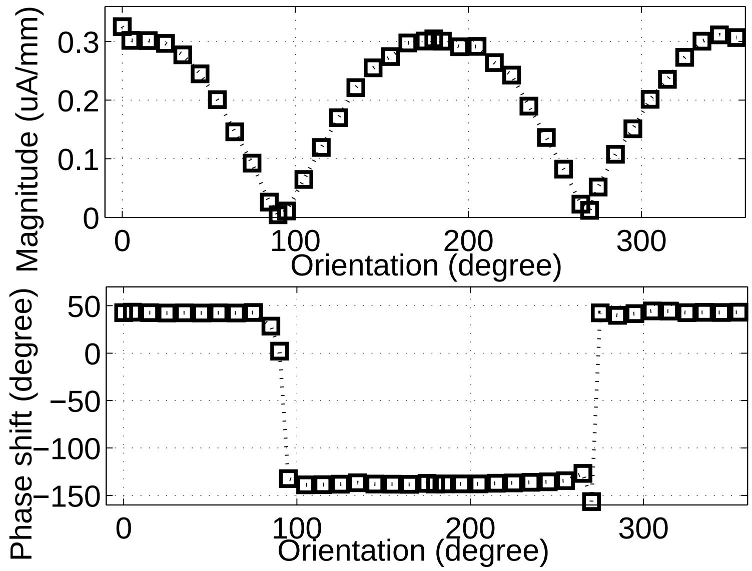

Figure 5.18: Measured sensor response of route 3 at varying stimulus orientations at the frequency of 5 Hz.

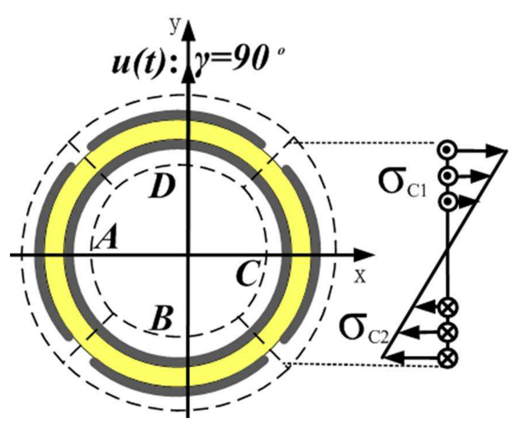

Figure 5.19: Illustration of stress distribution for route 3 at the stimulus orientation of 90°.

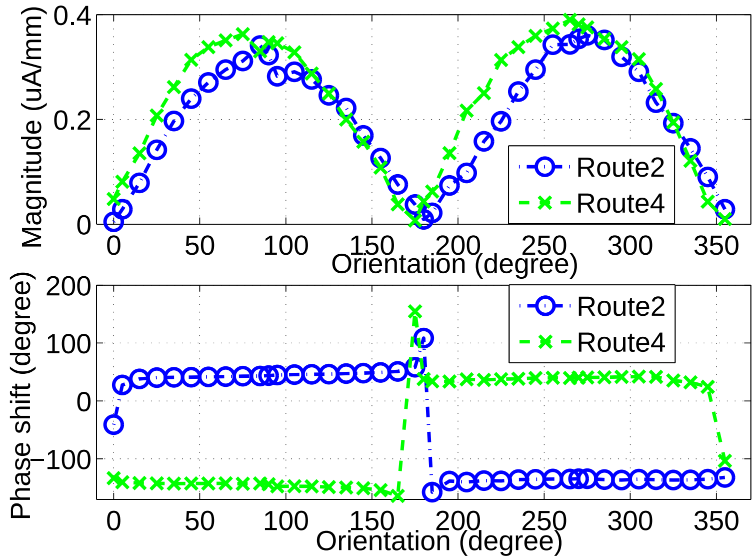

Figure 5.20: Measured sensor responses of routes 2 and 4 at varying stimulus orientations at 10 Hz.

the mechanical coupling. In other words, the tubular IPMC sensor can be treated as a mechanical combination of four separate IPMC sensors through a tubular structure.

5.2.3 Physical Modeling

5.2.3.1 Modeling Assumptions

Based on the experimental results and discussions in Section 5.2.2, we propose a dynamic physical model for the tubular IPMC sensor under tip excitation. Consider Fig. 5.22, where the tubular IPMC with the length of L is clamped at the base and subjected to a tip displacement $u(t)$, producing four routes of sensing current $i_1(t)$ to $i_4(t)$. The neutral axis of the tube is denoted by $x = 0$ and $y = 0$. The outer radius and the inner radius are denoted by r_2 and r_1, respectively. The wall thickness is denoted by $2h = r_2 - r_1$. The $x - y$ plane is parallel to the cross-section of the tube. We assume that the tubular IPMC sensor is geometrically symmetric and the widths of the insulation gaps on the outer electrode are negligible. With two platinum deposition steps, the surface resis-

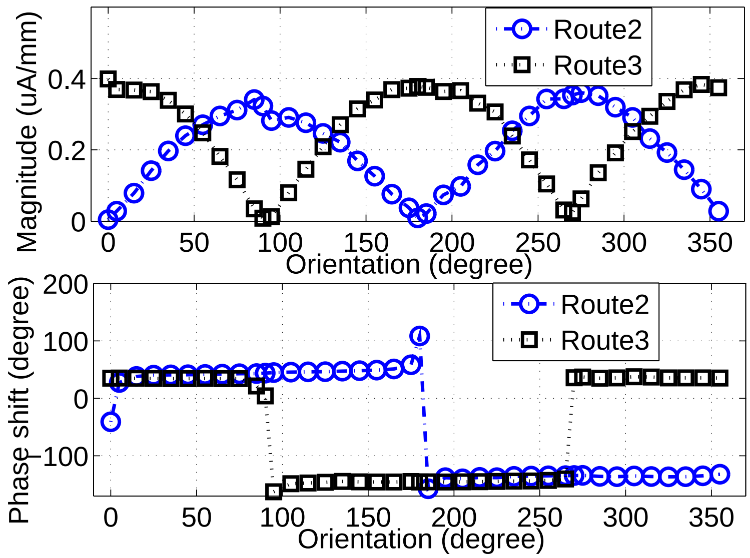

Figure 5.21: Measured sensor responses of routes 2 and 3 at varying stimulus orientations at 10 Hz.

tances of the inner and outer electrodes are very small and thus we assume the surface electrodes to be perfectly conductive. Note that the contact resistance between the surface electrode and the conductive wire for each route is not ignored, because the conductive wire is not soldered onto the surface electrode, which results in relatively large contact resistance. Considering that the wall thickness of the IPMC sensor is much smaller than the tube diameter, we further assume that the electric field E within the polymer of the tube wall is restricted to the normal directions of the tube surface, which is similar to the assumption made for traditional beam-shape IPMCs [7]. Since the sensor base is fixed and the sensor tip is subjected to prescribed deflection, we consider that the mechanical deformation of the tube is quasi-static under the relatively low-frequency (up to 20 Hz) tip stimuli. Finally, we assume that the tube excitation is sufficiently small, and therefore, the Brazier effect [79] of the tube bending is ignored.

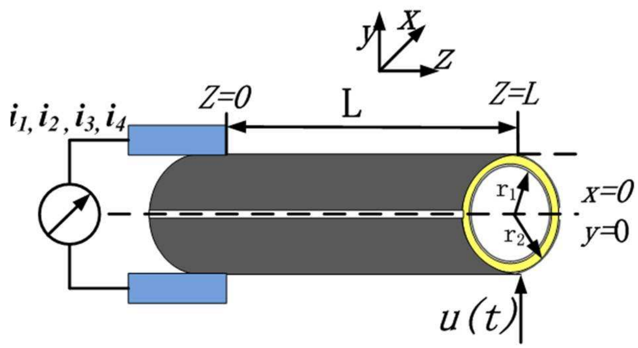

Figure 5.22: Configuration of the tubular IPMC sensor subjected to the tip excitation $u(t)$.

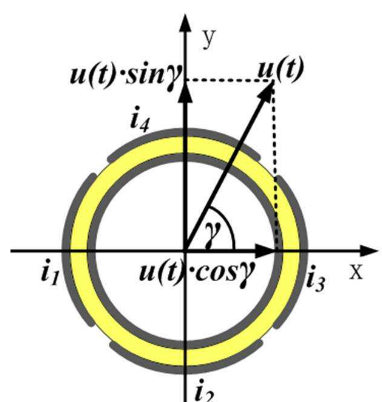

Figure 5.23: Decomposition of the tip excitation.

5.2.3.2 Overview of the Modeling Approach

We consider an arbitrary excitation $u(t)$ with an orientation angle of γ, as shown in Fig. 5.23. $u(t)$ can be decomposed into two components of $u_x(t) = u(t)\cos\gamma$ and $u_y(t) = u(t)\sin\gamma$ in the $x-$ and $y-$direction, respectively. We first model the sensor outputs induced by $u_y(t)$, as shown in Fig. 5.24. Now we consider an infinitesimal slice $p_{\mathrm{d}\alpha}$ on the tube wall with the length of L and the thickness of $2h$. The angle from $p_{\mathrm{d}\alpha}$ to $u_y(t)$ is denoted as α (radian), so the width of $p_{\mathrm{d}\alpha}$ is approximated as $W = r \cdot \mathrm{d}\alpha$, where $r = (r_1 + r_2)/2$. The contact resistance for $p_{\mathrm{d}\alpha}$ is denoted as $R_c = R(j)\frac{0.5\pi}{\mathrm{d}\alpha}$, where $R(j)$, $j = 1,2,3,4$, is the measured contact resistance for route j that $p_{\mathrm{d}\alpha}$ belongs to. Then the displacement $u_y(t)$ can be decomposed into two components of $u_c(t,\alpha) = u_y(t)\cos\alpha$ and $u_s(t,\alpha) = u_y(t)\sin\alpha$, as shown in Fig. 5.24. Following the assumption that the electric field E inside the polymer is restricted to the radial direction, $p_{\mathrm{d}\alpha}$ only responds to $u_y(t)\cos\alpha$. Thus $p_{\mathrm{d}\alpha}$ can be treated as a traditional beam-shaped IPMC with the width of $r \cdot \mathrm{d}\alpha$ and the thickness of $2h$, as shown in Fig. 5.25 where a new coordinate system $x' - y'$ for the cross-section has been set up for the convenience of discussion. Following the similar derivation as in [29], the induced sensing current from $p_{\mathrm{d}\alpha}$ can be obtained by incorporating certain boundary conditions that are determined by the stress distribution and the contact resistance. At last, the total sensing current for each route induced by $u_y(t)$ can be obtained by integrating the sensing current of $p_{\mathrm{d}\alpha}$ around the tube for the given route. Similarly, we can model the sensor outputs induced by $u_x(t)$. Further details are provided in Section 5.2.3.3 and Section 5.2.3.4.

5.2.3.3 Modeling of the Sensing Output from Slice $P_{\mathrm{d}\alpha}$

As shown in Fig. 5.25, $p_{\mathrm{d}\alpha}$ can be viewed as a beam-shaped IPMC sensor. We can model the sensing response of $p_{\mathrm{d}\alpha}$ based on the governing PDE for charge density distribution ρ within

IPMC [7], which is given by

$$
\begin{aligned}
\frac{\rho(x',z,t)}{\partial t} - d\frac{\partial^2 \rho(x',z,t)}{\partial (x')^2} + \\
\frac{F^2 dC^-}{\kappa_e RT}(1 - C^- \triangle V)\rho(x',z,t) = 0,
\end{aligned} \tag{5.13}
$$

where F is Faraday's constant, R is the gas constant, T is the absolute temperature, d is the ionic diffusivity, κ_e is the effective dielectric constant of the polymer, C^- is the anion concentration ($\mathrm{mol/m^3}$), and the volumetric change of $\triangle V$ represents how much the polymer volume swells after taking water.

The exact solution to (5.13) can be obtained in the Laplace domain with appropriate boundary conditions, which are determined based on the assumption [29] that the charge density $\rho(x',z,s)$ is proportional to the mechanically induced stress $\sigma(x',z,s)$ at the boundary $x' = \pm h$. Note that even though $p_{\mathrm{d}\alpha}$ is treated as a beam structure here, the stress $\sigma(x',z,s)$ on $p_{\mathrm{d}\alpha}$ is still calculated based on the tubular structure, as shown in the complete derivation given in Appendix C. In particular, we can derive, for $-h \le x' \le h$,

$$
\rho(x',z,s) = a_1(z,s)e^{-\beta(s)x'} + a_2(z,s)e^{\beta(s)x'}, \tag{5.14}
$$

where $\beta(s) = \sqrt{\frac{s+K}{d}}$, $K \triangleq \frac{F^2 dC^-}{\kappa_e RT}(1 - C^- \triangle V)$, and $a_1(z,s)$ and $a_2(z,s)$ are as given in Appendix C.

Let D, E, and ϕ denote the electrical displacement, electric field, and electric potential, respectively. Then the following equations hold:

$$
D(x',z,s) = \kappa_e E(x',z,s), \tag{5.15}
$$

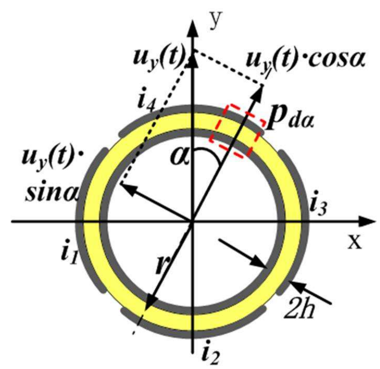

Figure 5.24: Cross-section of the tubular IPMC sensor subjected to the tip excitation.

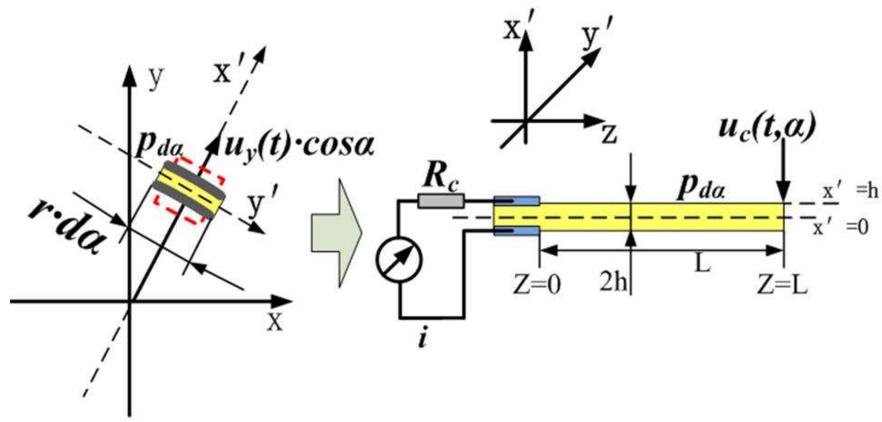

Figure 5.25: One infinitesimal part $p_{\mathrm{d}\alpha}$ on the cross-section.

$$E(x',z,s) = -\frac{\partial \phi(x',z,s)}{\partial x'}, \tag{5.16}$$

$$\kappa_e \frac{\partial E(x',z,s)}{\partial x'} = \rho(x',z,s). \tag{5.17}$$

With (5.14) and (5.17), we can solve for $E(x',z,s)$ for this infinitesimal part $p_{\mathrm{d}\alpha}$ using appropriate boundary conditions at $x' = \pm h$. With the assumption that the inner and outer electrodes are perfectly conductive, the electric potential is uniform across both surfaces $x' = \pm h$. Since the inner electrode is used as the common ground, the potential $\phi(-h,z,s)$ is set to be zero. Due to the existence of the contact resistance, the sensing currents of the tubular IPMC sensor are not treated as short-circuit currents; therefore, at $x' = h$ the potential $\phi(h,z,s) = R_c i(s)$ is not equal to zero but dependent on the contact resistance, as illustrated in the Fig. 5.25. The sensing current is the time derivative of the induced charge $Q(t)$, which implies $i(s) = sQ(s)$, and the total induced sensing charge can be obtained by integrating the electrical displacement D on the boundary $x' = h$. Therefore, we have the following boundary conditions to solve for $E(x',z,s)$ (see Appendix D for details):

$$\phi(-h,z,s) = 0, \tag{5.18}$$

$$\phi(h,z,s) = R_c sQ(s) = R_c s \int_0^L \int_0^W k_e E(h,z,s) \mathrm{d}y' \mathrm{d}z. \tag{5.19}$$

With knowing $E(x',z,s)$, one can further derive the charge $Q(s)$ and the sensing current $i(s)$ induced on $p_{\mathrm{d}\alpha}$ based on the discussion above. To make the following discussion more clear, we use new notation, $\mathrm{d}Q(s,\alpha)$ and $\mathrm{d}i(s,\alpha)$, to replace the notation $Q(s)$ and $i(s)$, respectively. The sensing current on $p_{\mathrm{d}\alpha}$ is linear with respect to the external stimulus $u_c(s,\alpha)$:

$$\mathrm{d}i(s,\alpha) = \frac{u_c(s,\alpha)3YWhs}{\alpha_o L\beta^2(s)(R_c\kappa_e WLs+2h)}(\beta(s)(e^{\beta(s)h}\beta_2(s) - e^{-\beta(s)h}\beta_1(s) + (e^{-\beta(s)h} - e^{\beta(s)h})(\beta_2(s)-\beta_1(s)))), \tag{5.20}$$

where α_o is the charge-stress coupling constant, and

$$\beta_1(s) = \frac{r_2 - r_1 e^{2\beta(s)h}}{e^{-\beta(s)h} - e^{3\beta(s)h}}, \tag{5.21}$$

$$\beta_2(s) = \frac{r_1 - r_2 e^{2\beta(s)h}}{e^{-\beta(s)h} - e^{3\beta(s)h}}. \tag{5.22}$$

5.2.3.4 Modeling of the Sensing Output from Each Route

Note that $p_{\mathrm{d}\alpha}$ is an infinitesimal part at angle α. The total induced sensing current for one route can be obtained by integrating $\mathrm{d}i(s,\alpha)$ over α. Take route 1 for example. We denote R_1 as the measured contact resistance of route 1, and plug $R_c = R_1\frac{0.5\pi}{\mathrm{d}\alpha}$, $W = r\cdot\mathrm{d}\alpha$, and $u_c(s,\alpha) = u_y(s)\cos\alpha$ into (5.20):

$$\mathrm{d}i(s,\alpha) = \frac{i_0(s)}{\frac{\pi}{2}R_1\kappa_e rLs+2h}u(s)\cos\alpha\mathrm{d}\alpha, \tag{5.23}$$

$$\text{with } i_0(s) = \frac{3Yrhs}{\alpha_o L\beta^2(s)}(\beta(s)(e^{\beta(s)h}\beta_2(s) - e^{-\beta(s)h}\beta_1(s)) + (e^{-\beta(s)h} - e^{\beta(s)h})(\beta_2(s)-\beta_1(s))), \tag{5.24}$$

We can then integrate (5.23) from $\alpha = \frac{5\pi}{4}$ to $\alpha = \frac{7\pi}{4}$ for route 1, and obtain the total sensing current induced by the $y-$component of $u(s)$ (recall Fig. 5.24) as

$$i_{1y}(s) = \int_{\frac{5\pi}{4}}^{\frac{7\pi}{4}} \frac{i_0(s)}{\frac{\pi}{2}R_1\kappa_e rLs + 2h} u(s)\cos\alpha \mathrm{d}\alpha = 0. \tag{5.25}$$

Similarly, the total sensing currents induced by $u_y(s)$ for other routes are given by

$$i_{2y}(s) = \frac{-\sqrt{2}i_0(s)}{\frac{\pi}{2}R_2\kappa_e rLs + 2h} u(s), \tag{5.26}$$

$$i_{3y}(s) = 0, \tag{5.27}$$

$$i_{4y}(s) = \frac{\sqrt{2}i_0(s)}{\frac{\pi}{2}R_4\kappa_e rLs + 2h} u(s). \tag{5.28}$$

Now considering the sensing outputs due to the $x-$component of the input, $u_x(t) = u(t)\cos\gamma$, we have

$$i_{1x}(s) = \frac{-\sqrt{2}i_0(s)}{\frac{\pi}{2}R_1\kappa_e rLs + 2h} u(s), \tag{5.29}$$

$$i_{3x}(s) = \frac{\sqrt{2}i_0(s)}{\frac{\pi}{2}R_3\kappa_e rLs + 2h} u(s), \tag{5.30}$$

$$i_{2x}(s) = i_{4x}(s) = 0. \tag{5.31}$$

Based on the results from (5.25) to (5.29), we can see that routes 1 and 3 only respond to the $x-$component of the tip stimulus, $u(t)\cos\gamma$, and routes 2 and 4 only respond to the $y-$ component of the stimulus, $u(t)\sin\gamma$. Hence, the complete dynamic model for the tubular IPMC sensor subjected to tip excitation $u(t)$ with the angle of γ is

$$H_1(s) = \frac{i_1(s)}{u(s)} = -C_1 \frac{H_0(s)}{\frac{\pi}{2}R_1\kappa_e rLs + 2h}\cos\gamma, \tag{5.32}$$

$$H_2(s) = \frac{i_2(s)}{u(s)} = -C_2 \frac{H_0(s)}{\frac{\pi}{2}R_2\kappa_e rLs + 2h}\sin\gamma, \tag{5.33}$$

$$H_3(s) = \frac{i_3(s)}{u(s)} = C_3 \frac{H_0(s)}{\frac{\pi}{2}R_3\kappa_e rLs + 2h}\cos\gamma, \tag{5.34}$$

$$H_4(s) = \frac{i_4(s)}{u(s)} = C_4 \frac{H_0(s)}{\frac{\pi}{2}R_4\kappa_e rLs + 2h}\sin\gamma, \tag{5.35}$$

$$\begin{aligned}\text{with } H_0(s) = \frac{3\sqrt{2}Yrhs}{\alpha_o L\beta^2(s)}&(\beta(s)(e^{\beta(s)h}\beta_2(s) - e^{-\beta(s)h}\beta_1(s)) \\ &+ (e^{-\beta(s)h} - e^{\beta(s)h})(\beta_2(s) - \beta_1(s))),\end{aligned} \tag{5.36}$$

where additional constants C_1 to C_4 have been introduced to accommodate the sensitivity differences among different routes, as evidenced in Fig. 5.16 and discussed in Section 5.2.2.2.

5.2.3.5 Model Reduction

The sensing model shown in (5.32) to (5.35) is infinite-dimensional since it involves irrational functions such as $e^{(\cdot)}$ and $\sqrt{\cdot}$. For practical implementation of stimulus reconstruction or feedback control design, it is of interest to reduce the model to a finite order. First, we take $1 - C^{-}\Delta V \approx 1$ since $\left|C^{-}\Delta V\right| \ll 1$ [7]. Based on the measured and identified physical parameters (see Table 5.1 and Table 5.2 in Section 5.2.3.6), for $s = j\omega$, one has $|\beta(s)h| = \left|h\sqrt{\frac{s+K}{d}}\right| > 100$ and $e^{-\beta(s)h} -$

$e^{3\beta(s)h} \approx -e^{3\beta(s)h}$, when the angular frequency ω is relatively low. We can then simplify $\beta_1(s)$ as

$$\beta_1(s) \approx \frac{r_2 - r_1 e^{2\beta(s)h}}{-e^{3\beta(s)h}} \approx \frac{r_1}{e^{\beta(s)h}}. \tag{5.37}$$

Similarly, $\beta_2(s)$ can be simplified as $\frac{r_2}{e^{\beta(s)h}}$. Then we have

$$\begin{aligned}
&(e^{-\beta(s)h} - e^{\beta(s)h})(\beta_2(s) - \beta_1(s)) = \frac{2h}{e^{2\beta(s)h}} - 2h, \\
&\beta(s)(e^{\beta(s)h}\beta_2(s) - e^{-\beta(s)h}\beta_1(s)) = \beta(s)r_2 - \frac{\beta(s)r_1}{e^{2\beta(s)h}}, \\
&(e^{-\beta(s)h} - e^{\beta(s)h})(\beta_2(s) - \beta_1(s)) \\
&+\beta(s)(e^{\beta(s)h}\beta_2(s) - e^{-\beta(s)h}\beta_1(s)) \\
&= \beta(s)r_2 - 2h + \frac{1}{e^{2\beta(s)h}}(2h - \beta(s)r_1),
\end{aligned}$$

where $\frac{1}{e^{2\beta(s)h}}(2h - \beta(s)r_1) \approx 0$, which yields

$$H_0(s) = \frac{3\sqrt{2}Y rhs(\beta(s)r_2 - 2h)}{\alpha_o L\beta^2(s)}.$$

Now, for example, the transfer function $H_1(s)$ of route 1 becomes

$$\begin{aligned}
\hat{H}_1(s) &= -C_1 \frac{H_0(s)}{\frac{\pi}{2}R_1\kappa_e rLs + 2h}\cos\gamma \\
&= \frac{-3\sqrt{2}C_1 Y rh\cos\gamma(\beta(s)r_2 - 2h)s}{\alpha_o L\beta^2(s)(\frac{\pi}{2}R_1\kappa_e rLs + 2h)}.
\end{aligned} \tag{5.38}$$

Plugging $\beta(s) = \sqrt{\frac{s+K}{d}}$ into (5.38), we have

$$\hat{H}_1(s) = \frac{6\sqrt{2d}C_1 Y rh\cos\gamma s(\sqrt{s+K}r_2 - 2h\sqrt{d})}{\alpha_o L(\pi R_1\kappa_e rLs + 4h)(s+K)}. \tag{5.39}$$

To further reduce (5.39) to a finite order, we approximate $\sqrt{s+K}$ with a rational function of s based on Padé approximation [66]. It is found that the Padé approximation of the order (3/2) can provide adequate approximation with minimal complexity for $\sqrt{s+K}$ around some point s_0, where $s_0 = |j\omega_0|$ and ω_0 is close to the midpoint of the angular frequency range one is interested in. In this paper, we take $s_0 = 60$, because the frequency range considered in our experiments is from 1 Hz to 20 Hz. The resulting finite-dimensional approximation to $H_1(s)$ is

$$\hat{H}_1(s) = \frac{6\sqrt{2d}C_1 Y rh \cos\gamma s}{\alpha_o L} \frac{p_3 s^3 + p_2 s^2 + p_1 s + p_0}{q_4 s^4 + q_3 s^3 + q_2 s^2 + q_1 s + q_0}, \tag{5.40}$$

where coefficients of $p_0, \cdots, p_3$ are dependent on [K, s_0, r_2, d, h], and coefficients of $q_0, \cdots, q_4$ are dependent on [K, s_0, h, R_1, κ_e, r, L].

With the same strategy, analogous results can be obtained for the other three routes. Note that the reduced model (5.40) is still a physics-based model since it is expressed in terms of fundamental physical parameters. The reduced model will be used for parameter identification, model validation, and stimulus reconstruction given the sensor output.

5.2.3.6 Model Validation

1)Parameter Identification: To validate the proposed model, physical parameters in the model need to be identified first. Table 5.1 lists the physical constants and the parameters obtained through direct measurement. The parameters that remain to be determined include the Young's modulus Y, compensation coefficients C_1 to C_4, diffusion coefficient d, anion concentration C^-, dielectric constant κ_e, and charge-stress coupling constant α_o, all of which are tuned by curve-fitting the empirical frequency responses of each route using the Matlab function *fminsearch*.

All the identified parameters are listed in Table 5.2. For route 1, the frequency response at the

Table 5.1: Physical constants and directly measured parameters.

F ($\mathrm{C\ mol^{-1}}$)	R ($\mathrm{J\ mol^{-1}K^{-1}}$)	T (K)	L (mm)	r_1 (mm)	r_2 (mm)
96487	8.3143	290	30	1.10	1.38
h ((μm)	r (mm)	R_1 (Ω)	R_2 (Ω)	R_3 (Ω)	R_4 (Ω)
140	1.24	5.0	3.4	6.1	4.8

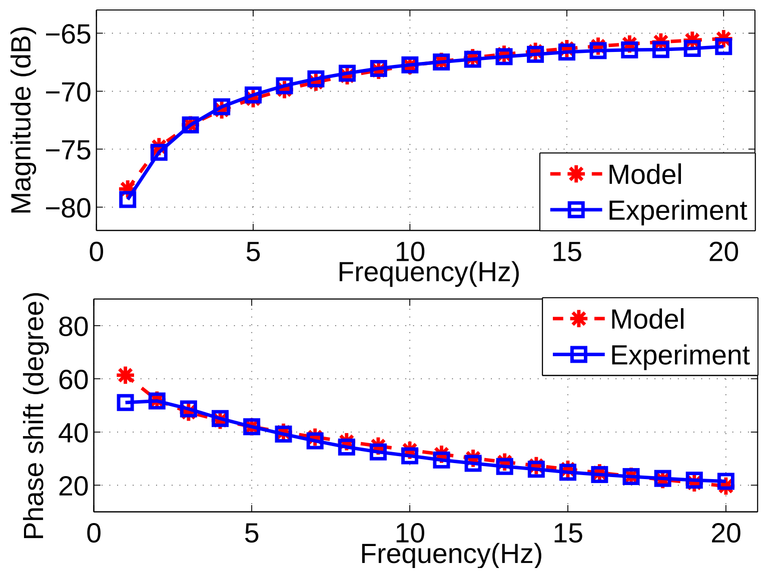

Figure 5.26: Identification of some model parameters via curve-fitting for route 3 at 180° of stimulus orientation. (input: tip excitation; output: IPMC sensing current).

orientation of 0° (or $\gamma = 180°$) was used to identify its parameters, since at this orientation route 1 has largest sensing output. Similarly, the frequency responses at 90°, 180° and 270° were used for route 2, 3 and 4, respectively. Note that the Young's modulus Y, compensation coefficients C_1 to C_4, and charge-stress coupling constant α_o contribute the same scaling effect to the sensing model; see (5.40). Therefore, they cannot be identified separately and thus are treated as a whole in this work. Fig. 5.26 shows the result of curve-fitting for route 3, where the model predictions fit the experimental data well over the considered frequency range for both the magnitude and phase responses.

Table 5.2: Identified parameters by curve-fitting.

C_1Y/α_o (Pa C J^{-1})	C_2Y/α_o (Pa C J^{-1})	C_3Y/α_o (Pa C J^{-1})	C_4Y/α_o (Pa C J^{-1})
1.30×10^5	2.05×10^5	2.41×10^5	2.39×10^5
d ($\mathrm{m}^2\ \mathrm{s}^{-1}$)	C^- (mol m^{-3})	κ_e (F m^{-1})	
3.308×10^{-12}	1086	3.1×10^{-3}	

2)Model Validation: With the identified parameters, we first validate the proposed model in terms of the frequency responses. Fig. 5.27 shows the model prediction and the experimental data at the orientation of 45° for route 3. Note that the data at 45° were not used for parameter identification of route 3. As we can see in the figure, overall the model predictions have good agreement with the experimental data for both the magnitude and phase responses over the full frequency range, providing support for the physical nature of the proposed model. Fig. 5.28 shows the model-predicted and measured magnitudes of the frequency response at 15 Hz for route 3 at varying orientations. Again, one can see that good agreement is achieved, indicating the feasibility of the proposed modeling approach on omnidirectional sensing.

5.2.4 Stimulus Reconstruction

5.2.4.1 Inversion Algorithm

One novel feature of the proposed tubular IPMC sensor is its omnidirectional sensing capability, which can be potentially used for 2D flow and displacement sensing. In such applications, one need to infer the two-dimensional mechanical stimulus given the sensing outputs of the IPMC sensor. In particular, it is of interest to reconstruct the original tip excitation signal $u(t)$ and the orientation angle γ based on the four routes of sensing outputs $i_1(t)$ to $i_4(t)$. Generally, for a single-input-

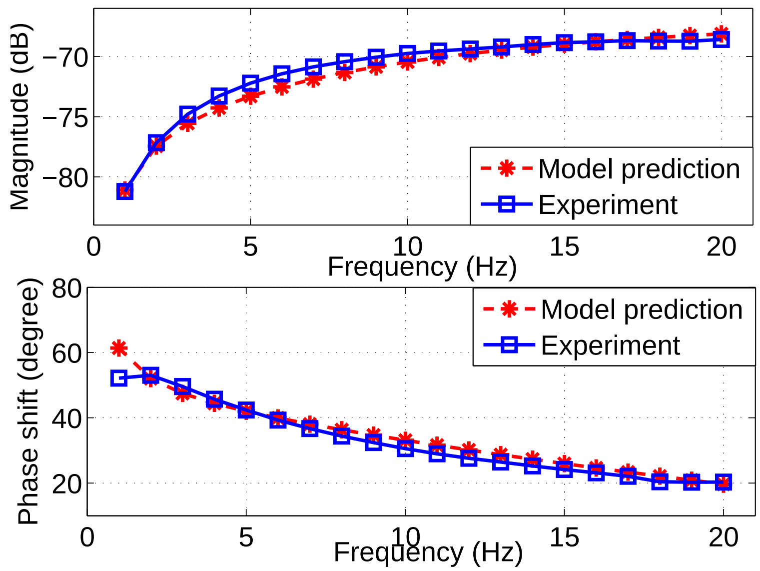

Figure 5.27: Comparison of the measured frequency responses with model predictions for route 3 at 45° of orientation. (input: tip excitation; output: IPMC sensing current).

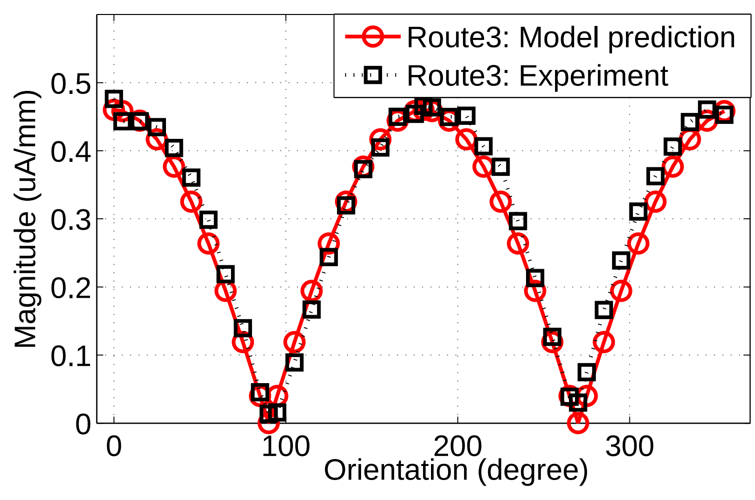

Figure 5.28: Comparison of the measured frequency responses at 15 Hz with model predictions for route 3 at varying orientations. (input: tip excitation; output: IPMC sensing current).

single-output (SISO) system, the reconstruction can be conducted by inverting the forward sensing model

$$u(s) = H_{inv}(s)i(s),$$

where $H_{inv}(s)$ denotes the inverse dynamics

$$H_{inv}(s) = \frac{1}{\hat{H}(s)}.$$

However, the tubular IPMC sensor has multiple inputs and outputs. As discussed in Section 5.2.3, we find that routes 1 and 3 only respond to the $x-$ component u_x of the stimulus $u(t)$, and routes 2 and 4 only respond to the $y-$ component u_y of $u(t)$. Therefore, we can reconstruct u_x and u_y separately. In the following, we will illustrate how to use route 1 to reconstruct u_x. The inverse dynamics for route 1 is

$$\begin{aligned} H_{inv1}(s) &= \frac{u_x(s)}{i_1(s)} = \cos\gamma \frac{1}{\hat{H}_1(s)} \\ &= \frac{\alpha_o L}{6\sqrt{2d}C_1 Y rhs} \frac{q_4 s^4 + q_3 s^3 + q_2 s^2 + q_1 s + q_0}{p_3 s^3 + p_2 s^2 + p_1 s + p_0}. \end{aligned} \tag{5.41}$$

The identified model for (5.40) has no zeros on the right half plane, so the inverse model (5.41) can be directly implemented except for the integrator (pole at the origin). In implementation, we approximate the pole with a pole at $-\varepsilon > 0$. In particular, ε is chosen to be -0.1. This is reasonable since $s + 0.1 \approx s$ within the considered frequency range 1–20 Hz. We note that in the event that $\hat{H}_1$ has zeros on the right half plane, stable but non-causal inversion algorithms can be used [63, 78].

Similarly, the above algorithm is applied to the other routes. Since both routes 1 and 3 can be used to reconstruct u_x, we take the average of the reconstructed values from the two routes as the final prediction for u_x. An analogous approach is taken to reconstruct u_y based on the outputs from routes 2 and 4.

5.2.5 Experimental Results

Fig. 5.29 (a) and (b) show the experimental setup for the reconstruction of mechanical stimulus. A 3D-printed square target is amounted at the tip of the tubular IPMC sensor, so that the tip displacements in the x- and $y-$directions can be easily captured by two laser displacement sensors (OADM 20I6441/S14F; Baumer Electric). The laser target is hollow inside, so its gravity effect is minimized. In the experiments, we manually perturb the tip of the tubular IPMC within the $x-y$ plane along arbitrary directions. The signals from two laser sensors are collected as the true excitation inputs u_x and u_y, while the signals from the four routes of the tubular IPMC sensor are used to reconstruct u_x and u_y. Fig. 5.30 and Fig. 5.31 show the reconstructed tip excitation signals along x-axis and y-axis, respectively, with comparison with the direct measurements. It can be seen that there is a reasonable agreement between the reconstructed and measured deflections for each direction, both in magnitude and in phase. The observed discrepancies can potentially be attributed to several factors, including unmodeled high-frequency dynamics excited by the irregular manual perturbation, and the impact of ambient temperature and humidity conditions, which could be mitigated by exploring several approaches in relevant literature [40, 63, 80].

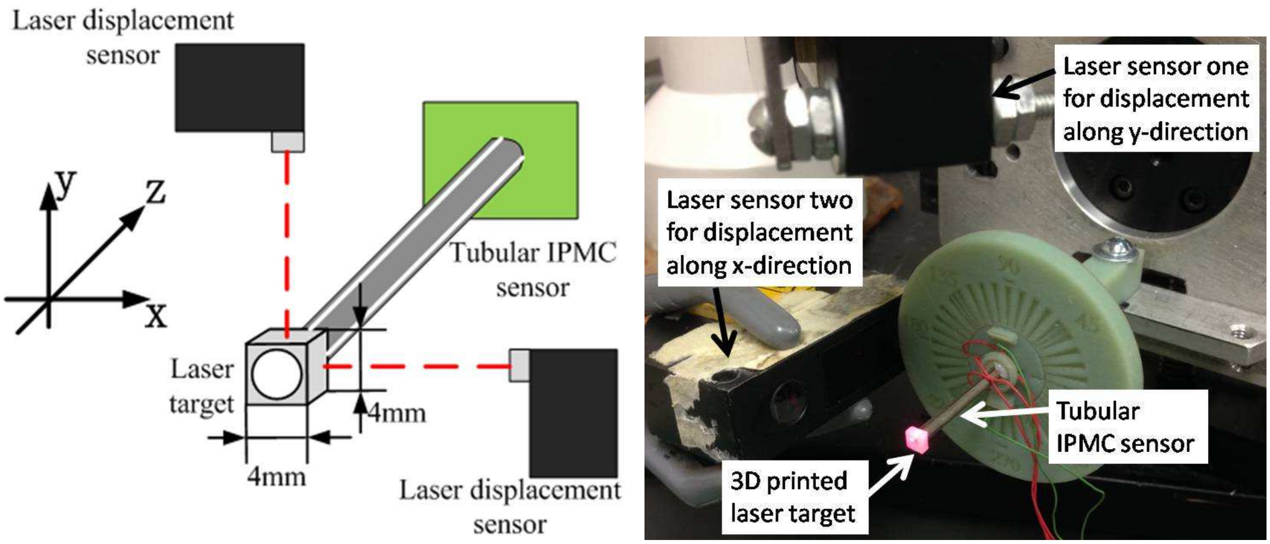

(a) (b)

Figure 5.29: Experimental setup from stimulus reconstruction: (a) Schematic; (b) actual.

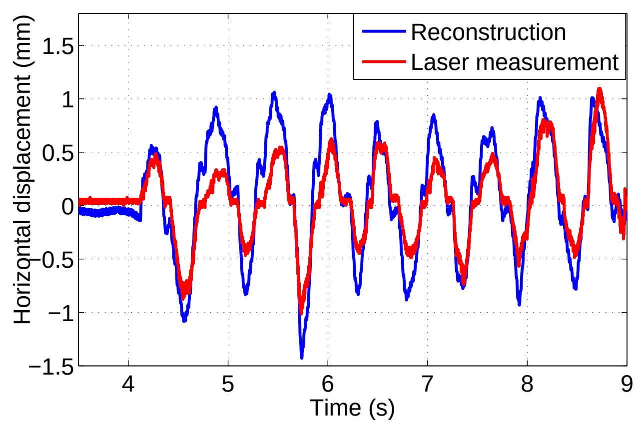

Figure 5.30: Comparison of the horizontal displacement (x-axis) between the reconstruction and the direct measurement.

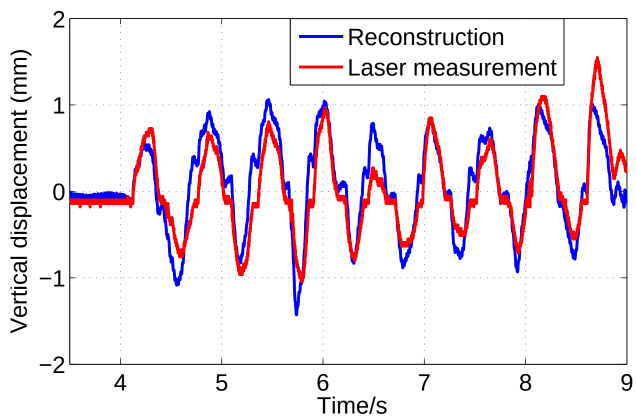

Figure 5.31: Comparison of the vertical displacement (y-axis) between the reconstruction and the direct measurement.

Chapter 6

Micro-fabrication of artificial lateral system based on IPMC

A novel microfabrication approach is proposed in this chapter to design flow sensors in micro array based on IPMC cilia, which is inspired by the lateral line system. Traditional IPMC fabrication is introduced and provides basis for the proposed recipe. Challenges are reviewed on the aspects of Nafion molding and selective formation of electrodes, followed by the detailed fabrication recipe that is explored to address mentioned challenges. The micro-fabrication process is further refined by the double-subtraction approach, and the first prototype is presented with testing results.

6.1 Traditional Approach of IPMC Fabrication

The traditional approach to IPMC fabrication has been well studied many years ago. Although new fabrication methods keep emerging [75,81–84], the traditional way is still the most commonly used and gives the best actuation and sensing properties. Our work in this study is also based on the idea of traditional IPMC fabrication, thus it is necessary to first introduce it. The traditional approach to IPMC fabrication is made up with three major steps. The first step is the surface roughening of Nafion membrane. Typically, a perfluorinated ion exchange membrane known as Nafion purchased from DuPont Company is roughened by sandblasting or plasma etching. This step greatly affects the properties of formed electrodes, but could be ignored if IPMC only need to be functional. Then the membrane is submerged in the platinum complex solution ($[Pt(NH_3)_4]Cl_2$ *or* $[Pt(NH_3)_6]Cl_4$) to impregnate platinum ion into Nafion membrane by ion-exchange process. Once there are enough platinum ions inside Nafion membrane, the last step of reduction is conducted. The platinum ions are reduced to atoms by specific reducing agent, like aqueous solution of sodium borohydride (5 wt% $NaBH_4$ aq), forming the platinum surface electrodes from the inside. If necessary, another ion-exchange process could be done to get the desired cation inside the IPMC (e.g., Li^+). There is also another similar approach to IPMC fabrication based on gold electrodes [84], which has the same steps but uses gold complex solution rather than platinum in the second step of ion-exchange.

This impregnation-reduction ion-exchange process introduced above is fundamentally different from metal deposition by physical vapor deposition (PVD) technology or by electroplating, which are typical for metal deposition in Micro-electromechanical Systems (MEMS) fabrication. For PVD and electroplating, the metal is only deposited on the surface of sample; yet in the impregnation-reduction ion-exchange process, the noble metal is deposited from the inside, forming the electrodes both underneath the surface and above the surface. Electrodes formed in such a way are critical for active sensitivity of IPMC, which is the reason why PVD is not chosen to form the electrodes in our recipe.

6.2 Proposed Fabrication Recipe

The proposed fabrication recipe in this study is to miniaturize the traditional approach to IPMC fabrication, get the IPMC into a standing structure and integrate an array of IPMC cilia to form an artificial lateral line system. Fig. 6.1(a) shows a prototype of artificial lateral line system based on IPMC which is developed by Abdulsdda and Tan [33]. Note that the IPMC flow sensors in this prototype are in macro scale and developed manually. Our goal is to miniaturize this prototype

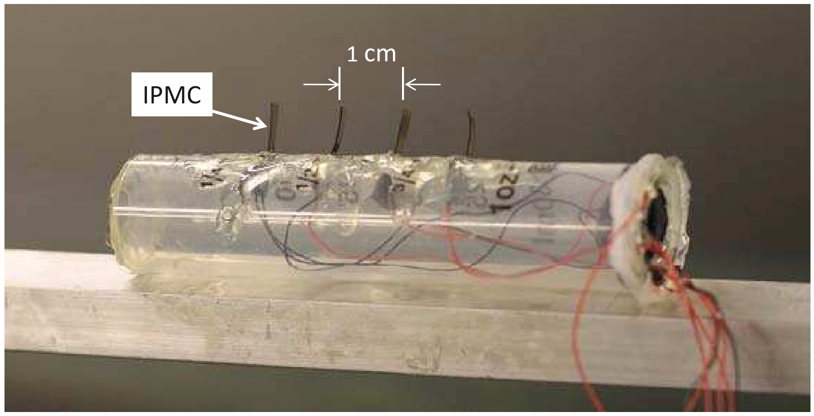

(a)

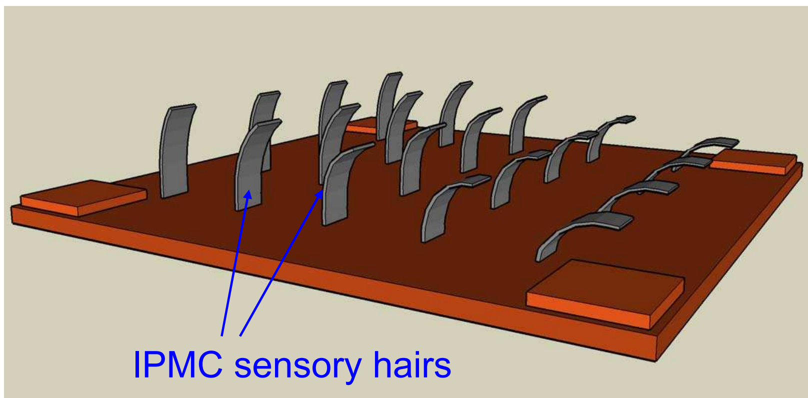

(b)

Figure 6.1: (a) Prototype of IPMC-based artificial lateral line system developed by Abdulsdda and Tan ; (b) Envision of proposed lateral line flow sensor based on IPMC.

and make it more comparable to a biological lateral line system and more compact as a micro flow sensor, as shown in Fig. 6.1(b). As we can see in the figure, to realize an artificial lateral line flow sensor, three-dimensional IPMC hairs need to be fabricated, sticking out of a substrate to effectively interact with flows, and thus the traditional planar MEMS process is too complicated and thus inapplicable.

The outline of proposed recipe for fabricating IPMC-based flow sensor is shown in Fig. 6.2, where side view is displayed on the left and top view on the right. It starts with creating a hole in the silicon wafer so that IPMC sensory hairs can be planted in the substrate. It is followed by constructing a mold on the substrate to hold Nafion solution and form the shape of sensor structure.

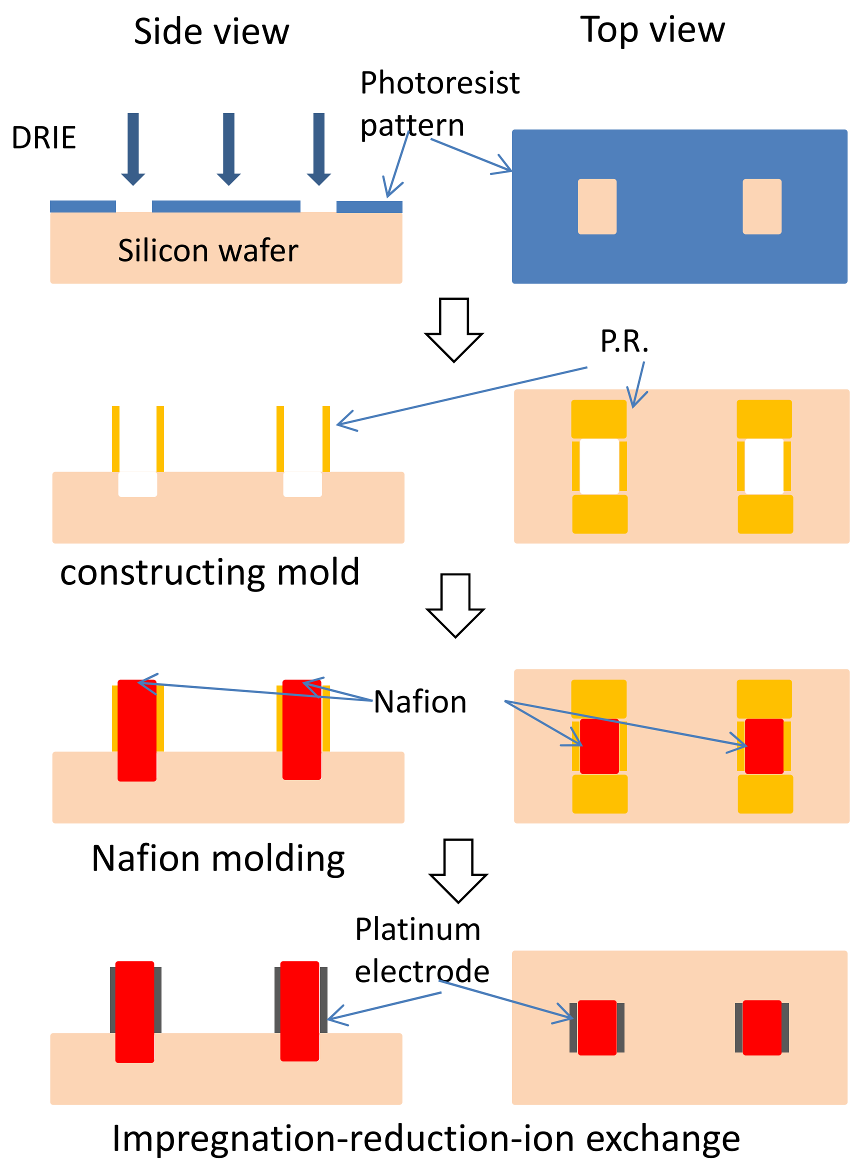

Figure 6.2: Outline of the proposed fabrication recipe.

Recall that IPMC is typically made up with Nafion membrane and can hardly be machined directly in a micro scale, which is the reason why Nafion solution is adopted to create the 3D structure with desired dimensions. Since Nafion solution is used to form the structure, thus a mold is needed to provide the room for solidifying the solution. For the next step, Nafion solution will be injected into these molds and solidified by evaporating the solvent. At last, based on the traditional approach of IPMC fabrication, electrodes are formed on target profiles of the vertical Nafion structure.

6.3 Molding of 3D Nafion Structure

The first critical challenge in the proposed recipe is the molding of 3D Nafion structure. Suppose that a mold has already been created on the substrate, it is difficult to get the Nafion solution into this micro-scale mold. This presents a key difference from other Nafion-cast fabrication process, in which Nafion solution is used to cast into some large container with large planar area layer by layer. It is obvious that Nafion solution cannot be cast into micro-scale mold created in our approach. Micro-injection with a micro-injector might be a choice, but based on the experimental results, it is difficult to find the appropriate micro-injector and the injection stage. Secondly, the solution volume would shrink dramatically during the process of solidification, which requires that the solution injection should be provided continuously, otherwise the structure will not be formed with designed dimensions or uniform. Another problem is that the solidified Nafion structure has severe cracking problem and poor mechanical and electrical properties, as reported in [75, 81].

We propose to use SU-8 to construct the high-aspect-ratio mold, and refine the Nafion solution to solve the cracking problem by exchanging solvent. Then we suspend the whole wafer up-side-down above a hotplate and inject the Nafion solution from back side of the substrate through the etched-through holes. Once the Nafion structure is formed, SU-8 mold is removed. The details are discussed as follows.

SU-8 is a kind of negative photoresist which is typically used to fabricate high-aspect-ratio structures. Here we adopt SU-8 2150, the type with capability of creating thickest structure, to construct the mold for Nafion solution. Before the SU-8 patterning, the wafer is etched through by Deep Reactive-Ion Etching(DRIE). Another silicon wafer is bonded as substrate with the etched-through wafer to prevent liquid SU-8 from flowing out through the holes during the SU-8 pre-baking process. Then SU-8 2150 is patterned on this double wafers structure, so that the SU-8 mold is right encircling the holes. Remove the substrate wafer once SU-8 patterning is finished. The process steps and experiment results are shown in Fig. 6.3.

Before molding the 3D structure, Nafion solution need to be refined in order to avoid crack problem and get the best mechanical and electrical properties of the solidified Nafion. The Nafion solution originally purchased from company contains water and propanol as solvent (e.g., Nafion dispersion of D2021 Alcohol based 1100 EW at 20% weight from Ion Power, Inc, contains 34% weight of water and 44% weight of 1-propanol), which should be replaced by other organic solvent like Dimethylformamide (DMF), otherwise the solidified Nafion would have severe crack problem and very poor mechanical and electrical properties, as reported in [75, 81].

Then the liquid Nafion solution is transformed into solid structure within the SU-8 mold by proposed back injection approach, as indicated in Fig. 6.4(a). A hotplate is used to heat up the solution from the bottom and evaporate the DMF solvent gently. The sample is suspended up-side-down above the hotplate within a proper distance. Refined Nafion solution is cast on the back of silicon wafer, continuously providing the solution into SU-8 mold. The capillary effect has been taken advantage of to prevent the liquid solution from dropping down from the holes. This approach makes sure that solidified Nafion structure is uniform and without contraction problem. The whole setup is indicated in Fig. 6.4(a) and some fabrication result for solidified Nafion 3D

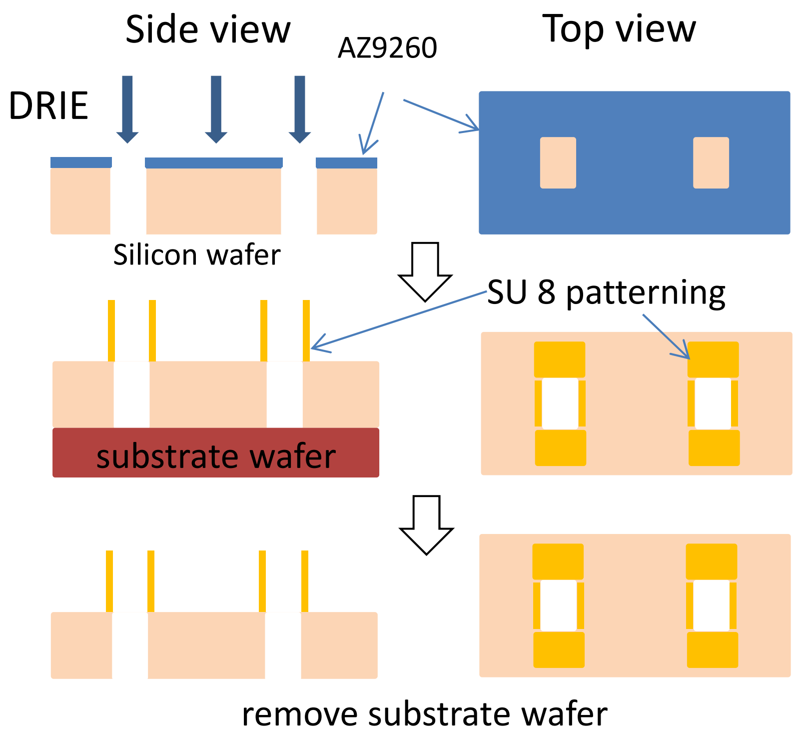

(a)

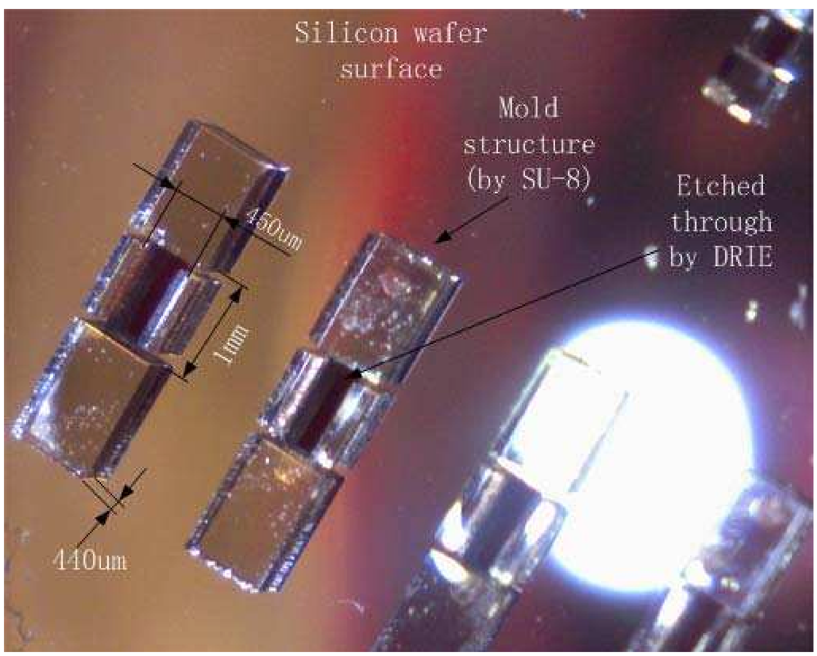

(b)

Figure 6.3: (a) Schematic process of SU-8 patterning ; (b) Experiment result of SU-8 patterning.

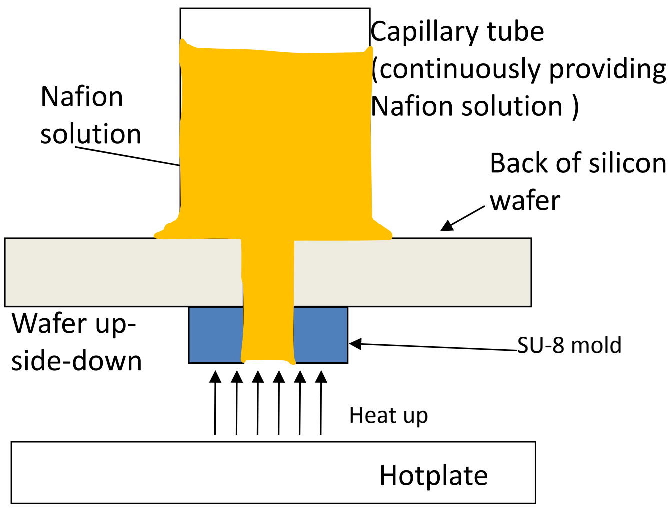

(a)

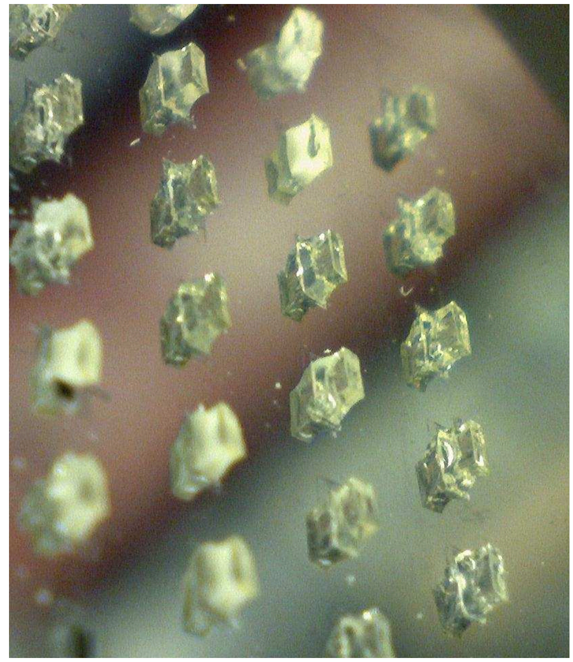

(b)

Figure 6.4: (a) Schematic setup of Nafion molding ; (b) Experiment result of Nafion molding.

structure is displayed in Fig. 6.4(b), where we can see that the proposed approach is feasible and effective to mold Nafion solution. Note that the Nafion structure shown in Fig. 6.4(b) is not quite of a slim and flat beam shape, as drawn in Fig. 6.1(b). It is because this experiment result is only preliminary and for method-proof purpose only. Detailed process will be refined to fabricate more beam-like structure.

6.4 Selective Electrode Formation

Once the Nafion structure is created, the next step is to form the electrodes based on the traditional approach to IPMC fabrication. As we mentioned, there is another challenge of selective electrode formation. Typically, for a big piece of IPMC sample, all its four edges should be cut away before it is used as actuator or sensor, otherwise there will be short-circuit between two electrodes. But for a standing Nafion structure in micro-scale, as shown in Fig. 6.5(a), it is infeasible to cut the

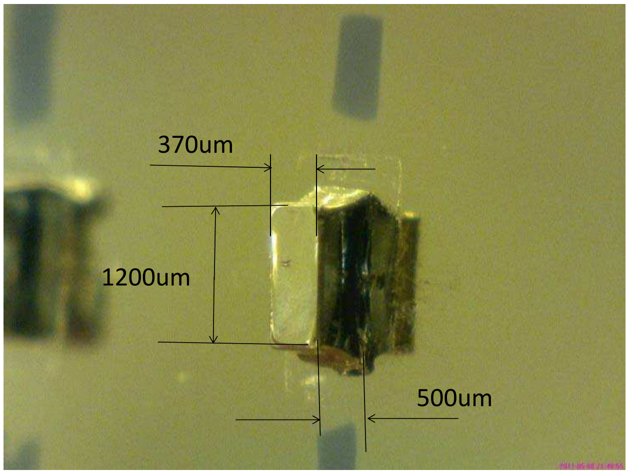

(a)

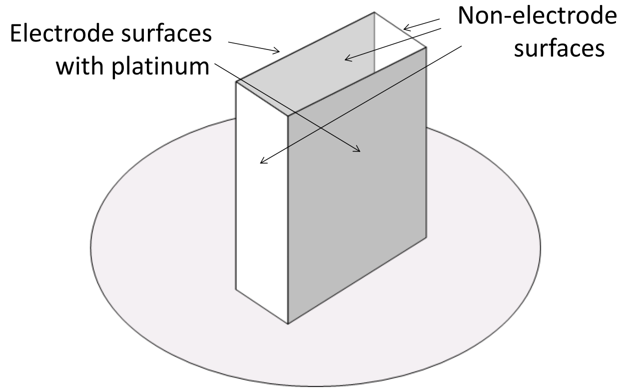

(b)

Figure 6.5: (a) 3D Nafion structure of micro-scale with electrodes formed on all surfaces ; (b) Definition of electrode surfaces and non-electrode surfaces.

edges away by typical methods, like using scissor or blade. A microfabrication approach should be presented to selectively form the electrodes on desired surfaces. Here we define the two electrode surfaces and three non-electrodes surfaces in Fig. 6.5(b).

Intuitively, there would be two ways to achieve the goal of selective electrode formation. One is subtractive approach, which forms the electrodes first on all surfaces and then find some way to remove the metal on the non-electrode surfaces. The other is additive approach, which forms on non-electrode surfaces a protection layer that blocks the electrode formation during the reduction process. These two methods are illustrated in Fig. 6.6 and we have investigated both methods to address the challenge of selective electrode formation.

6.4.1 Additive Electrodes Formation

Typically, platinum is used to form the electrodes for the IPMC fabrication. Since platinum is very difficult to be removed or etched away, only additive approach is considered for platinum-based electrodes. Thus a protection layer of good adhesion with Nafion need to be created on three non-

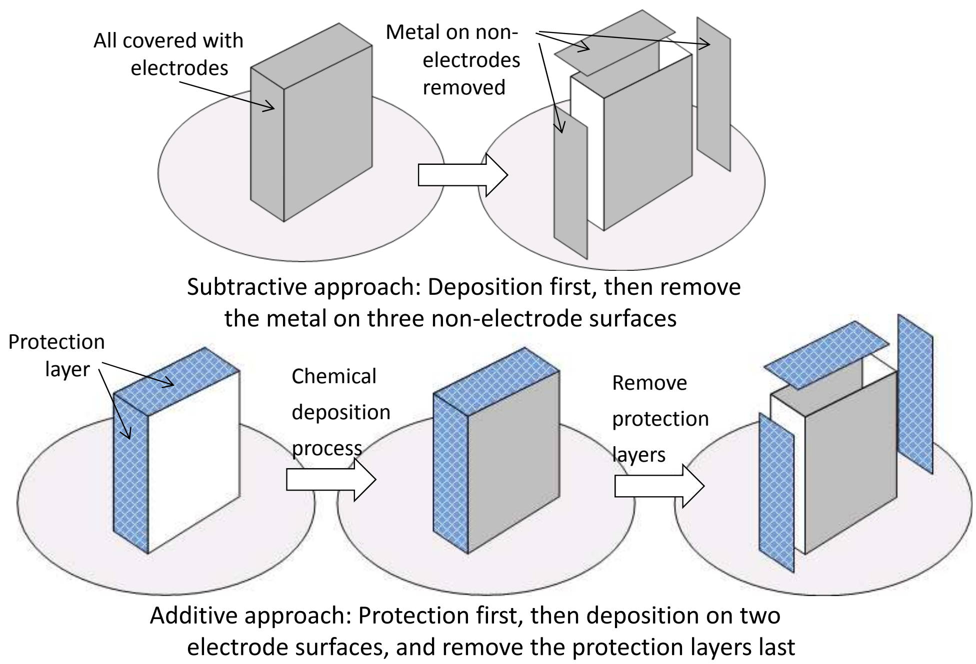

Figure 6.6: Subtractive approach and additive approach.

electrode surfaces of Nafion structure before the reduction process. SU-8 is chosen to form such protection layer due to its good adhesion with surface of solidified Nafion structure, great chemical stability within reducing agent and ease to fabricate. Therefore, there will be two SU-8 patterning processes. The first one is to construct the mold and the second process, as shown in Fig. 6.7(a), is to create protection layer. As we can see in the Fig. 6.7(a), the SU-8 patterning should cover part of the top surface and two edges in order to effectively block electrodes formation. Fig. 6.7(b) shows some experiment result for the second SU-8 patterning.

The experimental results based on this approach are not uniform or consistent, because it is difficult to find the right recipe for the second SU-8 patterning. To effectively protect the surfaces from electrode formation, the adhesion between SU-8 and Nafion surface should be good enough. But if this adhesion is too tight, the SU-8 protection layer cannot be removed later on. There should be some balance about the adhesion and it is very difficult to control this balance.

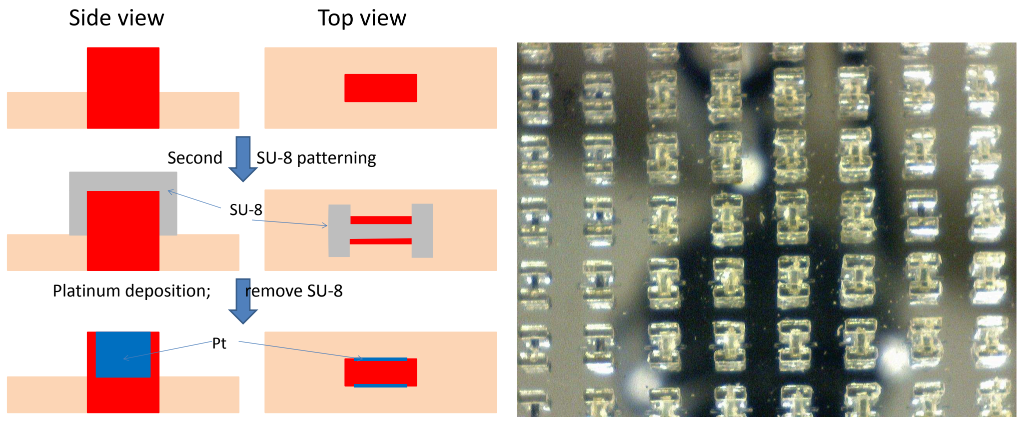

(a) (b)

Figure 6.7: (a) Schematic process of protective SU-8 patterning ; (b) Experiment result of protective SU-8 patterning.

6.4.2 Subtractive Electrodes Formation

Since platinum is difficult to be etched away, gold-based IPMC traditional fabrication is considered in this approach [84], as mentioned in Section 6.1, because of the convenience of removing gold electrodes by wet etching. The detailed recipe is indicated in Fig. 6.8(a). First, the sample with Nafion structures goes through the impregnation-reduction ion-exchange process based on gold complex solution and thus gold electrodes are formed on all the surfaces. It is followed by the parylene deposition (PDS 2035) with $4\mu m$ thickness. Since the parylene deposition is conformal, the whole sample will be covered by it. Selective plasma etching is then conducted to etch away all the parylene except for those on the two electrode surfaces. This is achieved by tilting the sample inside the plasma etching chamber and changing the etching recipe from oxygen plasma etching to pure argon plasma etching (Plasma-therm 790 RIE, Ar 100Sccm, pressure 100mTorr, RF power 150Watts) to get the best selectivity by pure physical etching, as illustrated in Fig. 6.8(b). After that, the whole sample is submerged in gold etchant ($1:4:40\ I_2/KI/H_2O$) for some time, and only the gold electrodes underneath the parylene protection layer will not be etched away. At last, the remaining parylene is removed by oxygen plasma etching. This approach shows great promise for addressing the challenge of selective electrode formation and we have already obtained some preliminary results.

6.5 Double-subtraction Approach

New approach of double-subtraction is found to be promising in modifying this micro-fabrication process, based on some cutting techniques such as pulsed laser cutting, plasma etching, wafer dicing saw, and mill machining. The principal idea is to first cast sufficient Nafion solution into a large mold on a wafer which is etched through by DRIE, and solidify the solution into a Nafion block. A thin layer of SU-8 is casted and cured on top of the Nafion block to prevent any reaction on the top surface of the Nafion structure in the following steps. Certain cutting approach will then be used to cut this Nafion block into thin strips with thickness in a scale of several hundred of micron. Traditional IPMC fabrication method will be applied to deposit platinum electrodes on the two side surfaces of the thin strips. Then the second cutting will be conducted to cut the thin strips into small IPMC cilia. The whole fabrication process and the fabricated prototype are shown in Fig. 6.9, where the CNC milling machine is used as the cutting method. Each IPMC cilia is ”planted” in one etched hole of the wafer, and has the dimension of $3mm$ by $1.5mm$ by $0.5mm$. The sensing response (short-circuit current) of the IPMC cilia under bending in air is shown in Fig. 6.10, which demonstrates good sensitivity and polarity. Note that this double-subtraction approach is still under improvement, e.g., pulsed laser cutting and plasma etching will be tested to reduce the feature size, and appropriate packaging will be designed to encapsulate the whole module and route out the sensing signal of each IPMC cilia.

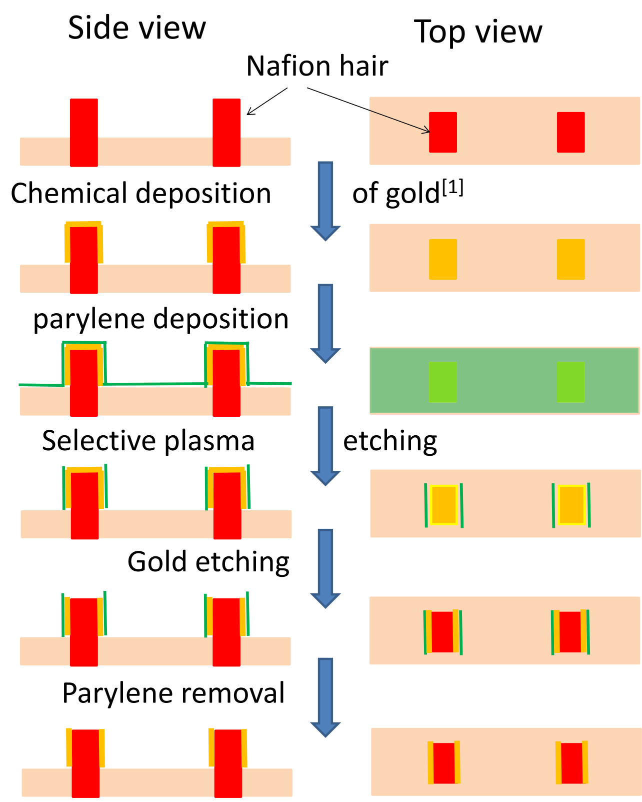

(a)

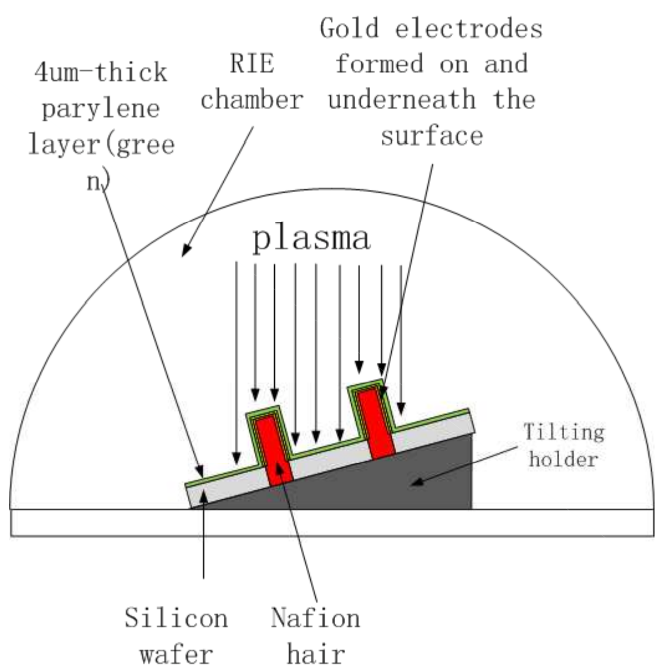

(b)

Figure 6.8: (a) Schematic process of gold-based selective electrode formation ; (b) schematic of selective plasma etching.

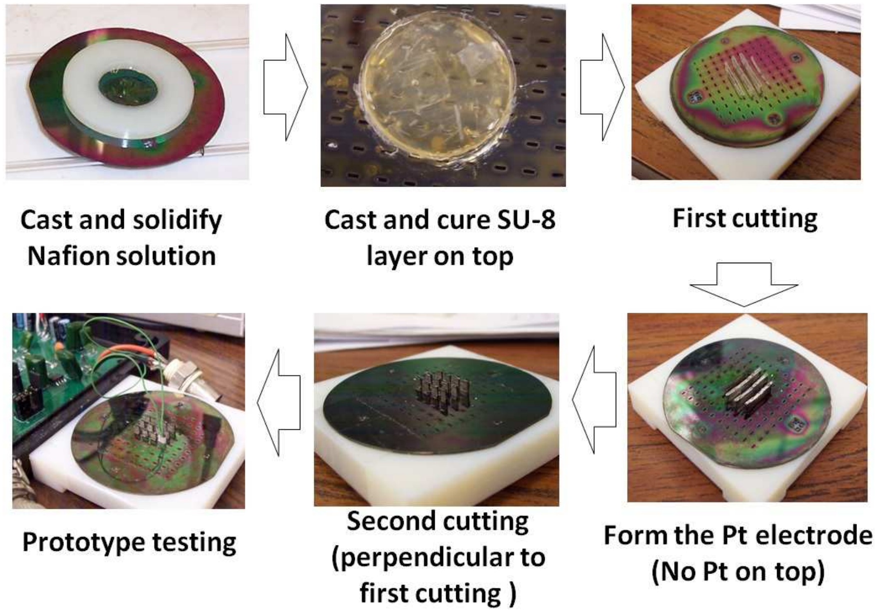

Figure 6.9: Fabrication process of double-subtraction approach.

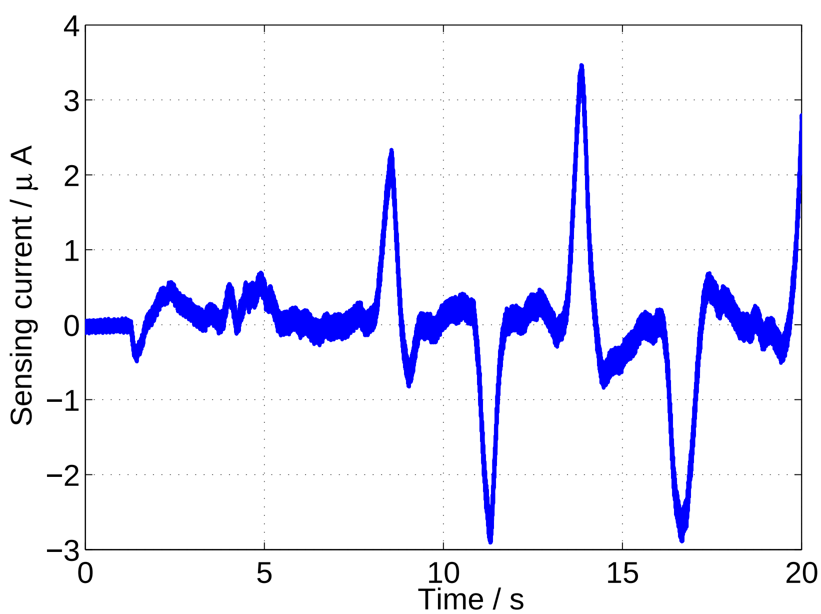

Figure 6.10: Response of the fabricated IPMC cilia under bending in air.

Chapter 7

Conclusions and Future Work

7.1 Conclusions

We derived a dynamic, physics-based model for a base-excited IPMC sensor in air. The model has a closed form and is geometrically scalable. Schemes were proposed to approximate the original infinite-dimensional model with one that is finite-dimensional, to facilitate practical use in sensing and feedback control applications. Experimental results had validated the mechanical vibration model and the overall sensing model. In addition, an inverse compensation scheme was described and illustrated with simulation results and structural monitoring experiments.

We characterized and modeled the humidity influence on IPMC sensors from a physical perspective by identifying the humidity-dependence of the physical parameters in the proposed dynamic model for base-excited IPMC, including the Young's modulus, strain-rate damping coefficient, viscous air damping coefficient, effective dielectric constant, and ionic diffusivity. We further modeled the humidity-dependence of the physical parameters with polynomial functions, which were then plugged into the physics-based model to predict the sensing output under other humidity conditions. Experimental results had validated the humidity-dependent model.

We proposed the fabrication of the encapsulated IPMC sensor based on thick parylene C coating and evaluate their performance. The proposed fabrication process enabled us to control and maintain the hydration level of an encapsulated IPMC sensor to achieve large sensing signal. The water impermeability, mechanical property, corrosion effect and sensing properties of the parylene-encapsulated IPMC sensor were tested by experiments with comparison with naked IPMC sensors.

We developed two novel IPMC sensors capable of two-dimensional sensing to further minimize the structural complexity of the sensor implementation and provide more sensing information. The square column IPMC sensor was fabricated by plating two pairs of electrodes on orthogonal surfaces of a Nafion square column. The sensor was characterized both in air and in water, and an empirical model was further developed for its sensing behavior under water. In order to deal with the coupling issue of the square column IPMC sensor, the tubular thin-wall IPMC sensor was fabricated based on the Nafion tubing. Characterization was conducted on this tubular IPMC under omnidirectional stimulus, and a physical model was developed for its omnidirectional sensing response in air.

A novel micro-fabrication approach was discussed to design flow sensors in micro array based on IPMC cilia, which was inspired by the lateral line system. Challenges in the fabrication process were reviewed on the aspects of Nafion molding and selective formation of electrodes, followed by the detailed fabrication recipe that was explored to address mentioned challenges. A prototype based on the double-subtraction approach was presented with testing results.

7.2 Future Work

First, in the study of tubular IPMC sensors, only the sensor modeling in air was given. It is of great interest to investigate the sensor capability of flow sensing in water. New experiments will be designed to characterize the sensing response of the tubular IPMC sensor under water, and new model needs to be developed to incorporate the interaction between the flow and the tubular sensor.

Second, the proposed micro-fabrication recipe for the IPMC-based artificial lateral line flow sensor needs to be refined based on the double-subtraction approach. Pulsed laser cutting and plasma etching will be tested to reduce the feature size and improve the resolution.

APPENDICES

Appendix A

Derivation of equation (2.41)

Based on the algorithm of the Padé approximation [66], for $f(s) = \sqrt{s+K}$ expanded around $s = s_0$, one gets (2.40) as

$$f(s) = \sqrt{s+K} \approx \frac{\sum_{l=0}^{m} q_l (s-s_0)^l}{1+\sum_{k=1}^{n} d_k (s-s_0)^k}. \tag{A.1}$$

For $m = 3$, $n = 2$,

$$
\begin{aligned}
d_1 &= \frac{a_2 a_5 - a_3 a_4}{a_3^2 - a_2 a_4}, \\
d_2 &= \frac{a_4^2 - a_3 a_5}{a_3^2 - a_2 a_4}, \\
q_0 &= a_0, \\
q_1 &= a_1 + a_0 d_1, \\
q_2 &= a_2 + a_1 d_1 + a_0 d_2, \\
q_3 &= a_3 + a_2 d_1 + a_1 d_2,
\end{aligned}
$$

where $a_0, \cdots, a_5$ are calculated as

$$
\begin{aligned}
a_0 &= f(s_0) = \sqrt{s_0+K}, \\
a_1 &= f^{(1)}(s_0) = \frac{1}{2\sqrt{s_0+K}}, \\
a_2 &= f^{(2)}(s_0) = \frac{-1}{8\sqrt{(s_0+K)^3}}, \\
a_3 &= f^{(3)}(s_0) = \frac{3}{48\sqrt{(s_0+K)^5}}, \\
a_4 &= f^{(4)}(s_0) = \frac{-15}{384\sqrt{(s_0+K)^7}}, \\
a_5 &= f^{(5)}(s_0) = \frac{105}{3840\sqrt{(s_0+K)^9}},
\end{aligned}
$$

and $f^{(k)}$ denotes the kth derivative of f. Substituting (A.1) into (2.39), we have

$$
\begin{aligned}
\hat{H}^E(s) &= \frac{sbY\sqrt{d}}{\alpha_o} \frac{\frac{\Sigma_{l=0}^{3} q_l (s-s_0)^l}{1+\Sigma_{k=1}^{2} d_k (s-s_0)^k} h - \sqrt{d}}{s+K} \\
&= \frac{sbY\sqrt{d}}{\alpha_o} \frac{u_3 s^3 + u_2 s^2 + u_1 s + u_0}{r_3 s^3 + r_2 s^2 + r_1 s + r_0},
\end{aligned}
$$

which is (2.41) with

$$
\begin{aligned}
u_3 &= hq_3, \\
u_2 &= hq_2 - 3hq_3s_0 - \sqrt{d}d_2, \\
u_1 &= 3hq_3s_0^2 - 2hq_2s_0 + 2\sqrt{d}d_2s_0 - \sqrt{d}d_1, \\
u_0 &= -hq_3s_0^3 + (hq_2 - \sqrt{d}d_2)s_0^2 + (\sqrt{d}d_1s_0 - hq_1)s_0 + hq_0 - \sqrt{d}, \\
r_3 &= d_2, \\
r_2 &= d_1 - 2d_2s_0 + Kd_2, \\
r_1 &= d_2s_0^2 - (d_1 + 2Kd_2)s_0 + 1 + Kd_1, \\
r_0 &= Kd_2s_0^2 - Kd_1s_0 + K.
\end{aligned}
$$

Appendix B

Derivation of equation (2.47)

From (2.42), one can perform Taylor expansion about $r_s = r_0$ to approximate $N_3'(s)$, considering up to the second-order terms:

$$\begin{aligned} N_3'(s) &\approx N_3'(r_s = r_0) + \frac{dN_3'(s)}{dr_s}\Big|_{r_s=r_0} (r_s - r_0) + \frac{d^2N_3'(s)}{dr_s^2}\Big|_{r_s=r_0} \frac{(r_s - r_0)^2}{2!} \\ &= b_0 + b_1(r_s - r_0) + b_2(r_s - r_0)^2, \end{aligned} \tag{B.1}$$

where

$$\begin{aligned} R_0 &= \sqrt[4]{r_0}L, \\ b_0 &= N_3'(r_s = r_0) = 2\sqrt[4]{r_0}[\cos(R_0)\sinh(R_0) - \cosh(R_0)\sin(R_0)], \\ b_1 &= \frac{dN_3'(s)}{dr_s}\Big|_{r_s=r_0} = \frac{\cos(R_0)\sinh(R_0) - \cosh(R_0)\sin(R_0)}{2\sqrt[4]{r_0^3}} - \frac{L\sin(R_0)\sinh(R_0)}{\sqrt{r_0}}, \\ b_2 &= \frac{1}{2!}\frac{d^2N_3'(s)}{dr_s^2}\Big|_{r_s=r_0} = \frac{L\sin(R_0)\sinh(R_0)}{8\sqrt{r_0^3}} - \frac{3[\cos(R_0)\sinh(R_0) - \cosh(R_0)\sin(R_0)]}{16\sqrt[4]{r_0^7}} \\ &\quad - \frac{L^2[\cos(R_0)\sinh(R_0) + \cosh(R_0)\sin(R_0)]}{8\sqrt[4]{r_0^5}}. \end{aligned}$$

Similarly, from (2.44), one can approximate $D_1'(s)$ by using the Taylor series expansion:

$$D_1'(s) \approx d_0 + d_1(r_s - r_0) + d_2(r_s - r_0)^2,$$

where

$$d_0 = D_1'(r_s = r_0) = \cosh^2(R_0) + \cos^2(R_0)$$
$$d_1 = \frac{dD_1'(s)}{dr_s} \mid_{r_s=r_0} = \frac{-L[\sin(2R_0) - \sinh(2R_0)]}{4\sqrt[4]{r_0^3}}$$
$$d_2 = \frac{1}{2!}\frac{d^2D_1'(s)}{dr_s^2} \mid_{r_s=r_0} = \frac{L[3\sin(2R_0) - 3\sinh(2R_0) - 2R_0\cos(2R_0) + 2R_0\cos(2R_0)]}{32\sqrt[4]{r_0^7}}.$$

Substituting (2.46) into (2.45), we have (2.47) as

$$\hat{H}^M(s) = \frac{b_2(\frac{ms^2}{4I(Y+C_S s)} - r_0)^2 + b_1(\frac{ms^2}{4I(Y+C_S s)} - r_0) + b_0}{d_2(\frac{ms^2}{4I(Y+C_S s)} - r_0)^2 + d_1(\frac{ms^2}{4I(Y+C_S s)} - r_0) + d_0} = \frac{b_4' s^4 + b_3' s^3 + b_2' s^2 + b_1' s + b_0'}{d_4' s^4 + d_3' s^3 + d_2' s^2 + d_1' s + d_0'},$$

where

$$b_4' = b_2 m^2,$$

$$b_3' = 4b_1 mIC_s - 8b_2 mr_0 IC_s,$$

$$b_2' = 4b_1 mIY - 8b_2 mr_0 IY + 16I^2 C_s^2 (b_2 r_0^2 + b_0 - b_1 r_0),$$

$$b_1' = 32I^2 YC_s (b_2 r_0^2 + b_0 - b_1 r_0),$$

$$b_0' = 16I^2 Y^2 (b_2 r_0^2 + b_0 - b_1 r_0),$$

$$d_4' = d_2 m^2,$$

$$d_3' = 4d_1 mIC_s - 8d_2 mr_0 IC_s,$$

$$d_2' = 4d_1 mIY - 8d_2 mr_0 IY + 16I^2 C_s^2 (d_2 r_0^2 + d_0 - d_1 r_0),$$

$$d_1' = 32I^2 YC_s (d_2 r_0^2 + d_0 - d_1 r_0),$$

$$d_0' = 16I^2 Y^2 (d_2 r_0^2 + d_0 - d_1 r_0).$$

Appendix C

Derivation of the charge density ρ

Performing a Laplace transform for the time variable of $\rho(x',z,t)$, we can convert (5.13) into the Laplace domain:

$$\frac{\partial^2\rho(x',z,s)}{\partial(x')^2} - \beta(s)^2\rho(x',z,s) = 0, \tag{C.1}$$

where $\beta(s) = \sqrt{\frac{s+K}{d}}$ and $K \triangleq \frac{F^2 dC^-}{\kappa_e RT}(1 - C^- \triangle V)$. The general solution of (C.1) takes the form

$$\rho(x',z,s) = a_1(z,s)e^{-\beta(s)x'} + a_2(z,s)e^{\beta(s)x'}, \tag{C.2}$$

where $a_1(z,s)$ and $a_2(z,s)$, some appropriate functions depending on the boundary conditions, are determined based on the assumption that $\rho(x',z,s)$ is proportional to the mechanically induced stress $\sigma(x',z,s)$ at the boundary $x' = \pm h$:

$$\sigma(\pm h,z,s) = \alpha_o\rho(\pm h,z,s), \tag{C.3}$$

where α_o is the charge-stress coupling constant.

The stress σ can be further related to the external stimulus. Consider the stress distribution on $p_{\mathrm{d}\alpha}$ when the tubing is excited by $u_c(t,\alpha)$ at the tip. In the time domain,

$$\sigma(x',z,t) = \frac{M(z,t)(x'+r)}{I} \tag{C.4}$$

where $M(z,t)$ denotes the bending moment at z and I is the moment of inertia of the tubing. $M(z,t)$ can be related to the external force $F(t)$ at the tip by

$$M(z,t) = F(t)(L-z). \tag{C.5}$$

Given the assumption that the tip-excitation is quasi-static within the relatively low frequency range, the out-of-plane deflection $u_c(t,\alpha)$ at the tip can be related to the force $F(t)$ by [85]

$$u_c(t,\alpha) = \frac{L^3 F(t)}{3YI}, \tag{C.6}$$

where Y is the the Young's modulus of the tubing. Combining (C.4) to (C.6) and considering the stress at the boundary, we have

$$\begin{aligned} \sigma(h,z,t) &= \frac{3Yr_1(L-z)u_c(t,\alpha)}{L^3}, \\ \sigma(-h,z,t) &= \frac{3Yr_2(L-z)u_c(t,\alpha)}{L^3}. \end{aligned} \tag{C.7}$$

Now back to Fig. 5.25, by transforming (C.7) into the Laplace domain and combining it with (C.3), we obtain

$$\begin{aligned} \rho(-h,z,s) &= \frac{3Yr_1(L-z)u_c(s,\alpha)}{\alpha_o L^3}, \\ \rho(h,z,s) &= \frac{3Yr_2(L-z)u_c(s,\alpha)}{\alpha_o L^3}, \end{aligned} \tag{C.8}$$

which, together with (C.2), yields

$$a_1(z,s) = \frac{3Y(L-z)u_c(s,\alpha)\beta_1(s)}{\alpha_o L^3}, \tag{C.9}$$

$$a_2(z,s) = \frac{3Y(L-z)u_c(s,\alpha)\beta_2(s)}{\alpha_o L^3}, \tag{C.10}$$

where

$$\beta_1(s) = \frac{r_2 - r_1 e^{2\beta(s)h}}{e^{-\beta(s)h} - e^{3\beta(s)h}}, \tag{C.11}$$

$$\beta_2(s) = \frac{r_1 - r_2 e^{2\beta(s)h}}{e^{-\beta(s)h} - e^{3\beta(s)h}}. \tag{C.12}$$

Appendix D

Derivation of the electrical field E

Using (C.2) and the field equations (5.17) and (5.16), one can derive the expressions for the electrical field E and then for the electrical potential ϕ in the Laplace domain:

$$E(x',z,s) = \frac{a_2(z,s)e^{\beta(s)x'} - a_1(z,s)e^{-\beta(s)x'}}{\kappa_e \beta(s)} + b_1(z,s), \tag{D.1}$$

$$\begin{aligned}\phi(x',z,s) =& \frac{-a_1(z,s)e^{-\beta(s)x'} - a_2(z,s)e^{\beta(s)x'}}{\kappa_e \beta^2(s)} - b_1(z,s)x' \\ &+ b_2(z,s),\end{aligned} \tag{D.2}$$

where $b_1(z,s)$ and $b_2(z,s)$ are appropriate functions to be determined based on the boundary conditions on ϕ. Plugging (D.1) into (5.19) and then combining (5.18) and (5.19) with (D.2), one can solve for $b_1(z,s)$:

$$\begin{aligned}& b_1(z,s) = \\ & \frac{3Yu_c(s,\alpha)(L-z)(e^{-\beta(s)h} - e^{\beta(s)h})(\beta_2(s) - \beta_1(s))}{2\alpha_o h L^3 \kappa_e \beta^2(s)} \\ & + \frac{3sYu_c(s,\alpha)R_c W}{4\alpha_o h L \beta^2(s)(sR_c\kappa_e WL + 2h)}(2h\beta(s)\beta_1(s)e^{-\beta(s)h} \\ & - 2h\beta(s)\beta_2(s)e^{\beta(s)h} + (e^{\beta(s)h} - e^{-\beta(s)h})(\beta_2(s) - \beta_1(s))).\end{aligned} \tag{D.3}$$

Combining (D.3), (D.1) and (5.15), one can obtain the electrical field E and the electrical displacement D.

BIBLIOGRAPHY

BIBLIOGRAPHY

[1] Y. Bar-Cohen, *Electroactive Polymer Actuators as Artificial Muscles: Reality, Potential and Challenges*. Bellingham, WA: SPIE, 2001.

[2] M. Shahinpoor and K. J. Kim, "Ionic polymer-metal composites: I. Fundamentals," *Smart Materials and Structures*, vol. 10, pp. 819–833, 2001.

[3] ——, "Ionic polymer-metal composites: III. Modeling and simulation as biomimetic sensors, actuators, transducers, and artificial muscles," *Smart Materials and Structures*, vol. 13, pp. 1362–1388, 2004.

[4] Z. Chen and X. Tan, "Monolithic fabrication of ionic polymer-metal composite actuators capable of complex deformation," *Sensors and Actuators A: Physical*, vol. 157, no. 2, pp. 246–257, 2010.

[5] H. Lei, W. Li, and X. Tan, "Microfabrication of IPMC cilia for bio-inspired flow sensing," in *Electroactive Polymer Actuators and Devices (EAPAD) XIV*, ser. Proceedings of SPIE, Y. Bar-Cohen, Ed., vol. 8340. Bellingham, WA: SPIE, 2012, p. 83401A.

[6] K. J. Kim and M. Shahinpoor, "Ionic polymer-metal composites: II. manufacturing techniques," *Smart Materials and Structures*, vol. 15, pp. 65–79, 2003.

[7] S. Nemat-Nasser and J. Li, "Electromechanical response of ionic polymer-metal composites," *Journal of Applied Physics*, vol. 87, no. 7, pp. 3321–3331, 2000.

[8] T. Wallmersperger, D. Leo, and C. Kothera, "Transport modeling in ionomeric polymer transducers and its relationship to electromechanical coupling," *Journal of Applied Physics*, vol. 101, no. 2, pp. 4912–4921, 2007.

[9] Z. Chen, Y. Shen, N. Xi, and X. Tan, "Integrated sensing for ionic polymer-metal composite actuators using PVDF thin films," *Smart Materials and Structures*, vol. 16, no. 2, pp. S262–S271, 2007.

[10] S. Tadokoro, S. Yamagami, and M. Ozawa, "Soft micromanipulation device with multiple degrees of freedom consisting of high polymer gel actuators," in *Proceedings of the IEEE International Conference on Micro Electro Mechanical Systems*, 1999, pp. 37–42.

[11] Z. Chen, S. Shatara, and X. Tan, "Modeling of biomimetic robotic fish propelled by an ionic polymer-metal composite caudal fin," *IEEE/ASME Transactions on Mechatronics*, vol. 15, no. 3, pp. 448–459, 2010.

[12] M. Aureli, V. Kopman, and M. Porfiri, "Free-locomotion of underwater vehicles actuated by ionic polymer metal composites," *IEEE/ASME Trans. Mechatronics*, vol. 15, no. 4, pp. 603–614, 2010.

[13] C. Bonomo, L. Fortuna, P. Giannone, S. Graziani, and S. Strazzeri, "A resonant force sensor based on ionic polymer metal composites," *Smart Materials and Structures*, vol. 17, no. 1, p. 015014, 2008.

[14] B. Paola, L. Fortuna, P. Giannone, S. Graziani, and S. Strazzeri, "IPMCs as vibration sensors," in *Proceedings of the IEEE International Instrumentation and Measurement Technology Conference*, 2008, pp. 2065 –2069.

[15] U. Zangrilli and L. M. Weiland, "Prediction of the ionic polymer transducer sensing of shear loading," *Smart Materials and Structures*, vol. 20, no. 9, p. 094013, 2011.

[16] Y. Bahramzadeh and M. Shahinpoor, "Dynamic curvature sensing employing ionic-polymer-metal composite sensors," *Smart Materials and Structures*, vol. 20, p. 094011, 2011.

[17] C. Lim, H. Lei, and X. Tan, "A dynamic, physics-based model for base-excited IPMC sensors," in *Electroactive Polymer Actuators and Devices (EAPAD) XIV*, ser. Proceedings of SPIE, Y. Bar-Cohen, Ed., vol. 8340. Bellingham, WA: SPIE, 2012, p. 83400H.

[18] J. Brufau-Penella, M. Puig-Vidal, P. Giannone, S. Graziani, and S. Strazzeri, "Characterization of the harvesting capabilities of an ionic polymer metal composite device," *Smart Materials and Structures*, vol. 17, no. 1, p. 015009, 2008.

[19] M. Aureli, C. Prince, M. Porfiri, and S. D. Peterson, "Energy harvesting from base excitation of ionic polymer metal composites in fluid environments," *Smart Materials and Structures*, vol. 19, no. 1, p. 015003, 2010.

[20] K. M. Farinholt, N. A. Pedrazas, D. M. Schluneker, D. W. Burt, and C. R. Farrar, "An energy harvesting comparison of piezoelectric and ionically conductive polymers," *Journal of Intelligent Material Systems and Structures*, vol. 20, no. 5, pp. 633–642, 2009.

[21] S. D. Peterson and M. Porfiri, "Energy exchange between a vortex ring and an ionic polymer metal composite," *Applied Physics Letters*, vol. 100, p. 114102, 2012.

[22] K. M. Newbury and D. J. Leo, "Electromechanical modeling and characterization of ionic polymer benders," *Journal of Intelligent Material Systems and Structures*, vol. 13, pp. 51–60, 2002.

[23] K. Newbury, "Characterization, modeling, and control of ionic polymer transducers," Ph.D. dissertation, Virginia Polytechnic Institute and State University, Blacksburg, Virgina, 2002.

[24] C. Bonomo, L. Fortuna, P. Giannone, S. Graziani, and S. Strazzeri, "A model for ionic polymer metal composites as sensors," *Smart Materials and Structures*, vol. 15, pp. 749–758, 2006.

[25] K. Takagi, N. Kamamichi, B. Stoimenov, K. Asaka, T. Mukai, and Z.-W. Luo, "Frequency response characteristics of IPMC sensors with current/voltage measurements," in *Proc. SPIE 6927*, Bellingham,WA, 2008, p. 692724.

[26] M. A. Buechler and D. J. Leo, "Charaterization and variational modeling of ionic polymer transducers," *J. Vib. Acoust*, vol. 129, pp. 113–120, 2007.

[27] P. G. de Gennes, K. Okumura, M. Shahimpoor, and K. Kim, "Mechanoelectric effects in ionic gels," *Europhys. Lett.*, vol. 50, no. 4, pp. 513–518, 2000.

[28] K. Farinholt and D. J. Leo, "Modeling of electromechanical charge sensing in ionic polymer transducers," *Mechanics of Materials*, vol. 36, pp. 421–433, 2004.

[29] Z. Chen, X. Tan, A. Will, and C. Ziel, "A dynamic model for ionic polymer-metal composite sensors," *Smart Materials and Structures*, vol. 16, pp. 1477–1488, 2007.

[30] M. Porfiri, "An electromechanical model for sensing and actuation of ionic polymer metal composites," *Smart Materials and Structures*, vol. 18, no. 1, p. 015016, 2009.

[31] G. D. Bufalo, L. Placidi, and M. Porfiri, "A mixture theory framework for modeling the mechanical actuation of ionic polymer metal composites," *Smart Materials and Structures*, vol. 17, no. 4, p. 045010, 2008.

[32] M. Aureli and M. Porfiri, "Nonlinear sensing of ionic polymer metal composites," *Continuum Mechanics and Thermodynamics*, 2012, in press.

[33] A. T. Abdulsadda and X. Tan, "An artificial lateral line system using IPMC sensor arrays," *International Journal of Smart and Nano Materials*, 2012, to appear.

[34] F. Bauer, S. Denneler, and M. Willert-Porada, "Influence of temperature and humidity on the mechanical properties of nafion 117 polymer electrolyte membrane," *Journal of Polymer Science Part B: Polymer Physics*, vol. 43, no. 7, pp. 786–795, 2005.

[35] E. Shoji and D. Hirayama, "Effects of humidity on the performance of ionic polymer-metal composite actuators: Experimental study of the back-relaxation of actuators," *The Journal of Physical Chemistry B*, vol. 111, no. 41, pp. 11 915–11 920, 2007.

[36] P. Brunetto, L. Fortuna, P. Giannone, S. Graziani, and S. Strazzeri, "Static and dynamic characterization of the temperature and humidity influence on ipmc actuators," *IEEE Transactions on Instrumentation and Measurement*, vol. 59, no. 4, pp. 893–908, 2010.

[37] ——, "Characterization of the temperature and humidity influence on ionic polymer-metal composites as sensors," *IEEE Transactions on Instrumentation and Measurement*, vol. 60, no. 8, pp. 2951–2958, 2011.

[38] K. Park, "Characterization of the solvent evaporation effect on ionic polymer-metal composite sensors," *Journal of the Korean Physical Society*, vol. 59, no. 6, pp. 3401–3409, 2011.

[39] P. Brunetto, L. Fortuna, P. Giannone, S. Graziani, and S. Strazzeri, "Characterization of the temperature and humidity influence on ionic polymer-metal composites as sensors," *IEEE Transactions on Instrumentation and Measurement*, vol. 60, no. 8, pp. 2951–2958, 2011.

[40] C. Lim, H. Lei, and X. Tan, "Characterization and modeling of humidity-dependence of ipmc sensing dynamics," in *Electroactive Polymer Actuators and Devices (EAPAD)*, ser. Proceedings of SPIE, Y. Bar-Cohen, Ed., vol. 8687. San Diego, CA: SPIE, 2013, p. 868720.

[41] M. Shahinpoor and K. Kim, "Effects of counter-ions on the performance of ipmcs," in *Electroactive Polymer Actuators and Devices (EAPAD)*, ser. Proceedings of SPIE, Y. Bar-Cohen, Ed., vol. 3987. Newport Beach, CA: SPIE, 2000, pp. 110–120.

[42] R. Tiwari and K. Kim, "Improved ipmc sensing by use of cation and through induced nano-to-micro scale surface cracks," in *Sensors and Smart Structures Technologies for Civil, Mechanical, and Aerospace Systems*, ser. Proceedings of SPIE, M. Tomizuka, Ed., vol. 6932. San Diego, CA: SPIE, 2008, p. 69323H.

[43] M. Shahinpoor, Y. Bar-Cohen, J. Simpson, and J. Smith, "Ionic polymer-metal composites IPMCs as biomimetic sensors, actuators and artificial muscle–a review," *Smart Materials and Structures*, vol. 7, no. 6, p. R15, 1998.

[44] B. Akle and D. Leo, "Electromechanical transduction in multilayer ionic transducers," *Smart Materials and Structures*, vol. 13, no. 5, p. 1081, 2004.

[45] J. Franklin, "Electromechanical modeling of encapsulated ionic polymer transducers," Master's thesis, Faculty of the Virginia Polytechnic Institute and State University, 2003.

[46] E. Malone and H. Lipson, "Freeform fabrication of electroactive polymer actuators and electromechanical devices," in *Proceedings of the 15th Solid Freeform Fabrication Symposium*, Austin TX, 2004, pp. 697 –708.

[47] J. Barramba, J. Silva, and P. C. Branco, "Evaluation of dielectric gel coating for encapsulation of ionic polymer-metal composite actuators," *Sensors Actuators A*, vol. 140, pp. 232–238, 2007.

[48] S. Kim, I. Lee, H. Lee, and Y. Kim, "Performance improvement of an ionic polymercmetal composite actuator by parylene thin film coating," *Smart Materials and Structures*, vol. 15, no. 6, pp. 1540–1546, 2006.

[49] M. Bennett and D. Leo, "Ionic liquids as stable solvents for ionic polymer transducers," *Sensors Actuators A*, vol. 115, no. 1, pp. 79–90, 2004.

[50] K. Oguro, N. Fujiwara, K. Asaka, K. Onishi, and S. Sewa, "Polymer electrolyte actuator with gold electrodes," in *Electroactive Polymer Actuators and Devices (EAPAD) XIV*, ser. Proceedings of SPIE, Y. Bar-Cohen, Ed., vol. 3669. Bellingham, WA: SPIE, 1999, pp. 3669–39.

[51] S. J. Kim, D. Pugal, J. Wong, K. J. Kim, and W. Yim, "A bio-inspired multi degree of freedom actuator based on a novel cylindrical ionic polymer-metal composite material," *Robotics and Autonomous Systems*, vol. 62, no. 1, pp. 53–60, 2014.

[52] L. Shen, Y. Cha, A. Shams, and M. Porfiri, "Fabrication and buckling analysis of ionic polymer metal composite pipes," *Smart Materials and Structures*, vol. 22, no. 10, p. 105032, 2013.

[53] S. Coombs, "Smart skins: Information processing by lateral line flow sensors," *Autonomous Robots*, vol. 11, pp. 255–261, 2001.

[54] S. Coombs and C. B. Braun, *Information Processing by the Lateral Line System*. New York: Springer-Verlag, 2003.

[55] K. Pohlmann, J. Atema, and T. Breithaupt, "Structural scaling and functional design of the cereal wind-receptor hairs of a cricket," *Journal of Experimental Biology*, vol. 207, pp. 2971–2978, 2004.

[56] J. M. Gardiner and J. Atema, "Sharks need the lateral line to locate odor sources: Rheotaxis and eddy chemotaxis," *Journal of Experimental Biology*, vol. 210, pp. 1925–1934, 2007.

[57] T. Pitcher, B. L. Partridge, and C. S. Wardle, "A blind fish can school," *Science*, vol. 194, pp. 963–965, 1976.

[58] Y. Yang, S. Pandya, D. L. Jones, J. M. Engel, and C. Liu, "Multisensor processing algorithms for underwater dipole localization and tracking using mems artificial lateral-line sensors," *EURASIP Journal on Applied Signal Processing*, vol. 2006, pp. 76 593:1–76 593:8, 2006.

[59] Y. Yang, N. Nguyen, N. Chen, M. Lockwood, C. Tucker, H. Hu, H. Bleckmann, C. Liu, and D. L. Jones, "Artificial lateral line with biomimetic neuromasts to emulate fish sensing," *Bioinspiration and Biomimetics*, vol. 5, pp. 016 001:1–016 001:9, 2010.

[60] A. Dagamseh, T. Lammerink, M. Kolster, C. Bruinink, R. Wiegerink, and G. Krijnen, "Dipole-source localization using biomimetic flow-sensor arrays positioned as lateral-line system," *Sensors and Actuators A*, 2010.

[61] R. W. Clough and J. Penzien, *Dynamics of Structures*. New York: McGraw-Hill, 1975.

[62] A. Erturk and D. J. Inman, *Piezoelectric Energy Harvesting, First Edition*. UK: John Wiley & Sons, Ltd., 2011.

[63] T. Ganley, D. L. S. Hung, G. Zhu, and X. Tan, "Modeling and inverse compensation of temperature-dependent ionic polymer-metal composite sensor dynamics," *IEEE/ASME Transactions on Mechatronics*, vol. 16, no. 1, pp. 80–89, 2011.

[64] H. Lei, W. Li, G. Zhu, and X. Tan, "Evaluation of encapsulated ipmc sensor based on thick parylene coating," ser. Proceedings of ASME 2012 Conference on Smart Materials, Adaptive Structures and Intelligent Systems, Stone Mountain, GA, 2012, p. 7975.

[65] A. K. Ghosh, "Vibration of a cantilever beam on a composite support with base excitation," *Journal of Sound and Vibration*, vol. 105, no. 1, pp. 91–99, 1986.

[66] G. A. Baker and P. Graves-Morris, *Padé Approximants*. New York: Cambridge University Press, 1996.

[67] S. Devasia, D. Chen, and B. Paden, "Nonlinear inversion-based output tracking," *IEEE Trans. Autom. Control*, vol. 41, no. 7, pp. 930–942, 1996.

[68] Z. Chen and X. Tan, “A control-oriented and physics-based model for ionic polymer-metal composite actuators,” *IEEE/ASME Transactions on Mechatronics*, vol. 13, no. 5, pp. 519–529, 2008.

[69] P. Menon, “Rates and activation energy of water vapor permeation through thin film parylene c,” Senior Thesis, California Institute of Technology, 2007.

[70] W. Hubbell, H. Brandt, and Z. Munir, “Transient and steady state water vapor permeation through polymer films,” *Journal of Polymer Science*, vol. 13, pp. 493–507, 1975.

[71] G. Loeb, M. Salcman, and E. Schmidt, “Parylene as a chronically stable,reproducible microelectrode insulator,” *IEEE Transactions on Biomedical Engineering*, vol. BME-24, no. 2, pp. 121–129, 1977.

[72] A. Tanioka, N. Fukushima, K. Hasegawa, K. Miyasaka, and N. Takahashi, “Permeation of gases across the poly(chlorop-xylylene) membrane,” *Journal of Applied Polymer Science*, vol. 54, pp. 219–229, 1994.

[73] P. R. Menon, W. Li, A. Tooker, and Y. Tai, “Characterization of water vapor permeation through thin film parylene c,” in *Proceedings of Transducers*, Denver, CO, 2009, pp. 1892 –1895.

[74] X. Chen, G. Zhu, X. Yang, D. L. Hung, and X. Tan, “Model-based estimation of flow characteristics using an ionic polymer-metal composite beam,” *IEEE/ASME Transactions on Mechatronics*, vol. 18, no. 3, pp. 932–943, 2013.

[75] R. Silva, M. D. Francesco, and A. Pozio, “Solution-cast nafion ionomer membranes: preparation and characterization,” *Electrochimica Acta*, vol. 49, pp. 3211–3219, 2004.

[76] L. A. Zook and J. Leddy, “Density and solubility of nafion: Recast, annealed, and commercial films,” *Analytical Chemistry*, vol. 68, no. 21, pp. 3793–3796, 1996.

[77] H. Lamb, *Hydrodynamics*. Cambridge: Cambridge University Press, 1932.

[78] H. Lei, C. Lim, and X. Tan, “Modeling and inverse compensation of dynamics of base-excited ionic polymercmetal composite sensors,” *Journal of Intelligent Material Systems and Structures*, vol. 24, no. 13, pp. 1557–1571, 2013.

[79] C. R. Calladine, *Theory of Shell Structures*. Cambridge, UK: Cambridge University Press, 1989.

[80] H. Lei, W. Li, and X. Tan, “Encapsulation of ionic polymer-metal composite (ipmc) sensors with thick parylene: Fabrication process and characterization results,” *Sensors & Actuators: A. Physical*, vol. 217, pp. 1–12, 2014.

[81] E. Malone and H. Lipson, “Freeform fabrication of ionomeric polymer-metal composites actuators,” *Rapid Prototyping Journal*, vol. 12, no. 5, pp. 244–253, 2006.

[82] I.-S. Park, R. Tiwari, and K. J. Kim, “Ipmc paints,” in *Proc. of SPIE 6927*, Y. Bar-Cohen, Ed., 2008, p. 69270B.

[83] Q. Chen, K. Xiong, K. Bian, N. Jin, and B. Wang, “Preparation and performance of soft actuator based on ipmc with silver electrodes,” *Front. Mech. Eng. China*, vol. 4, no. 4, pp. 436–440, 2009.

[84] N. Fujiwara, K. Asaka, Y. Nishimura, K. Oguro, and E. Torikai, “Preparation of gold-solid polymer electrolyte composites as electric stimuli-responsive materials,” *Chem. Mater.*, vol. 12, pp. 1750–1754, 2000.

[85] J. M. Gere, *Mechanics of Materials*. Belmont, CA: Thomson Learning, Inc., 2004.